

**Microstructural Effects on Charge Transfer in Small Molecule
Heterojunctions: A Tale of Tails**

by

Rebecca A. Callahan

B.A., Hendrix College, 2009

A thesis submitted to the
Faculty of the Graduate School of the
University of Colorado in partial fulfillment
of the requirements for the degree of
Doctor of Philosophy
Department of Chemistry and Biochemistry

This thesis entitled:

Microstructural Effects on Charge Transfer in Small Molecule Heterojunctions: A Tale of Tails

written by Rebecca A. Callahan

has been approved for the Department of Chemistry and Biochemistry by

David M. Walba

Garry Rumbles

Date: _____

The final copy of this thesis has been examined by the signatories, and we find that both the content and the form meet acceptable presentation standards of scholarly work in the above mentioned discipline.

Callahan, Rebecca A. (Ph.D. Material Chemistry)

Microstructural Effects on Charge Transfer in Small Molecule Heterojunctions: A Tale of Tails

Thesis co-directed by Prof. David M. Walba and Prof. Garry Rumbles

In a simplified picture of an organic photovoltaic active layer the molecular orbital energies are used to predict photo-induced charge transfer between potential electron donors and acceptors, a crucial step in the generation of electrical power from light. Yet often systems that are projected to work by this metric, in fact, do not work; perhaps there is more to it. The work presented in this thesis aims to understand how solid-state microstructure ultimately affects photoinduced charge transfer. Two distinctive small molecule electron donors are presented and are determined to undergo microstructure-modulated charge transfer for different reasons. Time-resolved microwave conductivity is used to detect photogenerated charges and powder x-ray diffraction, transmission electron microscopy, and solid-state spectroscopy are used to elucidate the film microstructure. In the first system presented, a helical nanofilament heterojunction is shown to yield more charge transfer than a lamellar structuring of the same components; a pathway for charge recombination is proposed to compete with charge generation. In the second system, a series of PBTTT-inspired small molecules with varied alkoxy tail lengths demonstrates systematic differences in the solid-state microstructure, photophysics, and charge transfer driving forces and consequently yield. In both cases it is conclusive that solid-state microstructure has considerable effect on the photophysical properties and charge transfer in organic donor-acceptor blends.

This dissertation is dedicated to my late mother, Kathleen Moran, for her strength, vision,
tenacity and beauty.

Acknowledgements

I would first like to acknowledge and wholeheartedly thank my advisors David Walba and Garry Rumbles. Dave, your enthusiasm for science and learning is truly infectious and something that I will carry with me forever. When my mom got sick and I needed to be with her, your understanding and support of my decision was momentous. Garry, you have been such a steady rock for me through research ups and downs. I cannot thank you enough for your belief in me particularly in this last year; I would not have made it through without your assistance and guidance.

I would also like to thank all my present and past labmates in both the Walba and Rumbles groups as well as cohorts in the Liquid Crystal Materials Research Center (LCMRC) and at the National Renewable Energy Lab (NREL) for your knowledge, companionship, and encouragement; in particular, Hilary Marsh, David Coffey, Eva Korblova, Art Klitnick, Obadiah Reid, Nikos Kopidakis, Andrew Ferguson, Mike Springer, Dong Chen, Noel Clark. Also I would like to acknowledge and thank Joey Luther for funding me my final year, and in so reigniting my interest in science again. Thanks to Christine Morrow for including me in many amazing outreach opportunities!

A heartfelt thanks to my dear friend Barbara Hughes for her continued support through the many trials and tribulations of life, to Lizz Griffith and Molly Beernink, I am so proud of you all and there is no way I could have stuck this out without you by my side. To Mallory Bader, you are a beacon in the ocean, often reminding me that I do have a home. To my friends and improv family at the Bovine Metropolis Theatre and Denver improv community in whole you started and have kept me laughing over the past two years, this thesis wouldn't exist without that outlet. To Walter, you have given me so much strength, encouragement, humility, trust and countless good ole fashioned belly laughs, you have a special place in my heart. Especially thanks to Alicia Wheelock, Jared McBain, Rose Schuchat and Steve O'Neill, I am lucky to call you good friends. For the years of companionship filled with tasty dinners, fiercely competitive board games, meandering hikes and loving care and support I want to thank Paul and Pearl Donohoo-Vallett as well as Kathleen and Mark Owkes.

For their love and support, I thank my family. To my sister, Lizz, I am so proud of you and your wonderful family and to my brother, Andrew, you are an amazing person whom I am so honored to know. To my father, grandmother and many aunts and uncles, I love you! To my cat, Milly, and pup, Chiquita, thanks for all the well-timed cuddles and for covering everything I own in your hair.

And to my Momma, I miss you *every* moment and I wish you were here to see me defend - but I will always feel your love and strength.

Table of Contents

Chapter I: Introduction and Motivation	1
1.1 Introductory Remarks	1
1.2 Organic Photovoltaics Active Layers	1
1.3 Organic Liquid Crystals and Crystals	9
1.4 This Work	12
Chapter II: Experimental Methods and Data Analysis	15
2.1 Overview of Experiments and Analysis	15
2.2 Flash-photolysis Time Resolved Microwave Conductivity.....	15
2.2.1 Fundamentals of TRMC	16
2.2.2 TRMC Experimental Setup.....	21
2.2.3 Sample Measurement.....	23
2.2.4 Data Analysis and Experimental Variations	25
2.2.5 Thin-Film Absorption Measurements.....	26
2.3 Photoluminescence	27
2.3.1 Steady-State Solution Photoluminescence.....	27
2.3.2 Relative Quantum Yields.....	28
2.3.3 Solid-State Film Photoluminescence	29
2.3.4 Photoluminescence Quenching.....	29
2.3.5 Time-Correlated Single Photon Counting (TCSPC).....	30
2.3 Powder X-ray Diffraction on Thin Films.....	32
2.3.1 Experimental Parameters	32
2.3.2 Basics of Diffraction	33
2.3.3 Peak Position, Width and Analysis.....	33
2.4 Transmission Electron Microscopy (TEM)	34
2.5 Differential Scanning Calorimetry (DSC)	34
2.6 Thin-film Sample Preparation.....	35
2.7 Summary.....	36
Chapter III: Helical Nanofilament Thin Films.....	37
3.1 Introduction to HNFs	37

3.2 Transmission Electron Microscopy (TEM)	43
3.2.1 TEM of neat P-9-OPIMB films	43
3.2.2 TEM of P-9-OPIMB/PC60BM thin films	45
3.3 XRD of Thin-Film Samples.....	48
3.3.1 XRD of Neat P-9-OPIMB.....	49
3.3.2 XRD of P-9-OPIMB with Fullerene Dopants.....	52
3.4 Differential Scanning Calorimetry.....	54
3.4.1 Mixed P-9-OPIMB/PCBM Differential Scanning Calorimetry	54
3.4.2 Calorimetry of P-9-OPIMB Thin Films.....	57
3.5 Conclusion	59
Chapter IV: Charge Transfer in the Helical Nanofilament System	61
4.1 Introduction to HNFs as a Donor-Acceptor Heterojunction.....	61
4.2 Solid-State Spectroscopy	65
4.2.1 Thin-film Optical Absorption of P-9-OPIMB and Blends	66
4.2.2 P-9-OPIMB Thin-film Photoluminescence	67
4.2.3 PCBM Photoluminescence and Quenching with HNFs	68
4.3 Photoconductivity of P-9-OPIMB in a Bilayer and Heterojunction.....	71
4.3.1 Photoconductivity Studies on P-9-OPIMB-C60 Bilayer	71
4.3.2 P-9-OPIMB Microwave Conductivity Contribution	76
4.3.3 PCBM Photoconductivity at Different Wavelengths.....	79
4.3.4 Photoconductivity Studies on P-9-OPIMB-PC ₆₀ BM Blends.....	79
4.3.5 Heterojunction P-9-OPIMB/PCBM Lifetime	82
4.3.6 Temperature Dependency of P-9-OPIMB/PCBM Blend Photoconductivity	83
4.3.7 Photoconductivity of PC ₇₀ BM/HNF Heterojunctions	85
4.4 Conclusions.....	85
Chapter V: Solution Optical and Electrochemical Characterization of n,2-OBTTT	88
5.1 Introduction to the n,2-OBTTT Series.....	88
5.1.1 Small Molecule Model Compound Studies	89
5.1.2 Previously Reported Model Compound Studies.....	90
5.1.3 Previous work on PBTTT	91
5.1.4 Helical Nanofilament Forming Mesogen Motivation.....	91
5.1.5 Basic Properties of n,2-OBTTT.....	92

5.2 Absorption Characterization of n,2-OBTTT Solutions	93
5.3 Steady-State Photoluminescence of n,2-OBTTT Solutions.....	96
5.3.1 Relative Fluorescence Quantum Yield Determination for n,2-OBTTT	97
5.3.2 Time-Resolved Photoluminescence of n,2-OBTTT	100
5.3.3 Determination of k_r and Oscillator Strength (f_{nm}).....	100
5.4 Electrochemical Determination of Frontier Orbital Energy Levels in n,2-OBTTT	102
5.5 Conclusion	107
Chapter VI: Solid-State Photophysics and Charge Transfer of n,2-OBTTT Films.....	109
6.1 Overview of Experiments	109
6.2 Bulk n,2-OBTTT Properties and Single Crystal Studies	110
6.3 Thin films of n,2-OBTTT	114
6.4 Solid-State Photophysics of n,2-OBTTT Thin Films	118
6.4.1 Solid-State Absorption.....	120
6.4.2 Solid-State Film Photoluminescence	124
6.4.3 Selective Emission From H-like and J-like Absorption	128
6.5 Photoconductivity Studies of n,2-OBTTT	129
6.5.1 Microwave Mobility Contribution of n,2-OBTTT	129
6.5.2 n,2-OBTTT as an Electron Donor	132
6.5.3 Driving Force Between PCBM and Isolated n,2-OBTTT	134
6.5.4 Photoconductivity of PCBM/n,2-OBTTT Films	137
6.5.5 n,2-OBTTT as an Electron Acceptor	139
6.6 Studies of n,2-OBTTT as a High-Energy Sensitizer in P3HT/PCBM Blends	141
6.7 Conclusion	143
Chapter VII: The Role of Microstructural Effects in Photoinduced Charge Transfer Processes	145
References.....	148

List of Tables

Table 3-1. Comparison of as-cast and annealed samples with varying concentrations of soluble fullerenes. Fwhm correlation length is given along with the smectic layer spacing, d , for each sample. RL refers to an instrument resolution limited peak width. In each sample annealing led to a sharpening of the peak width.	52
Table 3-2. Enthalpies and temperatures of transition for various molar mixing ratios of PCBM and P-9-OPIMB.	56
Table 3-3. Temperatures of phase transitions in thin films of PCBM/P-9-OPIMB as compared to bulk P-9-OPIMB. The glass and isotropic transitions are significantly affected in the thin films, though the B2 transition is almost unchanged in all samples.	59
Table 5-1. Measured and calculated photophysical properties of the n,2-OBTTT series in toluene. Values show no variation between different molecules of varying tail length.	102
Table 5-2. Calculated energies of first and second oxidation and reduction relative to Fc^+/Fc	104
Table 5-3. Average values measured in this chapter for n,2-OBTTT molecules. No systematic change was seen for molecules with different tail lengths.	107

List of Figures

- Figure 1-1.** Solar spectrum showing wavelengths of light and average irradiance at the top of the Earth's atmosphere and at sea level along with the calculated black body radiation from the sun. Different molecular species are known to absorb sunlight in certain areas of the spectrum and are denoted on the graph. For maximum absorption an OPV device needs to have an absorption profile that closely overlaps with the solar spectrum. Image is from the Wikipedia Commons. ... 2
- Figure 1-2.** Molecular interactions of chromophores in solution lead to higher and lower energy transitions depending on the alignment of the transition dipole (blue arrow). J-aggregates originate from the slipped stack alignment and H-aggregates from parallel alignment of dipoles, the solid arrow represents an allowable transition and the dashed a forbidden transition. Ultimately J-aggregates show a lower energy absorption than the isolated molecule and H-aggregates show a higher energy absorption. 5
- Figure 1-3.** Energy levels of the charge transfer process in which the exciton energy, E_{ex} , ionization potential, IP, and electron affinity, EA, energy levels create a driving force. Charge transfer can occur through electron or hole transfer from an exciton on the donor and acceptor, respectively. It should be noted that the exciton energy is always less than the HO-LU gap. 7
- Figure 1-4.** Simple kinetic scheme indicating the pathways an excited species, D^* , can take. D^* can return to D through radiative relaxation, k_r , as fluorescence or undergo nonradiative relaxation, k_{nr} . In the presence of an electron acceptor species, A, D^* may now also couple to form a charge transfer state with A, CT, in which the pair are electronically coupled. The CT state can also decay through radiative and nonradiative relaxation leading to isolated and uncoupled D and A species. Or the CT state can fully separate to the D^+ and A^- ions in the charge separated state (CS). It is the latter process that leads to charge generation in a heterojunction. .. 8
- Figure 1-5.** Liquid crystal ordering is categorized into positional and orientational ordering. In the isotropic example A) there is neither positional nor orientational ordering. The nematic liquid crystal B) has orientational but not positional ordering and the smectic C) has both. These are two very simple examples of liquid crystallinity. 9
- Figure 1-6.** Examples of three basic liquid crystal-forming mesogens A) calamitic, B) discotic and C) bent-core. Interactions between the molecular structure, its shape and tail all lead to the formation of different phases. Calamitic mesogens form nematic and smectic phases. 10
- Figure 1-7.** Word cloud made from the text of this chapter, size of word corresponds to its frequency in the text. 14
- Figure 2-1.** Schematic of the resonant cavity used in the time-resolved microwave conductivity technique. An iris is used to create a cavity resonance. Figure supplied by Nikos Kopidakis at NREL. 19
- Figure 2-2.** The photoexcitation setup for the TRMC is a Continuum Precision II Nd:YAG laser that uses 10 Hz 355 nm excitation pulses to pump an Continuum Panther Optimal Parametric Oscillator (OPO) to generate light pulses with wavelength range (~410-2600 nm.) The excitation beam then passes through diffusers and neutral density filters before reaching the sample cavity. A uniform, diffuse laser pulse excites the entire sample surface. 21

Figure 2-3. Simplified schematic drawing indicating certain important parts of the time-resolved microwave conductivity setup including 1) the diffuse laser beam 2) the microwave cavity chamber with a selectively reflective front plate which keeps microwaves inside the chamber, 3) thin-film sample on a quartz substrate, 4) iris, 5) waveguide, 6) GHz microwave source, 7) circulator, 8) microwave detector, 9) amplifier, 10) Tektronix oscilloscope, 11) computer. 22

Figure 2-4. Example of the microwave cavity resonance plotting is shown. The voltage is recorded at various microwave frequencies to determine the resonance specific to the iris and sample. A Lorentzian function is fit to the resonance from which TRMC characterization parameters are determined (Q , K , τ) f_0 is the resonant frequency and R_0 the resonance depth. ... 24

Figure 2-5. Picture and simple diagram of the Shimadzu integrating sphere, as provided on the Shimadzu website. Transmission and reflectance measurements are both made using this setup. 26

Figure 2-6. Simple kinetic scheme indicating the relaxation pathways an excited species, D^* , can take. D^* can return to D through radiative relaxation, k_r , as fluorescence or undergo nonradiative relaxation, k_{nr} . In the presence of an electron acceptor species, A , D^* may now also couple to form a charge transfer state with A , CT , in which the pair are electronically coupled. The CT state can also decay through radiative and nonradiative relaxation leading to isolated and uncoupled D and A species. Or the CT state can fully separate to the D^+ and A^- ions in the charge separated state (CS). It is the latter process that leads to charge generation in a heterojunction. All processes aside from fluorescence from D^* are sources of photoluminescence quenching. . 30

Figure 2-7. Time-correlated single photon counting schematic, courtesy of Andrew Ferguson at the National Renewable Energy Laboratory. In the TCSPC technique a Fianium Supercontinuum laser pulse, at a repetition rate of 10 MHz, is passed through an AOTF to select the excitation wavelength and is then directed to the sample. The emission from the sample is directed to a monochromator, to select for a specific emission wavelength, and then into the detector. The signals are recorded with the Becker & Hickl SPC-130 TCSPC module. 31

Figure 2-8. Word cloud made from the most used words in this chapter. 36

Figure 3-1. Hierarchical self-assembly of an HNF mesogen: A) The molecular structure of the HNF mesogen P-9-OPIMB with the transition temperatures and phase sequence observed on heating and cooling; B) Illustration of the structure of a single twisted layer composed of HNF mesogens; C) Stacking of the twisted layers produces “twisted rod”-shaped HNFs ~ 30 nm in diameter. The final stage of the self-assembly (not shown) involves liquid crystalline ordering of the HNFs into an hexatic phase where the HNF twist is coherent. The HNF bulk phase is necessarily porous, since twisted rods as illustrated in C cannot fill space. 37

Figure 3-2. Freeze-fracture of P-9-OPIMB grown from 8CB, demonstrating the individual helical nanofilaments (A) as well as their ability to align and coherent twist growth (B). Image from Chen et al.¹⁴ 39

Figure 3-3. HNF's aligned with an induced temperature gradient. Hot samples are capillary filled into 10 μm channels of a Si substrate and exposed to a steady flow of gas as it cools. The HNFs align along the channels of the substrate. Image from Yoon et al.¹⁸ Such methods could be employed to align HNFs in a photovoltaic device, thereby creating a direct charge transfer pathway between electrodes. 40

Figure 3-4. a) At a glass surface, parabolic focal conics are common. In these surface-induced structures the twist is suppressed, and layers with positive curvature are seen. The curved smectic layers of P-9-OPIMB stack from a point defect. In this study by Chen et al. HNFs were observed to grow on top of the focal conics. Image from Chen et al.²² b) Toroidal focal conics, with negative curvature, are another commonly seen surface-induced structure obtained from films of P-9-OPIMB obtained by freeze-fracture..... 42

Figure 3-5. TEM images of as-spun and annealed P-9-OPIMB thin-films on quartz are presented. Images (A) and (B) are as-cast P-9-OPIMB films. Images (C) and (D) are annealed thin films. The texture of these images reveals surface topography obtained for a thin layer of Pt metal obtained by oblique incidence evaporation onto a cryo-cooled surface. The topography of the resulting Pt surface is essentially a replica of the organic thin film topography. HNFs are observed in the as-cast samples, in addition to the surface droplets. When annealed the films form surface-driven phases such as those shown in Figure 3-4. This differentiates between kinetic (as-cast) and thermodynamically (annealed) formed films..... 44

Figure 3-6. Thin films of P-9-OPIMB/PC₆₀BM composites made 50 wt%. Samples were annealed to different temperatures (A) 25 °C, (B) 150 °C and (C) 240 °C. In as-spun films HNFs are the dominant phase while the two annealed samples show varying degrees of lamellar phase, in which the mesogen tails are oriented normal to the air interface. 45

Figure 3-7. TEM images of 50/50 PCBM/P-9-OPIMB as-spun samples demonstrate parabolic focal conics, arising from concentric curved smectic layers. 47

Figure 3-8. Diffractograms of as-spun and annealed (to 165 °C) thin films showing Bragg scattering from the layers are shown, along with their Gaussian fits. d is the smectic layer spacing. XRD of as-spun film, shown above by TEM to be composed of HNFs, demonstrates a broader diffraction peak than the annealed film, this indicates a shorter correlation length. Only in the annealed P-9-OPIMB sample was a higher order diffraction peak detected 49

Figure 3-9. Schematic of HNF and lamellar packing illustrating the same layer spacing (green bar) a property measured with diffraction experiments. 53

Figure 3-10. Heating and cooling DSC curves of blends of PCBM and P-9-OPIMB are shown. All curves are the second heating and cooling cycle. On heating the HNF to B2 transition is nearly unchanged across the blend series, whereas the Isotropic transition is sensitive to PCBM doping. On cooling the phase transitions are nearly identical. 55

Figure 3-11. Enthalpy of phase transitions plotted against molar ratio of PCBM in P-9-OPIMB. The slopes of both enthalpies come close to crossing zero at 100% PCBM. 57

Figure 3-12. Thin films of annealed and as-cast P-9-OPIMB/PCBM films and bulk P-9-OPIMB. 58

Figure 3-13. Word cloud made from the most commonly used words from this chapter. 60

Figure 4-1. Thin film absorptance of P-9-OPIMB, PCBM and mixtures as measured in an integrating sphere. Annealed P-9-OPIMB/ PCBM thin films show a distinct broad absorption at 500 nm. 66

Figure 4-2. Solid-state photoluminescence of P-9-OPIMB films shows an emission peak at 440 nm. Slight differences are observed between the as-cast (orange) and annealed (blue) samples. 67

- Figure 4-3.** Figure from Cook et al. showing the CT-state emission and S_1 - S_0 emission of PCBM films of isolated (grey) and aggregated (black) PCBM molecules. $\lambda_{ex}=433$ nm.²² 69
- Figure 4-4.** Absorption and photoluminescence of P-9-OPIMB/PCBM films annealed to three different temperatures, red is as-cast (annealed to 25°C), green is 150°C and blue is annealed to 240°C. The absorption of the CT state increases with increasing annealing temperature and the PL quenching rates decreases with increasing annealing temperature. 70
- Figure 4-5.** Yield-mobility product transients ($\Phi\Sigma\mu$) for films of neat C_{60} and bilayers of C_{60} on P-9-OPIMB nanofilaments. The P-9-OPIMB/ C_{60} sample has a 95x larger yield-mobility signal indicating a generation of photo-induced charges. 71
- Figure 4-6.** TRMC of P-9-OPIMB and C_{60} bilayer films. Extrapolated $t = 0$ signal measured and plotted over different light intensities. The A value of the modified Dicker fit for the P-9-OPIMB/ C_{60} bilayer is 0.166 and 0.00240 for the C_{60} film. 74
- Figure 4-7.** P-9-OPIMB, PCBM and 1% PCBM in P-9-OPIMB films measured with TRMC at different light intensity..... 77
- Figure 4-8.** Yield-mobility product of 1% PCBM in P-9-OPIMB excited at 420 nm and 355 nm. The decrease in signal is attributed to P-9-OPIMB absorbing light at 355 nm at the expense of the PCBM absorption..... 78
- Figure 4-9.** Comparison of the yield-mobility product for the same film of PCBM excited at different wavelengths. The difference in signal is within the error range of the measurement.... 79
- Figure 4-10.** Similar to the charge generation results from the HNF- C_{60} bilayer the HNF heterojunction thin films confirms that HNFs act as a “good charge-generating interface”. In addition to the increase in $t = 0$ signal. The HNF heterojunctions have much longer-lived charges (inset). 80
- Figure 4-11.** Normalized TRMC transients over different light intensities in A) HNF heterojunction sample of P-9-OPIMB and PCBM and B) a lamellar microstructured heterojunction of the same components..... 82
- Figure 4-12.** Yield-mobility product of heterojunction samples as a function of annealing temperature. The yield-mobility product decreases with increasing annealed temperature. 83
- Figure 4-13.** Photoconductivity decay comparison of P-9-OPIMB/PC₆₀BM samples annealed to various temperatures between room temperature and 240°C. All photoconductance transients excited at 420 nm with an absorbed flux of 1×10^{13} photons/cm². 84
- Figure 4-14.** P-9-OPIMB/PC₇₀BM HNF and lamellar heterojunctions microwave absorption measured at different light intensities and compared to neat PC₇₀BM. Photoinduced electron transfer does not occur. 85
- Figure 4-15.** Word cloud constructed from commonly used words in this chapter..... 87
- Figure 5-1.** Molecular structures of PBTTT and the newly designed and synthesized model compound, n,2-OBTTT, characterized in this work, where $R = C_nH_{2n+1}$ and $n = 1-13$. The photophysical and electrochemical properties show no variation between molecules with different tail lengths. 88

- Figure 5-2.** Simplified schematic depicting three different dissolved polymers in solution, A) the non-interacting polymer, B) polymer chains interacting and C) clustered polymers. Polymers exhibit clustering to different degrees in different solvents, in particular the intermolecular interactions in clustered polymer chains can lead to a shifting of properties, e.g. H- or J-aggregation..... 90
- Figure 5-3.** Target PBTTT-inspired small molecule mesogens designed to form helical nanofilaments. The arm units are identical to those characterized herein, with two different core units that are used in other HNF-forming mesogens. 92
- Figure 5-4.** Normalized absorption spectra of 1,2-OBTTT in various solvents compared to PBTTT. Solvent is shown to have minimal effect on the absorption profile. The small molecule absorption is blue-shifted (410 nm) from the polymer absorption (540 nm). 93
- Figure 5-5.** Normalized absorption curves of n,2-OBTTT in toluene demonstrate the general absorption shape uniformity across the series, though a subtle shift in the peak absorption is seen to vary, shifting to lower energy with increasing tail length. 95
- Figure 5-6.** Photoluminescence spectra of 1,2-OBTTT in different solvents indicate a change in stokes shift between the molecules in toluene and chloroform/dichlorobenzene. The latter solvents have a higher dielectric constant compared to toluene. 96
- Figure 5-7.** Normalized absorption and emission of n,2-OBTTT in chloroform. The arrows are a guide to the eye demonstrating the subtle shift of absorption and emission to higher energies with increasing tail lengths. 97
- Figure 5-8.** Measured relative quantum yields of the model compounds in toluene are plotted versus tail length, indicating a lack of quantum yield trend with tail length. The dashed line corresponds to an average across the series for contrast..... 98
- Figure 5-9.** Time-resolved photoluminescence of the n,2-OBTTT series shown with the instrument response function, I.R. (dashed line). The signals of all n,2-OBTTT molecules are indistinguishable thus the rate of radiant emission is not changing with different tail lengths. . 100
- Figure 5-10.** Voltammograms of n,2-OBTTT n = 1, 4, 7, 10, 13, showing electrochemical reduction on the right and oxidation on the left. The oxidation and reduction potentials are calculated relative to the Fc⁺/Fc peak, which is added to the sample as an internal reference. The average E_{red} is -1.75 V. The average first and second oxidation potentials are 0.46 V and 0.70 V. 103
- Figure 5-11.** Oxidation voltammogram of 1,2-OBTTT demonstrating the cathodic and anodic peak energies indicated, E_{pc} and E_{pa}, along with the determination of E_{1/2}, dashed line. E_{1/2} is used to determine the E_{red} and E_{ox} potentials. 104
- Figure 5-12.** Relative HOMO and LUMO values for the n,2-OBTTT molecules and some common OPV electron donors and acceptors as measured electrochemically. The molecules studied herein fall into a range to exhibit favorable electron transfer to PCBM and also act as an electron acceptor with the conducting polymers, PBTTT and P3HT. The energy axis is left blank to indicate the general uncertainty in converting solution measured electrochemical energies to solid-state HOMO/LUMO values. 106

- Figure 5-13.** Chapter 5 word cloud, word size corresponds to its frequency in the text and this figure is included in case you don't want to read the entire chapter, but it mostly is nonsense so you should probably just go ahead and read the chapter. 108
- Figure 6-1.** Unit cell axes of the 3,2-OBTTT crystal structure, letters correspond to viewing the crystal down the axes, a) shows the general herringbone packing in the crystal, b) and c) elucidate the layers formed in the crystal. 111
- Figure 6-2.** Unit cell axes of the 9,2-OBTTT crystal structure, letters correspond to viewing the crystal down the axes, a) and b) shows the general herringbone packing in the crystal, and b) and c) elucidate the presence of sheets of alternate tail-direction. The slipped chromophores in these sheets are proposed to lead to specific absorption trends. 112
- Figure 6-3.** Expanded unit cell along the c axis of 9,2-OBTTT demonstrates the alternating direction of pairs of 9,2-OBTTT molecules. Molecules are all tilted into the plane. 113
- Figure 6-4.** Diffraction of annealed n,2-OBTTT thin films on quartz. Diffraction spacing, q , is highly dependent on the tail length and consequently shows the layer spacing is increasing with tail length. 115
- Figure 6-5.** Calculated powder pattern made in Mercury from the measured single crystal data (dashed line) and measured thin film (solid line). The calculated powder peak location varies substantially from the thin film XRD. In the case of the shorter-tailed homologue, the larger q peak matches closely with the calculated diffraction pattern, indicating a similar packing geometry to the single crystal. In the longer tail homologue the diffraction spacing differs substantially, the calculated peak at $q = 2.5 \text{ \AA}^{-1}$ is from a smaller layer spacing than either of the measured diffraction peaks. 116
- Figure 6-6.** Measured powder X-ray diffraction spacing from thin films (red circles) is compared to the calculated powder diffraction (black squares) and the extended molecular length (blue open circles.) The measured thin film diffraction shows layer spacing just larger than that of the molecular length, indicating that the molecules exist in untilted layers of molecules. 117
- Figure 6-7.** Simplified examples of chromophore interaction effects on molecular absorption, solid and dashed lines represent allowed and forbidden transitions respectively. The blue oval represents the chromophore in which the black arrow is the absorption transition dipole. Parallel orientation of the dipoles leads to an allowed transition to higher energy. Slipped dipole alignment, J-aggregate, leads to a lower energy absorption. In more complicated (and common) crystal orientations both transitions are allowable to varying degrees. 119
- Figure 6-8.** Thin film absorption for dropcast films of the n,2-OBTTT series between glass slides annealed to 200 °C. A peak is seen at about 340 nm with a shoulder extending out to ~ 550 nm. The solution absorption is also shown for comparison. The film thickness varies some between different samples, but notably the 2,2-OBTTT shows a less intense low-energy shoulder and the absorption edge ~550 increases with increasing tail length. 120
- Figure 6-9.** Ratio of the peak magnitudes of the H- and J-like absorption features, 340 and 450 nm respectively shows a lack of tail length trend, although again 2,2-OBTTT is anomalous. The ratio is also used to account for differences in film thickness. 122

Figure 6-10. The absorption edge, determined from a fit to the absorption edge, of the lower energy “J-like” transition is plotted against tail length. The absorption edge is determined by fitting a line to the steep shoulder and extracting this value to the baseline. The absorption edge shifts to a lower energy as tail length increases. This indicates that there is a systematic effect of tail length on the intermolecular packing..... 123

Figure 6-11. Thin film photoluminescence shown for the n,2-OBTTT, with n = 2 – 13, series excited at 355 nm. For all films measured two peaks were observed, a peak at 420 nm from a weak emission and a much more intense peak at ~550 nm. The peak location of the higher energy peak (420 nm) remained constant for different tail lengths while the lower energy (~550 nm) peak shifts to longer wavelengths (lower energy) with increasing tail length. 124

Figure 6-12. Peak emission wavelength (blue circles) and absorption edge wavelength (red crosses) plotted versus the tail length of the n,2-OBTTT mesogens. Both features follow the trend that increasing tail length leads to lower energy features. The absorption shoulder can be used to account for the change in emission wavelength for different tail lengths..... 125

Figure 6-13. Schematic summarizing the absorption trends from the H-like and J-like split S_1 energy levels are shown for different tail lengths. The dark blue and orange levels indicated the optically active level of the transition, while the semitransparent bars indicate the inactive transition. The H-like transition, blue bar, originates from parallel dipole alignment and is unchanged with tail length. The J-like energy level, orange, is shown to decrease in energy with increasing tail length. 126

Figure 6-14. Proposed scheme for the source of H- and J-like spectral features using cartoon molecules, the orange oval represents the chromophore and the line represents an alkoxy tail. The dipole alignment of the chromophore in the b and c directions leads to the H-like absorption (which was observed to **not** vary with tail length.) Whereas the slipped orientation of the dipoles is leading to the J-like absorption, the varying degree of slipped leads to the different total splitting in the energy level (the longest tails have the most-slipped dipoles and thus the lowest energy transition.) 127

Figure 6-15. Photoemission is shown from two different excitation wavelengths in a sample of as-cast 2,2-OBTTT, 350 nm and 450 nm, indicated with arrows. The inset graph depicts the difference between the two PL emissions demonstrating a peak at 550 nm, which originates solely from the 350 nm absorption. 128

Figure 6-16. A maximum yield-mobility product for samples of neat n,2-OBTTT excited at 430 nm (2×10^{13} photon/cm²) is plotted for several films demonstrating the lack of variation in yield-mobility between tail lengths. This is used to demonstrate that the microwave carrier mobility of n,2-OBTTT is constant between different tail lengths..... 130

Figure 6-17. Yield-mobility product transients of a neat 9,2-OBTTT film excited at 420 nm with different light intensities. A fast and slow decay component is observed for generated charges. 131

Figure 6-18. Photoconductance transients of n,2-OBTTT (n = 2, 3, 6, 8, 11, 12) with 2 mol% PCBM as an electron acceptor, photoexcited at 430 nm at $\sim 1 \times 10^{13}$ absorbed flux, left. Yield-mobility products are shown on the right indicating subtle differences with fluence. Maximum yield-mobility products are shown to decrease with increasing tail length. Recall that the charge

carrier mobility was the same across different tail lengths making the difference in yield-mobility product here actually a difference in yield. Thus the tail length is leading to a difference in the total quantity of charges generated. 132

Figure 6-19. Photoconductance transients of 99 mol% PCBM doped with various n,2-OBTTT molecules (left) excited at 430 nm, the end-of-pulse (EOP) and extracted $t=0$ values for the same films are shown in the right plot, all fluences are $\sim 1 \times 10^{13}$ photons \cdot cm $^{-2}$. No systematic difference is seen in the EOP data, and a very slight trend with increasing yield as tail length is increased is seen in the fit and extracted $t = 0$ data. This trend is actually opposite that seen in the 2% PCBM and n,2-OBTTT blends and thus does not account for the yield/tail length difference in figure 6-18. 134

Figure 6-20. Maximum yield-mobility product for samples of 2 mol% PCBM in different n,2-OBTTT sample ($n = 2, 3, 6, 8, 11, 12$) plotted against the measured exciton energy for each n,2-OBTTT film. The microwave mobility is unchanged for different tail lengths, making the yield-mobility product effectively a comparison of yields. The exciton energy is shown to substantially affect the driving force of the charge transfer process, and is particularly dependent on the extent of J-like aggregation in the sample. 136

Figure 6-21. Photoconductance transients of 50/50 mol% mixtures of n,2-OBTTT/PCBM heterojunction excited at 430 nm (fluence 1×10^{12} photons/cm 2). The driving force dependent yield-mobility product observed in the low molar PCBM loading studies is not duplicated for these 50/50 heterojunctions. All samples studied here ($n = 2, 3, 6, 8, 11$ and 12) except $n = 11$ show high yield-mobility products. 137

Figure 6-22. Yield-mobility product plots of the same n,2-OBTTT/PCBM heterojunctions photoexcited at various intensities of 430 nm light. 138

Figure 6-23. Normalized transients of the PCBM/ n,2-OBTTT films used to show the relative lifetimes of charges in blends of the different homologues. Notably, 139

Figure 6-24. Transients of 2,2-OBTTT and 11,2-OBTTT mixed with P3HT (50 wt%) and neat P3HT to compare generation yields in thin films photoexcited at 430 nm. Both tail lengths act as electron acceptor and undergo photoinduced charge transfer with P3HT. 140

Figure 6-25. TRMC yield-mobility product diagram of optically dense film of a P3HT/3,2-OBTTT heterojunction photoexcited at 420 nm. This was shown to be a very high yield-mobility sample, it is likely that both components contribute to the mobility product and thus a yield cannot be extracted. 141

Figure 6-26. Yield-mobility product to compare two heterojunctions of P3HT/PCBM, one containing 2,2-OBTTT and the other without. The 2,2-OBTTT is acting as a high-energy sensitizer in the prototypical heterojunction blend. The carrier dynamics of the sample appear unchanged with the additive but the total yield is over 2x higher with the small molecule. 142

Figure 6-27. Just in case you weren't yet tired of seeing the word 2-OBTTT, I included this word cloud, based on the most used words in the chapter (some of them are pretty generic, it figures.) 144

Chapter I: Introduction and Motivation

1.1 Introductory Remarks

Intermolecular interactions present in organic solids greatly affect both optical and electronic properties. Deceptively minor structural modifications can lead to appreciable differences in the resulting properties. Such solid-state effects require consideration in the design and study of organic materials for use in solar energy harvesting. This work strives to systematically quantify the effect of chemical structure modifications and processing conditions on the solid-state microstructure of small molecular based organic thin films.

1.2 Organic Photovoltaics Active Layers

Organic photovoltaics (OPV), the term consistently used in this work, is a technology known by many names including organic solar cells, plastic solar cells, excitonic solar cells, all which can be further separated into subcategories, including polymeric, small-molecule, bilayer, heterojunction, solution-processable, seemingly ad infinitum.¹⁻⁹ The breadth in nomenclature, although at times confusing, displays the versatility of organic materials in solar energy applications. The classically touted benefits of organic photovoltaics are the decrease of production costs relative to inorganic-based devices, leading to more-affordable solar energy, and the production of flexible solar devices with the possibility to diversify solar energy deployment.^{1, 9} With respect to the work herein, perhaps the most important aspect of organic photovoltaics research is that photoinduced charge-generation in organic photovoltaic is not wholly understood, thus posing it as an intriguing and valuable research topic.^{2, 4, 10, 11}

Despite the many varieties of materials and techniques used, charge generation in organic photovoltaics are all described and constrained by certain physical phenomena. In this work the three components most relevant to the photovoltaic charge generation process are 1) light absorption, 2) exciton diffusion, and 3) charge generation through exciton dissociation; each will be described in more detail in the following paragraphs. It should be noted that additional processes of charge transport to and extraction at the electrode interfaces in devices is not trivial^{8, 12-14} but herein specific fundamental properties of charge generation in a device active layers are being studied and therefore a thorough description of charge extraction through electrodes is not provided.

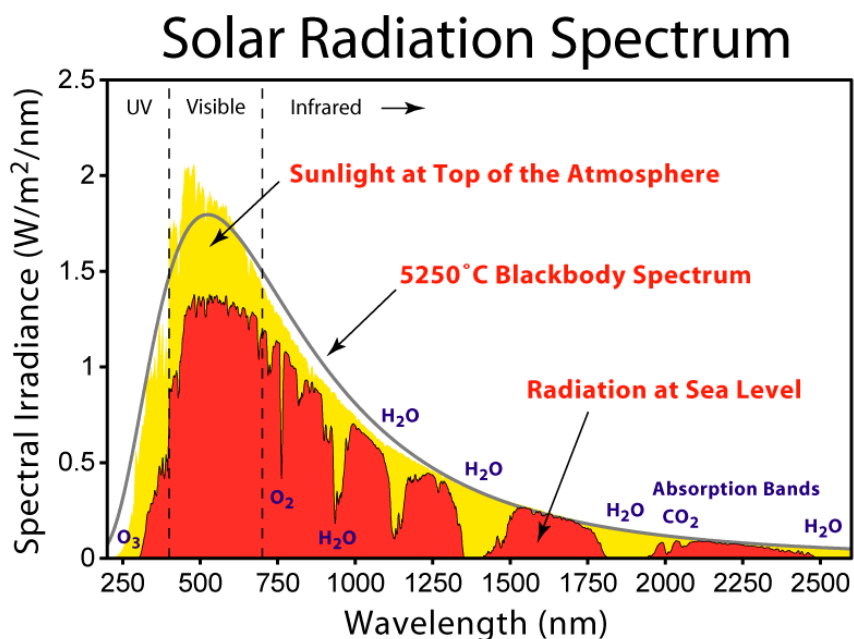


Figure 1-1. Solar spectrum showing wavelengths of light and average irradiance at the top of the Earth's atmosphere and at sea level along with the calculated black body radiation from the sun. Different molecular species are known to absorb sunlight in certain areas of the spectrum and are denoted on the graph. For maximum absorption an OPV device needs to have an absorption profile that closely overlaps with the solar spectrum. Image is from the Wikipedia Commons.

Typical OPV devices are composed of electron donor and acceptor materials combined in either blended heterojunctions or discrete bilayers.² To most effectively use the available solar resources the device absorption profile should closely overlap with that of the solar spectrum, Figure 1-1. Light absorption may occur in either the donor or acceptor layer; but often both are needed to overlap with more of the solar spectrum.^{1, 8, 15}

Description of light absorption is simplest by first considering the molecules isolated in the gas phase. In molecules electrons exist in molecular orbitals that are delocalized between several atoms on the molecule. The energy of the electronic ground state is associated with the energy of the highest occupied molecular orbital with energy, E_{HO} . This is also called the ground singlet level, denoted by S_0 in this work. Higher energy molecular orbitals also exist in the molecule but are empty in the ground state; the lowest energy molecular orbital that does not contain an electron is called the lowest unoccupied molecular orbital with energy E_{LU} . The difference in energy of the HO and LU molecular orbitals represents the energy needed to move an electron between them. Accordingly this energy is the energy of light that can be absorbed by the molecule, which leads to the molecule to exist in the first excited singlet state, S_1 . The probability of a light absorption event is significantly more complicated and beyond the breadth of this work. The energy of light absorbed is typically reported as a spectrum in either wavelength (nm) or energy (cm^{-1} or eV.) In solution, the energy of the ground state and, more often, excited state molecular orbitals can be shifted by either favorable (energy lowering) or unfavorable (energy raising) interactions between molecule and solvent.

In dimers of chromophores in solution as well as larger aggregates interaction between adjacent transition dipoles leads to a splitting of the S_1 state, as drawn in Figure 1-2. The degree

of splitting is dependent on the relative orientations of the transition dipoles, their separation distance, and the dielectric constant of the medium (e.g. the solvent.)¹⁶ Aggregates in solution have been extensively studied and are called H-aggregates when the dipoles are parallel, a reference to the Hypsochromic shift (blue-shift), and J-aggregates when a slipped stacking leads to a lower energy transition.¹⁷ Noticeably in Figure 1-2, a higher and lower energy state exist in both alignments from the split S_1 state (as a result of the dimer) but the energy of transition and transition dipole are not directly related. The energy splitting occurs from a Van der Waals interaction between the excited monomer and the ground state monomer (as a linear combination of states.) The transition dipole (oscillator strength) is the sum of the individual dipole moments. For the case of the J-aggregate, with dipole moment, m , the lower energy state is made of the aligned head-to-tail dipoles, which has oscillator strength of $2m$, and the higher energy transition is 0. Thus J-aggregates have allowable transition to the lower energy state. But in the case of the H-aggregate, the “aligned dipoles” configuration is higher in energy, the lower energy transition is made up of dipoles in opposite directions, but when added together give an oscillator strength of 0 (forbidden transition). So H-aggregates solely absorb into the higher energy state.¹⁸

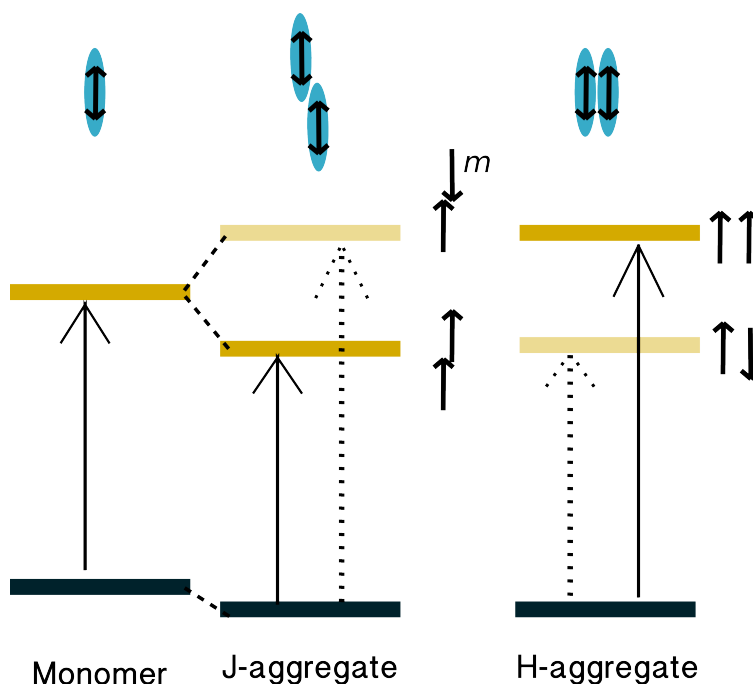


Figure 1-2. Molecular interactions of chromophores in solution lead to higher and lower energy transitions depending on the alignment of the transition dipole (black arrow). J-aggregates originate from the slipped stack alignment and H-aggregates from parallel alignment of dipoles, the solid arrow represents an allowable transition and the dashed a forbidden transition. Ultimately J-aggregates show a lower energy absorption than the isolated molecule and H-aggregates show a higher energy absorption.

Similar to the differences observed in the clustered H- and J-aggregates in solution, solid-state interactions can significantly influence the energy of absorption. The relative orientations of chromophores in the solid also lead to H- and J-like aggregate dipolar interactions, but unlike that observed in solution aggregates (or that shown in Figure 1-2) 3-dimensions of dipole interactions lead to allowable higher and lower S_1 energies.^{19, 20} Recall that absorption results in the promotion of an electron between the ground and excited state molecular orbitals. It is also possible in close-packed molecular crystals for an exciton to delocalize across multiple molecules, which would also lead to a distinctly lower-energy absorption relative to the monomer.²¹ In this work, molecular orientation is proposed to give H- and J-like transitions to

varying extents dependent on the molecular tail length and the varying microstructures (orientation and distance of neighboring chromophores).

Once light absorption has occurred and a molecule is excited (forming an exciton) the exciton must move towards an interface for a useful charge transfer to occur. Due to the low dielectric constant of organic materials most organic semiconductors generate Frenkel excitons, in which the electron and hole are coulombically bound and move together. Excitons are uncharged species and are not affected by an electric field, thus their movement in a solid is described as diffusion. It is suggested that exciton diffusion occurs primarily through long-range energy transfer.³ Though a higher degree of crystallinity has been correlated to longer exciton diffusion distances.^{22, 23}

The last aspect of charge generation in OPV that will be described here is the process of charge transfer between the donor and acceptor species. The previously described HO and LU orbital energies make a reappearance to participate in the charge transfer process. For charge transfer to be favorable the donor and acceptor must fulfill certain requirements, a simplified energy level diagram is included in Figure 1-3. The driving force for the electron transfer is related to the energy differences from the initial and final states such that Equation 1-1 describes ΔG .^{3, 4} A successful driving force requires a sufficiently high electron acceptor electron affinity (EA) and low donor ionization potential (IP) and well-suited exciton energy, E_{ex} . Assuming that the exciton originates on the electron donor, though the exciton could be on either species, the promoted electron is in the LU orbital of the donor (making movement of an electron to the LU orbital on the acceptor a decrease in energy.) The electron moves to the LU_A and leaves a hole on the donor, and then the charges are separated.

$$\Delta G = IP_D - EA_A - E_{ex}$$

Equation 1-1

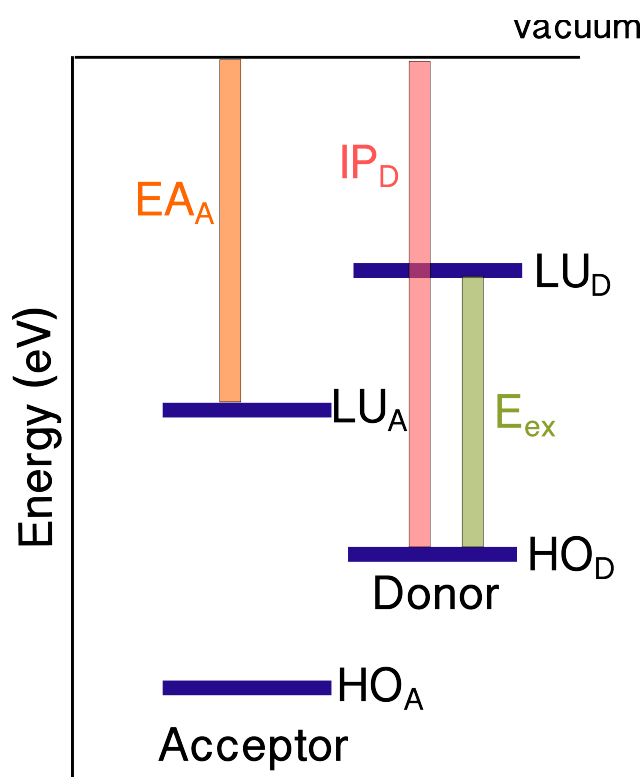


Figure 1-3. Energy levels of the charge transfer process in which the exciton energy, E_{ex} , ionization potential, IP , and electron affinity, EA , energy levels create a driving force. Charge transfer can occur through electron or hole transfer from an exciton on the donor and acceptor, respectively. It should be noted that the exciton energy is always less than the HO-LU gap.

As mentioned the exciton could be generated on either the donor or acceptor. If the exciton is on the donor an electron transfers from the LU_D to the LU_A . If the exciton is on the acceptor then a hole transfers from HO_A to HO_D . These processes can both happen in a device, though the driving force is not equivalent because the exciton energies differ between the donor and acceptor species.

Charge transfer can be more complicated than this simplified description, the exciton can also energy transfer between the donor and acceptor which can be either beneficial or detrimental depending on whether the electron or hole transfer is more efficient.¹¹ Electronic coupling

between the donor and acceptor can lead to charge transfer states. Charge transfer states have been proposed to be an intermediate towards separated charges.^{2, 3, 10} But it can also act as a charge trap if the charges remain coulombically bound which could lead to geminate charge recombination (in which an electron recombines with its own hole). This is visually described in the kinetic scheme in Figure 1-4.

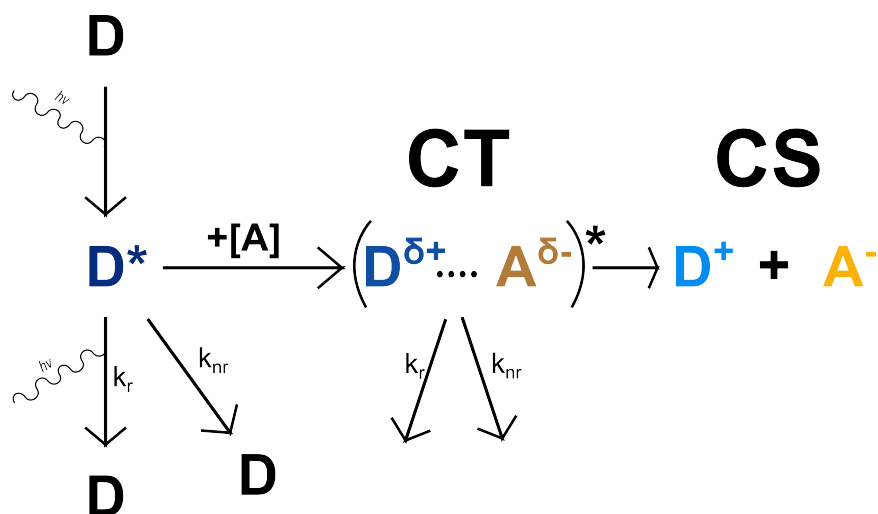


Figure 1-4. Simple kinetic scheme indicating the pathways an excited species, D^* , can take. D^* can return to D through radiative relaxation, k_r , as fluorescence or undergo nonradiative relaxation, k_{nr} . In the presence of an electron acceptor species, A , D^* may now also couple to form a charge transfer state with A , CT , in which the pair are electronically coupled. The CT state can also decay through radiative and nonradiative relaxation leading to isolated and uncoupled D and A species. Or the CT state can fully separate to the D^+ and A^- ions in the charge separated state (CS). It is the latter process that leads to charge generation in a heterojunction.

In each process described sample microstructure is highly important to light absorption, exciton diffusion and donor-acceptor charge transfer. These properties are difficult to “design” into a system and are even more rarely systematically varied to be able to study the effect on microstructure on a particular part of the process. Here I have characterized two small molecule systems with systematic variations that allow us to isolate different microstructures and their effect on charge transfer.

OPV is a field primarily driven by the externally motivated goal of creating efficient devices rather than a fundamental investigation of physical properties for the purpose of understanding. Incidentally the most common way to create efficient devices is a trial-and-error approach achieved via a seemingly haphazard combination of donor and acceptor materials, often resulting in stepwise improvements to known systems. This leads the OPV field to be a particularly positive-result biased field, leaving gaps in knowledge about materials systems that do not “work” or the reasons for which they do not “work”. In this thesis an intentional effort is made to study the changes of physical properties with systematic microstructural variation.

1.3 Organic Liquid Crystals and Crystals

The small molecule materials studied in this work are all mesogens, meaning that they undergo liquid crystal transitions, though the liquid crystallinity is not the focus of the work. Here a brief description of liquid crystals is presented as relevant to this text.

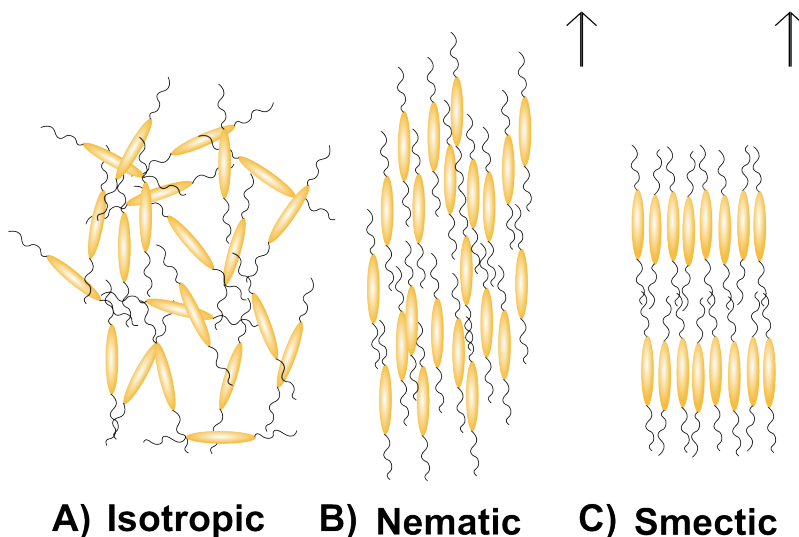


Figure 1-5. Liquid crystal ordering is categorized into positional and orientational ordering. In the isotropic example A) there is neither positional nor orientational ordering. The nematic liquid crystal B) has orientational but not positional ordering and the smectic C) has both. These are two very simple examples of liquid crystallinity.

Liquid crystal phases exist between isotropic and crystalline phases. In a purely isotropic array of molecules there is no correlation between the molecular directors of neighboring molecules, i.e. the director average taken across any portion of the sample would be zero, such in the isotropic example in Figure 1-5. Additionally, in a system with no positional ordering the distributions of centers of mass (COM) will be random and equivalent for any direction. Now consider the orientation of an oblong molecule, if that molecule contained a preferential orientation, but still no positional order, a nematic liquid crystal phase would be formed (Figure 1-5B.) In a positionally-ordered system the COM distribution will be preferentially found in one plane as compared to all others such as the sheets of molecules formed by Smectic liquid crystals, as depicted in Figure 1-5C. Thus liquid crystals contain different orientational and positional degrees of ordering. Nematics and Smectics are two very simple examples of liquid crystals.

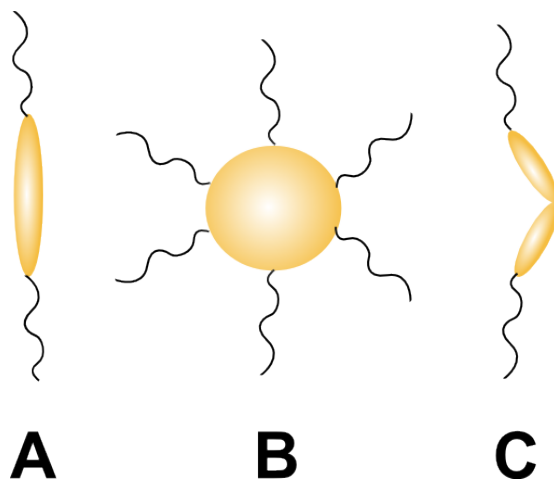


Figure 1-6. Examples of three basic liquid crystal-forming mesogens A) calamitic, B) discotic and C) bent-core. Interactions between the molecular structure, its shape and tail all lead to the formation of different phases. Calamitic mesogens form nematic and smectic phases.

Different types of mesogens exist that lead to the formation of different phases including calamitic, discotic and bent-core, as shown in Figure 1-6. Calamitic (Figure 1-6A) mesogens are

one- and two-tailed molecules with a core made of aromatic rings and form nematic and smectic phases, such as those depicted in Figure 1-5. The term smectic is a general term that refers to a molecular structuring that contains positional and orientational ordering in layers such as those shown in Figure 1-5, but many different smectic phases exist. Flat aromatic molecules that have several tails attached around the core are discotic mesogens (Figure 1-6B). These molecules also form nematic phases in addition to the more characteristic columnar phases. Columnar phases form from the flat molecules stacking on top of one another to form molecular pillars, similar to smectic phases many types of columnar phases exist. The final mesogens that will be mentioned are the bent-core mesogens (Figure 1-6C). It is very similar to a calamitic mesogen except for the presence of a rigid bend in the core of the molecular structure.²⁴ Certain bent-core mesogens may also form smectic phases but the bent-core liquid crystal mesogens class forms its own phases, including the helical nanofilament (HNF) phase that will be considered in chapters 3 and 4.²⁵⁻³⁰

The degree of orientational and positional ordering within liquid crystalline phases has led to their study as charge transport materials. In particular high charge carrier mobilities have consistently been measured for an assortment of crystalline and low-temperature phases.^{14, 31-33} Columnar phases, with significant areas of π - π overlap in the cores, have shown very high charge carrier mobilities, up to $6.7 \text{ cm}^2 \text{V}^{-1} \text{s}^{-1}$.³⁴⁻³⁶

Even in thoroughly characterized systems of well-known liquid crystal phases, the creation of thin films can change the intermolecular structuring. It behooves the researcher to study the liquid crystalline material as both a bulk (thick film) and a thin film if using the material in an application such as OPV.

1.4 This Work

The chapters of this thesis break down by two classifications, the characterization methods and/or the type of materials being studied. The initial project was carefully and deliberately chosen to expound on previous and present work in the Liquid Crystal Materials Research Center (LCMRC) at the University of Colorado –Boulder, and is included in chapters 3 and 4. This is the first time the helical nanofilament phase has been studied for use as an order heterojunction material, necessitating the characterization of the heterojunction microstructure in addition to photoinduced charge transfer. Chapter 3 contains the structural description of the helical nanofilament phase when processed into thin films, specific techniques include the use of calorimetry, surface imaging and diffraction experiments. Samples are made of spincoated solutions of neat P-9-OPIMB and as mixtures with soluble fullerenes that are processed under different temperature conditions. Three microstructures of the mesogens are uncovered and described. The most notable result is that the as-cast samples display helical nanofilaments, even when mixed with fullerenes, but when annealed all samples switch to surface-driven flattened layers thus demonstrating a distinct difference between the kinetically and thermodynamically formed phases.

Continuing on studies of the helical nanofilament phase, chapter 4 uses the time-resolved microwave conductivity (TRMC) technique, along with solid-state absorption and photoluminescence to quantify the photophysical effects of the microstructures described in chapter 3. In these studies TRMC is used to quantify photoinduced charge transfer yields in bilayers and different heterojunction microstructures. Most notably the bilayer films of HNFs and C₆₀ were measured to convert 100% of absorbed photons to charges.

The materials studied in chapters 3 and 4 have been extensively described but this thesis also includes work for the characterization of new materials. Chapter 5 contains a basic yet thorough photophysical description of a novel small molecule thiophenes series, n,2-OBTTT. The novel molecule was designed from the monomer unit of Poly[2,5-bis(3-tetradecylthiophen-2-yl)thieno[3,2-b]thiophene] (PBTTT), a highly conductive polymer, and the series includes molecules with different alkoxy tail lengths, n, ranging from very short methoxy (CH₃) tails to long tridecoxy (C₁₃H₂₇) tails. The solution characterization showed no systematic changes across the series, fundamental photophysical and electrochemical properties are reported in this chapter including absorptivity, quantum yields, fluorescence rates, and oxidation and reduction potentials.

The final results chapter of this work, chapter 6, chronicles a new and exciting heterojunction project. Solid-state characterization of n,2-OBTTT thin films across the different tail lengths shows appreciable differences in the microstructure of the films. The microstructural differences lead to systematic variation in the photophysics of the film as well as a difference in exciton energy, E_{ex} . The photoinduced charge transfer yield in mixtures with PCBM is shown to vary with tail length and is postulated to be dependent on the driving force, ΔG . N,2-OBTTT is shown to act as an electron donor and acceptor with prototypical OPV materials. The system is finally used as a high-energy sensitizer in P3HT/PCBM bulk heterojunction blends which is shown to increase the yield-mobility product relative to blends without the dopant.

Several key findings can be distilled from the culmination of this work including 1) that thin films are especially susceptible to the competition between kinetically and thermodynamically formed phases and 2) that thin film microstructures have significant

Chapter II: Experimental Methods and Data Analysis

2.1 Overview of Experiments and Analysis

The work in this dissertation utilizes several experimental techniques to characterize and realize the microstructure and photophysics of small molecular electron donor-acceptor systems. This chapter will describe and present background information on several of the most important techniques to the work. Time-resolved microwave conductivity (TRMC) is the most prominent and distinctive technique used in this work and is therefore addressed first. This transient photoconductivity technique follows the absorption of a standing microwave during and after photoexcitation to yield information about photogenerated charges and their mobility. The technique relies on accurate thin film absorption values, which is also described. Basic photoluminescence techniques are used to measure radiative emission, excited-state lifetimes and fluorescence quenching, including steady-state and time-resolved photoluminescence techniques and are also described. Powder x-ray diffraction and differential scanning calorimetry experiments and their use to study thin-film microstructure are described. Finally the sample preparation is described.

2.2 Flash-photolysis Time Resolved Microwave Conductivity

Time Resolved Microwave Conductivity (TRMC) is a pump-probe method primarily useful as an electrode-less photoconductivity technique used to detect photo-induced charges in low conductivity semiconductor samples. The technique has successfully been used to characterize dye-sensitized solar cells, organic photovoltaic active layers, quantum dots and

nanocrystalline systems, and more.^{13, 37-40} TRMC operates from the principle that mobile charges absorb microwaves. Time-resolution is achieved by monitoring the microwave power before excitation, as a baseline, during excitation, as charges are generated, and in the time after as charges recombine, trap and otherwise decay.

In chapter 4, TRMC is used to study the effectiveness of the helical nanofilament surface as a charge-generating surface. In chapter 6, TRMC is used to quantify the tail-length effects on photo-induced charge yield in small molecule-fullerene blends.

Time-resolved microwave conductivity measurements were taken on a homebuilt setup. Photoexcitation was from Continuum Precision II Nd:YAG laser and a Continuum Panther OPO at a repetition rate of 10 Hz. A Tektronix DPO 7254 Digital Phosphor Oscilloscope was used to record the electrical signal. The microwave signal was generated with a Midcentury MC16/34B Gunn diode and detected with a Philips Sievers PM7195X Schottky barrier diode. The signal is amplified with a HAS-X-1-40 Laser Components high-speed amplifier.

2.2.1 Fundamentals of TRMC

This technique differs from other carrier mobility and conductivity measurements as it is a localized, nanoscale measurement in comparison to device carrier mobility measurements such as field effect transistors, charge-extraction by linearly increased voltage, time-of-flight conductivity among others. These traditional bulk methods detect carrier mobility by measuring a current across the sample, under the influence of an applied electric fields, occasionally accompanied by a charge-generating light source.⁴¹ Because the electrons sample an entire path between the electrodes, these techniques are sensitive to grain boundaries, defects and ultimately give bulk-values for charge carrier mobility that correlate to the slowest carrier pathway. In

comparison, TRMC utilizes the oscillating microwave as an AC charge detection, similar to terahertz spectroscopy techniques,⁴² and is sensitive to mobile charges over nanoscale regions of the sample. The TRMC technique's utility thus varies from that of device measurement techniques. Microwave mobilities, in fact, lack significant sensitivity to grain boundaries, for example in samples of P3HT with varying regioregularity the TRMC measured $\Sigma\mu$ (sum of carrier mobilities) were indistinguishable between samples with high and low regioregularity, yet the measured μ_{FET} varies about an order of magnitude through the samples.⁴³ Therefore the extracted mobility is not directly comparable to a device mobility measurement, though both values have units of $\text{cm}^2\text{V}^{-1}\text{s}^{-1}$. Recently methods have been developed to circuitously (and laboriously) decouple the yield and mobility of the TRMC signal to obtain a microwave mobility.⁴⁴

Two main excitation sources are generally used in this technique, pulse-radiolysis and flash-photolysis, herein we solely employ the latter but the former will be briefly described. Pulse-radiolysis (PR) TRMC uses an accelerated electron source to introduce charges into the sample. Mobile charges are generated as an electron beam passes through the sample and some of the electron energy ionizes the sample. The yield of generated charges can be calculated from the radiation dose and the known electron-hole formation energy of the excited material, related to the ionization potential.⁴⁵ In solution experiments (e.g. to study isolated polymer chain), the electron beam excites the solvent containing the sample with electrons and a single carrier, electron or hole, can be selectively transferred, dependent on the energy levels and binding energy of the analyte and solvent. Similarly, samples can be measured as solid films with this technique. This method is often used to quantify the microwave mobility of a single component, for example prototypical OPV materials, PCBM or P3HT. PR-TRMC measured C_{60} and PCBM

electron carrier mobilities are used in chapter 4 to estimate charge generation yield in heterojunction samples.

The flash-photolysis technique used herein illuminates the solid or solution sample with a 4 ns wide laser pulse. Light is absorbed in one or more components of the sample and creates excitons, which subsequently dissociate to generate charges. The yield of generated charges may be known from previous studies on the materials, estimated from photoluminescence quenching experiments or estimated. Once mobile charges are present in the sample the basic principles underlying PR-TRMC and FP-TRMC are the same.

The propagation of electromagnetic waves through a uniform conducting medium, which we assume our samples to be, is described by Maxwell's equations and simplifies to two equations one each for the electric field and the magnetic field, Equations 2-1 and 2-2. The microwave frequency (the electric field) is contained in a waveguide. The waveguide shape is related to the microwave wavelength such that only one polarization of microwave can propagate in the waveguide.

$$\vec{D}(\vec{r}, t) = \epsilon_o \left(\epsilon_r - \frac{i\sigma}{\omega\epsilon_o} \right) \vec{E}(\vec{r}, t) \quad \text{Equation 2-1}$$

$$\vec{B}(\vec{r}, t) = \mu_o \mu_r \vec{H}(\vec{r}, t) \quad \text{Equation 2-2}$$

A metal iris, as shown in Figure 2-3, further restricts the microwave signal and limits the microwave wavelengths to only those that fit with boundary conditions inside the resonant cavity (i.e. a wave that has nodes at the iris and the front of the chamber.) The microwave cavity resonance is achieved by the placement of a copper iris inside the sample holder in the path of

the microwave waves. This allows for the entering microwaves to pass through the iris into the cavity but as the microwaves bounce off the far wall of the cavity some microwaves again propagate through the sample multiple times at certain frequencies, in the case of our typical 9.4 mm iris and cavity the resonant frequency is ~ 8.86 GHz. This value is dependent on the substrate thickness and dielectric constant. The thickness varies modestly between different quartz substrates and thus it is necessary to directly monitor the voltage at a variety of microwave frequencies in the dark. By incorporating a resonant cavity, Figure 2-1, we amplify small changes in the photogenerated signal allowing the measurement of low carrier mobility samples.

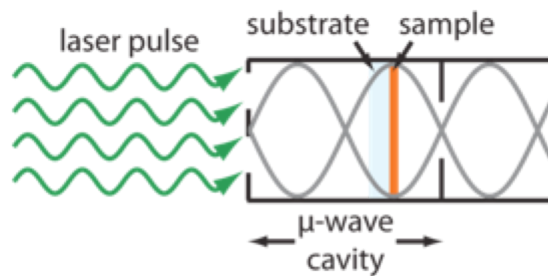


Figure 2-1. Schematic of the resonant cavity used in the time-resolved microwave conductivity technique. An iris is used to create a cavity resonance. Figure supplied by Nikos Kopidakis at NREL.

$$Q = \frac{2\pi f_o}{fwhm} \quad \text{Equation 2-3}$$

$$\tau = \frac{Q}{\pi f_o} \quad \text{Equation 2-4}$$

The resonance is fit to a Lorentzian function in which the full width half maximum, $fwhm$, and resonant frequency, f_o , are related to the quality factor, Q (dimensionless), of the cavity, Equation 2-3. The response time (rise-time) of the cavity, τ , is also proportional to the quality factor and inversely proportional to the microwave frequency, Equation 2-4. Typical

values of Q and τ are 250 and 9 ns, respectively. This value acts as a lower limit to the accurate measurement of fast charge decay properties (<10 ns.)

The power of the system is monitored as a ratio of the reflected microwave power of the photo-excited sample to the reflected power of the dark sample ($\Delta P/P$). This relates to the increase in conductivity, σ , as the sample is photoexcited (σ decays as charges lose their ability to move by being trapped or recombining) by Equation 2-1. It can further be related by the specific parameters of the sample to convert conductivity to conductance. The K-factor is calculated in Equation 2-5 by accounting for the resonance properties, where R_o is the depth of the resonance curve, and dimensional values of the sample holder, including a and b , waveguide dimensions, and d , distance between the iris and front of resonant chamber and the dielectric of the substrate, ϵ , the samples in this work are very thin in comparison to the substrate thickness and thus their dielectric contribution is small and ignored. A typical K-factor value for an organic thin film sample is 55,000. The K-factor is used to convert the power dissipation into a value of bulk photoconductance, ΔG , Equation 2-6.

$$K = \frac{2Q(1 \pm \frac{1}{\sqrt{R_o}})}{\pi f_o \epsilon \epsilon_o d \beta} \quad \text{Equation 2-5}$$

$$\frac{\Delta P}{P} = -K \Delta G \quad \text{Equation 2-6}$$

While photoconductance is a useful quantity for comparison between samples it can be further converted to the yield-mobility product using Equation 2-7. The photoconductance is normalized by the elementary charge, q_e , waveguide dimensions, β , and absorbed photon flux, $I_o F_A$ to convert it to the charge yield, ϕ , and sum of mobility, $\Sigma \mu$, product. In a generic single-

component sample the yield-mobility product is the quantity of each charge normalized by the quantity of incident photons and its respective mobility in the sample, Equation 2-8.

$$\phi(t)\Sigma\mu = \frac{\Delta G(t)}{\beta q_e I_o F_A} \quad \text{Equation 2-7}$$

$$\phi\Sigma\mu = \frac{n_e}{I_o F_A} \mu_e + \frac{n_p}{I_o F_A} \mu_p \quad \text{Equation 2-8}$$

The iris and resulting resonant cavity allow the measurement of low microwave-mobility samples and also allows for the ability to differentiate between the real microwave absorption caused by transient photo-induced mobile charges and the imaginary phase-shifting photo-induced dielectric changes. In the majority of this work we have assumed the imaginary signal contribution to be less than 5% of the total real signal and thus minimally affecting the measured signal.

2.2.2 TRMC Experimental Setup

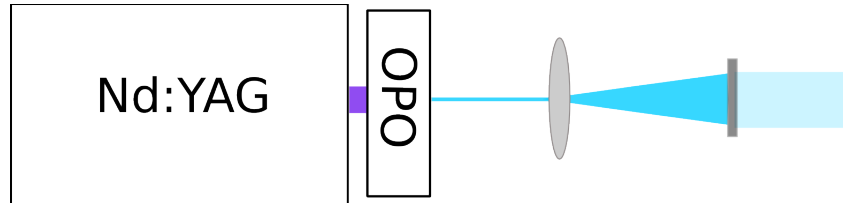


Figure 2-2. The photoexcitation setup for the TRMC is a Continuum Precision II Nd:YAG laser that uses 10 Hz 355 nm excitation pulses to pump an Continuum Panther Optimal Parametric Oscillator (OPO) to generate light pulses with wavelength range (~410-2600 nm.) The excitation beam then passes through diffusers and neutral density filters before reaching the sample cavity. A uniform, diffuse laser pulse excites the entire sample surface.

The photoexcitation of the sample in the TRMC experiment is from a wavelength-selectable Optimal Parametric Oscillator (OPO) pumped with a 10Hz, 240 mJ, 355 nm laser

pulse from a frequency-tripled Nd:YAG laser, as depicted in Figure 2-2. Experiments in this work use only visible wavelengths with the exclusion of experiments using 355 nm light in which an attenuated pump laser beam was routed around the OPO and used. Once the beam leaves the OPO it is diffused to uniformly excite the sample and passed through a series of neutral density filters to reduce the pulse energy to specified fluences, allowing the sample measurement at several different orders of magnitude of photon fluences.

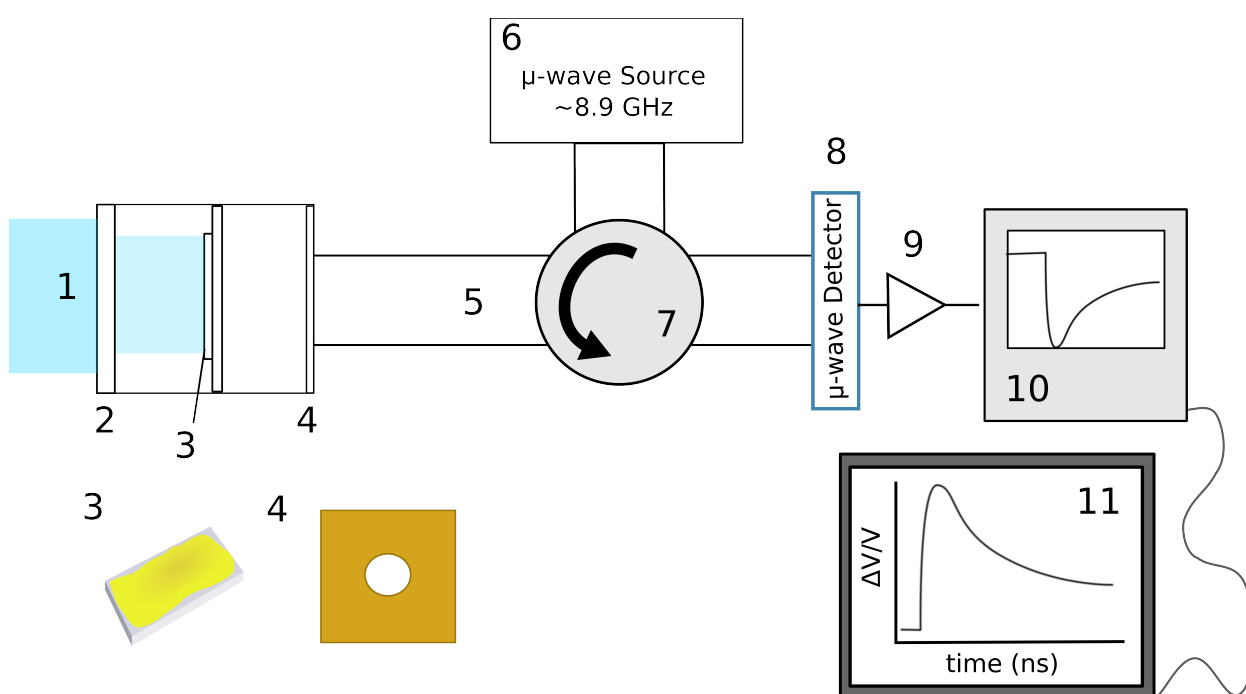


Figure 2-3. Simplified schematic drawing indicating certain important parts of the time-resolved microwave conductivity setup including 1) the diffuse laser beam 2) the microwave cavity chamber with a selectively reflective front plate which keeps microwaves inside the chamber, 3) thin-film sample on a quartz substrate, 4) iris, 5) waveguide, 6) GHz microwave source, 7) circulator, 8) microwave detector, 9) amplifier, 10) Tektronix oscilloscope, 11) computer.

As shown in the drawing of Figure 2-3, there are several key components to the TRMC experiment. The attenuated laser pulse (1) enters the sample holder and passes through a quartz window (2) containing a metal grating that selectively retain the microwaves in the resonant chamber, while allowing the incident laser pulse through. The excitation beam irradiates the

sample (3), a thin film of the particular material on a transparent quartz substrate. The sample is irradiated through the quartz to minimize photoionization. The X-band microwave is generated from a Gunn diode microwave source (6) where it enters a directional circulator (7) propagating the radiation into a waveguide (5) towards the sample holder. The sample holder contains a copper plate with the aforementioned iris (4). This leads to the sample chamber acting as a resonant chamber as described in section 2.2.1. Some of the microwave power is attenuated by the sample and the remaining microwave signal is reflected back into the circulator (7) and sent to the microwave detector (8) then to an amplifier (9) recorded using a Tektronix oscilloscope (10), which monitors the change in voltage on the detector. This signal is monitored in time, inverted and sent to Igor Pro, made by WaveMetrics, Inc., for data analysis (11).

2.2.3 Sample Measurement

A brief description of a sample measurement is included. A sample is prepared, as described in section 2.6, as a thin film on a small quartz substrate, typically by spincoating, dropcasting or vacuum deposition. This is assembled into the resonant microwave cavity either in air or a glove box. Before the measurement begins the laser power is measured and recorded at the wavelength of light to be used in the study. An automated laser power measurement system is calibrated at this time, in which a mirror moves into the path of the laser at each specified filter combination and reflects that light to an auxiliary power meter before each actual transient measurement.

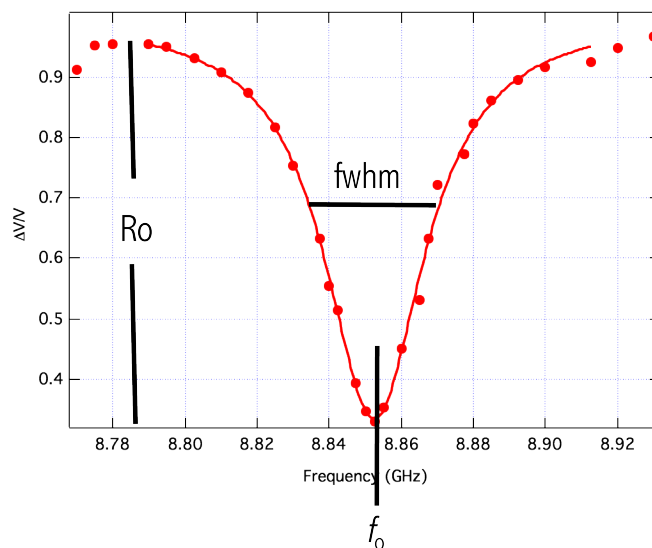


Figure 2-4. Example of the microwave cavity resonance plotting is shown. The voltage is recorded at various microwave frequencies to determine the resonance specific to the iris and sample. A Lorentzian function is fit to the resonance from which TRMC characterization parameters are determined (Q , K , τ) f_0 is the resonant frequency and R_0 the resonance depth.

The resonant microwave frequency is found by monitoring the voltage as the microwave frequency generated is changed. The minimum reflected power identifies the resonant frequency and then the microwave frequency is read and recorded. The resonant microwave cavity is recorded for a variety of frequencies to plot the resonance, Figure 2-4, and extract the accompanying cavity responses, Q , K and τ .

The oscilloscope is set to the appropriate gain and window size for the intended timescale. An acquisition program, written in Igor Pro, is used to control the experiment. Transients are averaged until the signal-to-noise ratio is deemed sufficiently low, or until additional averaging has minimal effect on the signal-to-noise ratio, typically this is anywhere from 20 - 30,000 pulse averages. The measurement is then repeated for a series of neutral density filter combinations, to measure the transient at different light intensities, thereby studying the

nonlinear effects of charge generation with light intensity. The laser power is then measured again after the final filter combination.

2.2.4 Data Analysis and Experimental Variations

Several experiments are used in this work, which vary different parameters to study a specific contribution to the signal. Most samples include an electron donor and acceptor, in which each contributes a respective mobility, thus the signal is complicated though certain experimental parameters can be used to extract meaningful information from the complicated signal. For example, the separation of the yield and mobilities can be used to quantify the mobility of one or more component. If a photo-induced electron transfer (PET) yield, ϕ , is known the sum of the localized charge carrier mobilities can be extracted. If one mobility is known the second mobility can be calculated from the sum.

If both microwave mobilities are known, the yield can easily be calculated, although this is only the case for a small number of polymers and fullerenes. Typically these mobilities are measured by pulse-radiolysis and thus may differ based on the microwave wavelength, PR-TRMC uses Q-band frequency (~ 30 GHz) whereas here X-band frequency (~ 9 GHz) is used, thus the oscillation distance minimum for microwave absorption differs slightly. In a system dominated by a single-component with a known mobility, the PET yield can also be determined. Such as in a heterojunction in which one component has a very high mobility species relative to the other, e.g. C_{60} , $\mu = 0.3 \text{ cm}^2\text{V}^{-1}\text{s}^{-1}$ and paired with an electron donating insulator, $\mu = 0 \text{ cm}^2\text{V}^{-1}\text{s}^{-1}$. It is also possible to force the system into the singly-contributing mobility regime by using very low weight percent loadings of the second component, such that the second component does not cluster, this is the so-called “dilute regime”. An example of the usefulness of the dilute

regime was demonstrated in work by Coffey et al.⁴ In the work reported in this thesis, I study systems that both fit in the singly contributing mobility and dilute regime as well as complex systems in which all components are contributing to the total signal.

2.2.5 Thin-Film Absorption Measurements

Absorption measurements were taken on a Shimadzu UV-3600 UV-VIS-NIR Spectrophotometer with an external ISR-3100 Integrating Sphere Attachment, Figure 2-5.

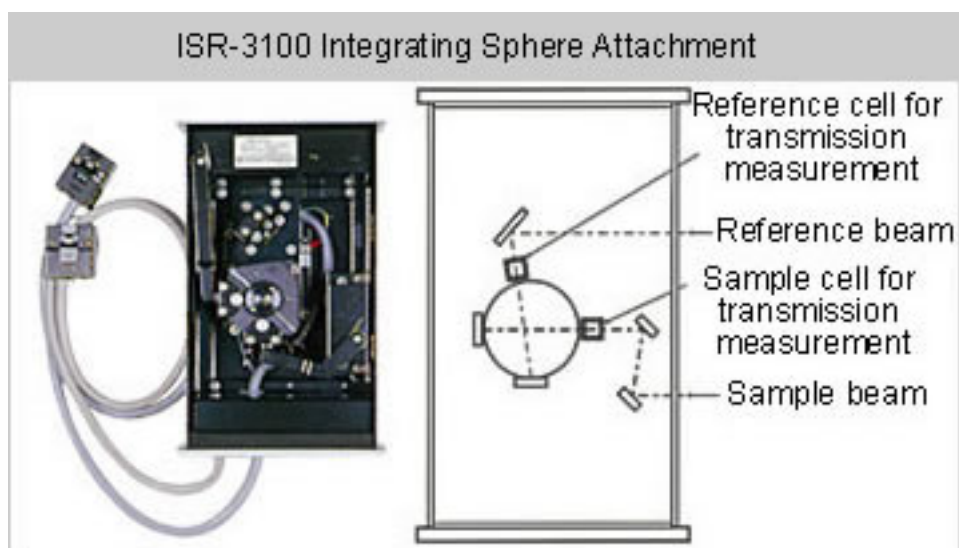


Figure 2-5. Picture and simple diagram of the Shimadzu integrating sphere, as provided on the Shimadzu website. Transmission and reflectance measurements are both made using this setup.

As described above an accurate value of light absorbed by the sample, F_A , is necessary for TRMC data analysis. Samples have varying degrees of reflectivity dependent on the incident wavelength, the sample's composition, and its crystallinity. Separating absorption from reflection can be accounted for by measuring the transmittance (T) and reflectance (R) of the sample in an integrating sphere. The absorptance, A , is then calculated from Equation 2-9.

$$A = 100 - T - R$$

Equation 2-9

Light transmission (and absorbance accordingly) is not a property that scales linearly with film thickness but instead it is related to the number of molecules through a logarithm. Absorbance is useful for determining the fraction of absorbed light. But for comparison of different optical transitions between films absorption is the preferred metric. Thin film absorption can also be used to help elucidate the intermolecular structure of films. Specifically if the first excited state is split by an H- or J- aggregation and the wavelength is blue and red shifted respectively. This will be of particular importance in chapter 6.

2.3 Photoluminescence

Photoluminescence (PL) is the emission of a photon from a photoinduced excited-state. PL measurements were made with a Horiba Jobin Yvon Fluorolog-1039 with continuous wavelength Xenon excitation source, 300 lines/mm gratings blazed at 500 nm, and with a charge-coupled device (CCD) detector on a Horiba iHR320 Imaging Spectrometer. Entrance and exit slit widths of 5 nm were used.

Emission can be used to study the electronic and vibrational states in a molecule. Singlet emission is primarily studied herein but non-radiative kinetics also contributes to photoluminescence techniques, affecting both the photoluminescence lifetime, τ_R , and quantum yield, ϕ .

2.3.1 Steady-State Solution Photoluminescence

Samples were measured in dilute solutions, typically 2 μM , toluene, chloroform, and dichlorobenzene solutions. The excitation wavelength is chosen such that it is blue shifted significantly with regard to the emission. If a sample has a low quantum yield then long pass

filters may be required to further suppress the excitation light. Different monochromator gratings are selected to choose the wavelength window of detection and resolution. The sample detector is located in the conventional manner perpendicular to the excitation beam for solutions.

2.3.2 Relative Quantum Yields

Relative quantum yields, ϕ_R , were also measured in this work. Solutions of the compounds being studied are compared to a dye, chosen for its similarity in absorption and emission spectra. The sample and standard solutions were made to be nearly the same optical density (OD) at the excitation wavelength. The excitation beam intensity was also monitored to account for intensity fluctuations in the source. Measurements between the sample and standard were taken with the same integration time, slit widths and grating settings.

Though sample and standard were measured in rapid sequence some variation is observed in the incident beam, thus the PL is normalized to the intensity of the incident beam. The total photoluminescence area is integrated for both the sample, F , and standard, F_{ref} .

The relative quantum yield is calculated using Equation 2-10. The ratio of integrated photoluminescence, F , of the sample is taken with respect to the reference, normalized by the absorptance, while accounting for the refractive index of the solvents, n . Absorptance is used instead of absorbance due to its linear relationship with excitation intensity (whereas absorbance is nonlinear). The yield is finally adjusted in the case that the reference has a less-than unity yield, ϕ .⁴⁶

$$\Phi_{sample} = \Phi_{ref} \frac{F(1 - \exp(-A_{ref} \ln 10)n^2)}{F_{ref}(1 - \exp(-A \ln 10)n_{ref}^2)} \quad \text{Equation 2-10}$$

2.3.3 Solid-State Film Photoluminescence

Thin film PL was measured using the same spectrometer, but using a front-face illumination instead. Identical parameters were used, though longer integration times were required and occasionally a spike of noise, attributed to cosmic radiation, had to be removed from the spectrum (identified by a giant signal over a single point or two – statistical methods were used to determine artifacts from real signals.)

2.3.4 Photoluminescence Quenching

Photoluminescence (PL) quenching was also studied in films of electron donors and acceptors to gauge electron transfer. Several mechanisms can lead to the loss of photoluminescence signal. As indicated in the kinetic scheme in Figure 2-6, there are many possible pathways for a molecule once in the excited state, D^* . The excited state can decay as fluorescence, k_r , or nonradiatively decay to D through internal conversion, k_{nr} . In the presence of another molecule, $[A]$, a charge transfer state is possible, CT, which can also radiantly or nonradiatively decay, k_r and k_{nr} . Another state, the charge-separated state, CS, is possible and depicts the pathway through which charge separate in a donor-acceptor system. All pathways besides the emission from D^* act as a photoluminescence quencher.

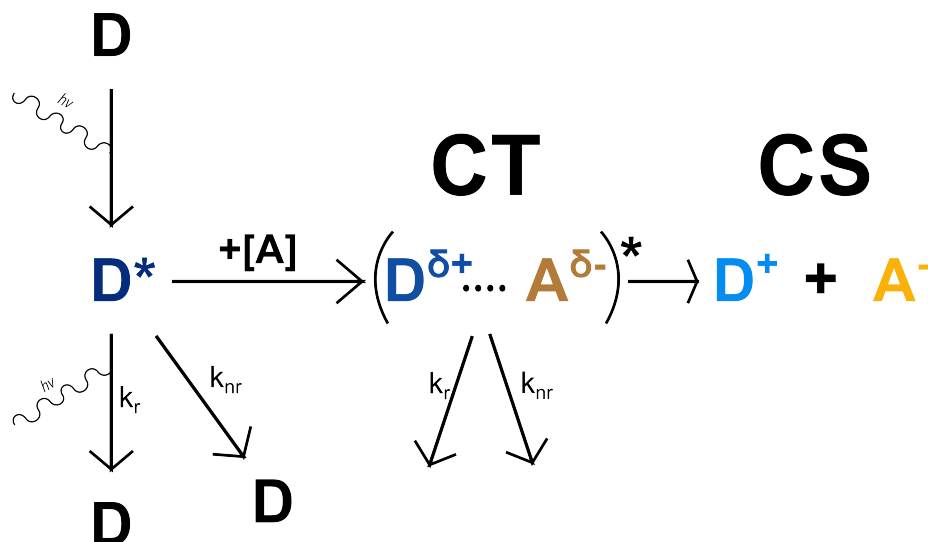


Figure 2-6. Simple kinetic scheme indicating the relaxation pathways an excited species, D^* , can take. D^* can return to D through radiative relaxation, k_r , as fluorescence or undergo nonradiative relaxation, k_{nr} . In the presence of an electron acceptor species, A , D^* may now also couple to form a charge transfer state with A , CT , in which the pair are electronically coupled. The CT state can also decay through radiative and nonradiative relaxation leading to isolated and uncoupled D and A species. Or the CT state can fully separate to the D^+ and A^- ions in the charge separated state (CS). It is the latter process that leads to charge generation in a heterojunction. All processes aside from fluorescence from D^* are sources of photoluminescence quenching.

2.3.5 Time-Correlated Single Photon Counting (TCSPC)

Transient photoluminescence experiments are used to measure excited-state lifetimes. A sample is photoexcited and the resulting photoluminescence is monitored as a function of time. The method used in this work is time-correlated single photon counting, as shown in Figure 2-7. In the TCSPC technique a Fianium Supercontinuum laser pulse, at a repetition rate of 10 MHz, is passed through an acousto-optic tunable filter (AOTF) to select the excitation wavelength and is then directed to the sample. The emission from the sample is directed to a monochromator, to select for a specific emission wavelength, and then into the detector. The signals are recorded with the Becker & Hickl SPC-130 TCSPC module.

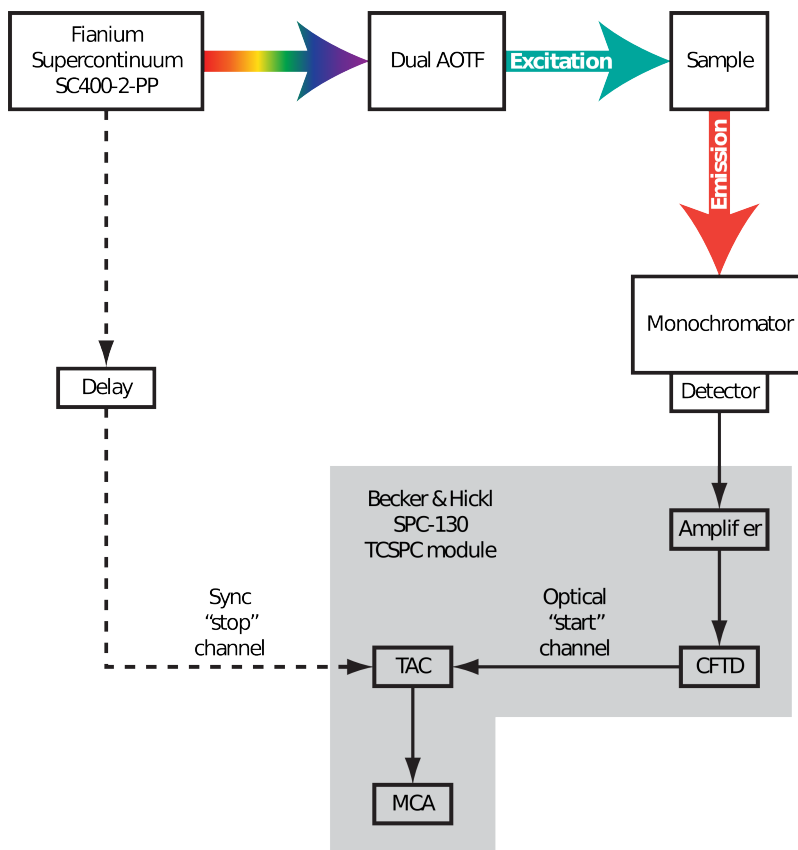


Figure 2-7. Time-correlated single photon counting schematic, courtesy of Andrew Ferguson at the National Renewable Energy Laboratory. In the TCSPC technique a Fianium Supercontinuum laser pulse, at a repetition rate of 10 MHz, is passed through an AOTF to select the excitation wavelength and is then directed to the sample. The emission from the sample is directed to a monochromator, to select for a specific emission wavelength, and then into the detector. The signals are recorded with the Becker & Hickl SPC-130 TCSPC module.

Samples are measured in a $1 \times 1/2 \text{ cm}^2$ cuvette. The excitation beam is chosen and a 10nm bandpass filter is placed in its path to constrain the excitation to only chosen wavelengths. An instrument response function (IRF) is determined by scattering light from a colloidal scattering solution of SiO_2 nanocrystals to the detector. Neutral density filters can be used to minimize noise. The transient signal is fit to a single or multiexponential decay convoluted with the instrument response, Equation 2-11. The lifetime of the fits are then used as photoluminescence lifetime, τ .

$$I_{PL}(t) = IRF \otimes Ae^{-\frac{t}{\tau}} \quad \text{Equation 2-11}$$

2.3 Powder X-ray Diffraction on Thin Films

X-ray diffraction, XRD, is a highly versatile and useful technique frequently used to study both liquid crystal phases and OPV active layers. In this work, it is used to determine the thin film structure of different samples, both as neat samples and as mixtures. Helical nanofilaments have a distinctive diffraction pattern and in chapter 3 XRD is used to identify that phase in different sample preparation methods and processing conditions. The experiment is also used to determine the layer spacing of the novel smectic liquid crystal mesogens studied in chapter 6.

2.3.1 Experimental Parameters

Diffraction measurements were taken on a Rigaku d/max diffractometer, with Copper $K\alpha$ radiation from a rotating anode set to 40 kV and 250 mA. 5mm entrance slits were used to focus the beam directly onto the substrate surface. $\theta/2\theta$ measurements were taken at a rate of 0.5°/minute. The diffractogram background was fit to a double-exponential decay and removed and the diffraction peaks fit to Gaussian curves. Instrument broadening was measured from Gaussian fit diffraction peak from LaB_6 . The instrument broadening FWHM was determined to be 0.082° and was corrected with equation 2-12.

$$B_{sample} = \sqrt{B^2 - B_{instrument}^2} \quad \text{Equation 2-12}$$

2.3.2 Basics of Diffraction

Diffraction experiments rely on the interaction between a propagating electromagnetic field and a material in its path. In particular, diffraction is most strongly expressed from objects with a size on the same order of magnitude as the radiation's wavelength. X-rays are used in the characterization of atomic and molecular materials because of their interaction with electrons. Electron density surrounding nuclei absorb the X-ray radiation, and reemit X-rays elastically (at the same wavelength as the incident X-ray beam.) The emitted radiation can be described as wavefronts. Periodic structuring of electron density (of atoms and molecules) leads to constructive interferences of the wavefronts at an angle relative to the incoming X-ray angle.

In the organic-based samples presented in this thesis, the X-ray diffraction occurs between the repeating electron-dense aromatic regions of the smectic layers. Intra-layer crystallization leads to diffraction and considerable information about a sample but is not included in this work, largely due to the interference of the quartz substrate at such diffraction angles. Low 2θ angles, below 1° , are limited by the orientation of the detector, which can become saturated with x-ray radiation at low angles (directed from the source to the detector.)

2.3.3 Peak Position, Width and Analysis

The diffraction angle is related to the reciprocal spacing of the lattice. In all samples characterized herein layer spacing is due to smectic liquid crystalline ordering. These distances are on the order of several nms, which simplified diffraction analysis. Peak width can be used as a gauge of crystallite domain size in poly- and semicrystalline samples. The limited correlation length across the diffractable region leads to peak broadening. Peak widths are also affected by strain within the crystal. Though often both factors contribute to the peak broadening, sample

composition and preparation may lead one broadening factor to dominate. In all cases in this work the crystallite size is the dominant contribution to peak broadening.

2.4 Transmission Electron Microscopy (TEM)

TEM is used to topographically map the P-9-OPIMB samples, images were taken by Dong Chen in the LCMRC. Small samples were cut from different parts of the prepared quartz substrate sample and coated with 2 nm Pt at an angle of 45°, creating a shadowed replica of the samples surface. A 25 nm layer of carbon was then deposited as a support to the Pt replica. The sample was dissolved in ethyl acetate and the replica floated and mounted on a Formvar-supported Cu TEM grid. The TEM images were taken with a Phillips TEM. The angled deposition leads to a surface differentiation where dark areas are surfaces that face the deposition and light areas are shadowed from the deposition. Samples were measured to be between 100-350 nm thick as measure with a Tencor Instruments Alpha-step profilometer.

2.5 Differential Scanning Calorimetry (DSC)

Phase transitions of various materials were determined with a Mettler Toledo DSC823e using a heating and cooling rate of 10° C/min. Bulk mixed samples were made by combining accurately weighed portions of the mixture components into a glass vial, which then underwent three cycles that included melting on a hotplate combined with manual stirring with a small glass rod, and then placing the vial into a centrifuge and spinning at 4000 rpm for 2 min. The samples were then measured from these mixtures and weighed into aluminum crucibles (2-4 mg of material). Thin film samples were made as described below and then scraped from their substrate onto a weigh dish, crucibles were then filled with sample flakes. The second heating cycle data is reported for all bulk samples and the first heating cycle data is reported for thin film samples.

2.6 Thin-film Sample Preparation

Quartz substrates were prepared by repeated sonication in a solution of Hellmanex III, then acetone, and finally isopropyl alcohol and then were rapidly dried with compressed air. The substrates were cleaned the day before or the day of sample deposition.

P-9-OPIMB was synthesized as previously described⁴⁷, and was thoroughly purified by recrystallization. Purity was confirmed with ¹H and ¹³C NMR spectra recorded on a Bruker Avance-III 300 spectrometer. Sample phases were confirmed with DSC and polarized light microscopy. C₆₀, PC60BM, PC70BM and bis-PC60BM were purchased from Nano-C Inc. n,2-OBTTT molecules were synthesized by Mike Springer in the LCMRC.

Stock solutions of P-9-OPIMB and fullerenes were made in chloroform at concentrations of 10 g/L. Mixtures were made from relative volumes of stock solutions. Samples of n,2-OBTTT were made as molar ratios from freshly prepared solutions in a N₂ filled glovebox (unless otherwise noted.) Films were prepared by spin-coating solutions with a PWM32 spincoater onto clean quartz substrates at 600 rpm for 60 s in a nitrogen-filled glove box and then annealed on a pre-heated hotplate for 5 min and then rapidly cooled by immediate placement from the hotplate to a room temperature metal surface. Bilayer films were made by depositing 30 nm of C₆₀ with an Edwards thermal evaporator onto prepared P-9-OPIMB films. P-9-OPIMB samples were stored in the dark and measured in air. n,2-OBTTT samples were stored in the dark in a N₂-filled glovebox and measured in N₂ (except for XRD experiments.)

Chapter III: Helical Nanofilament Thin Films

3.1 Introduction to HNFs

The helical nanofilament (HNF) liquid crystal phase represents a promising self-assembling, nanophase-segregated architecture with potential as a good charge transporting system in an organic photovoltaic (OPV) device. A key advantage of the HNF phase over other bulk heterojunctions is the spontaneous formation of rigid twisted rods with nm metrics in two dimensions, and liquid crystalline control of morphology (vide infra). As illustrated in Figure 3-1, molecules of HNF mesogens (in this case P-9-OPIMB, Figure 3-1A) self-assemble into twisted layers composed of aromatic and aliphatic sublayers, Figure 3-1B.²⁵ These sublayers create domains that are conducting (aromatic sublayer) and insulating (aliphatic sublayers.)

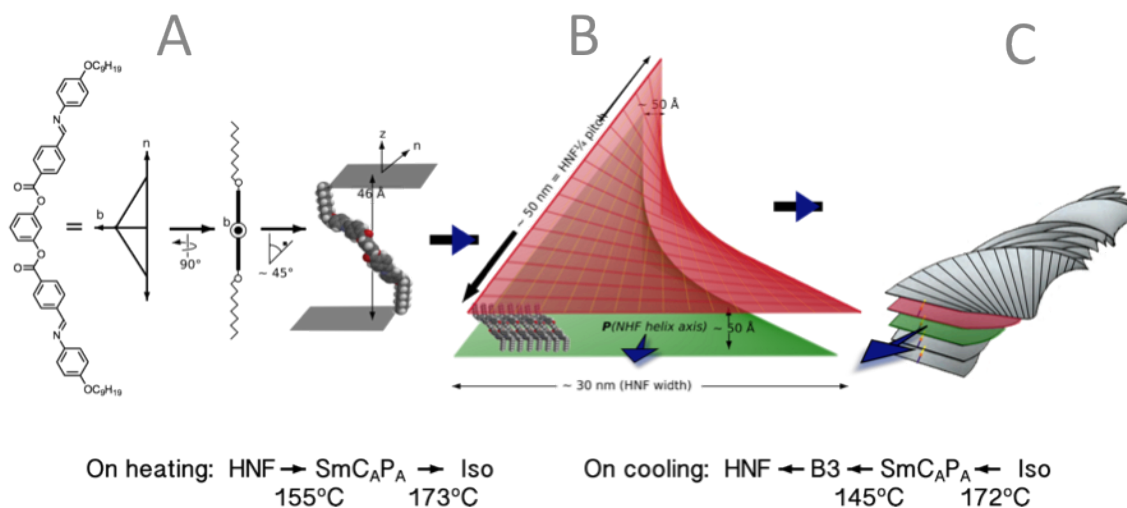


Figure 3-1. Hierarchical self-assembly of an HNF mesogen: A) The molecular structure of the HNF mesogen P-9-OPIMB with the transition temperatures and phase sequence observed on heating and cooling; B) Illustration of the structure of a single twisted layer composed of HNF mesogens; C) Stacking of the twisted layers produces “twisted rod”-shaped HNFs ~ 30 nm in diameter. The final stage of the self-assembly (not shown) involves liquid crystalline ordering of

the HNFs into an hexatic phase where the HNF twist is coherent. The HNF bulk phase is necessarily porous, since twisted rods as illustrated in C cannot fill space.

Within the aromatic sublayers, dynamic solid-state NMR data suggests the molecules are present in a “crystalline” environment, and electron diffraction experiments have revealed that the aromatic sublayers actually exist as crystalline “half-layers” in a rectangular lattice, with the “stretched” direction in aromatic half-layers oriented in nearly orthogonal directions.^{25, 30} Since the molecules in these half-layers are covalently bonded, the orthogonality of the rectangular lattices induces strain, which is relieved by negative Gaussian curvature of the layers, leading to a twisted layer structure as illustrated in Figure 3-1B. The degree of curvature in the twisted layers cannot be uniform, and approaches zero as the layer width increases and as the number of layers in the stack (HNF thickness) increases.^{25, 28} This causes the width and thickness of the HNFs to spontaneously self-limit (~ 30 nm width, and ~ 5-8 layers per HNF) (Figure 3-1C). Thus, the twisted layers exist in stacks, with a small number of layers (5-8) in each stack, forming twisted HNFs (Figure 3-1C). The HNF length is unconstrained, and at the highest level of the hierarchical structure, the HNFs form a hexatic liquid crystalline supra-HNF self assembly wherein the HNFs are parallel, and the twist is coherent (Figure 3-2).²⁸ The HNF have polar symmetry, with the polar axis (shown in blue in Figures 3-1B,C), and electric polarization, oriented along the HNF long axis.

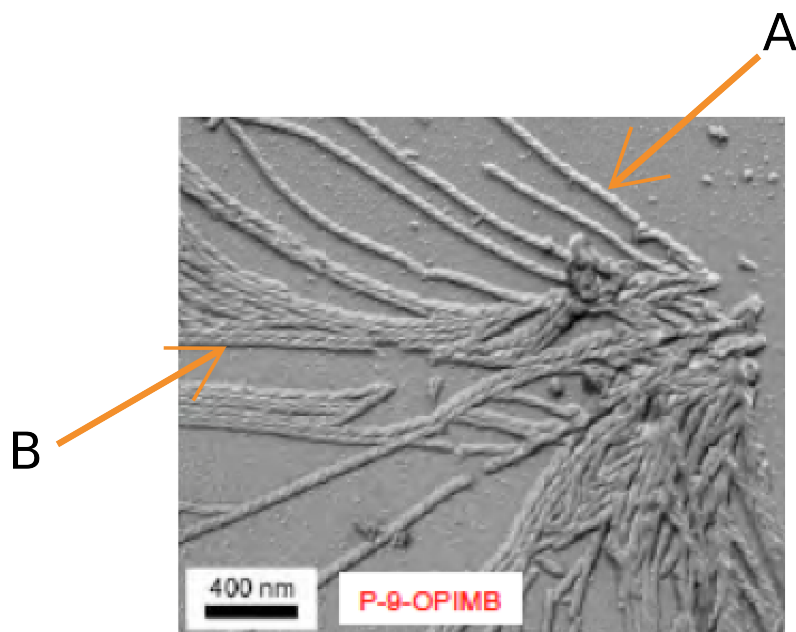


Figure 3-2. Freeze-fracture of P-9-OPIMB grown from 8CB, demonstrating the individual helical nanofilaments (A) as well as their ability to align and coherent twist growth (B). Image from Chen et al.²⁸

The HNF phase is necessarily porous, and is robust to high levels of doping by small molecules, mesogens, and even polymers.^{28, 48, 49} Diffraction and freeze-fracture TEM studies by the Clark group show that the dopant molecules surround, but do not penetrate, individual nanofilaments, shown in Figure 3-2. This leads to a novel two-component composite with periodic nano-segregated domains of each component. It has been demonstrated that P-9-OPIMB forms HNFs when mixed with the soluble fullerene PC₆₀BM, though analysis was limited to bulk mixtures.⁴⁸

While detailed characterization of the bulk HNF phase has been previously reported,²⁵ understanding the structure of very thin films of HNF phase, < 300 nm, particularly in mixtures with other materials, is critical with regard to its application in OPV. Herein, we report studies of neat thin films of the HNF mesogen P-9-OPIMB, bilayers with C₆₀, and as mixtures with soluble fullerenes when processed under different conditions.

The HNF phase can be grown with macroscopic orientation of the long axis of the rods through various methods, including thermal gradient, applied electric fields, shearing, growth from nematic liquid crystal solvents, geometrical confinement, and self-assembled monolayers.^{26, 28, 50, 51} One such experiment achieved HNF alignment through apparent shear induced by air flow over the top of a micro-confined sample during cooling, illustrated in Figure 3-3, the HNFs grew in the direction of the channel.⁵⁰ With regards to OPV, macroscopic alignment would be beneficial for the structuring of a device with the HNFs perpendicular to the substrate allowing for direct pathways for charge carriers through the film to the electrodes.

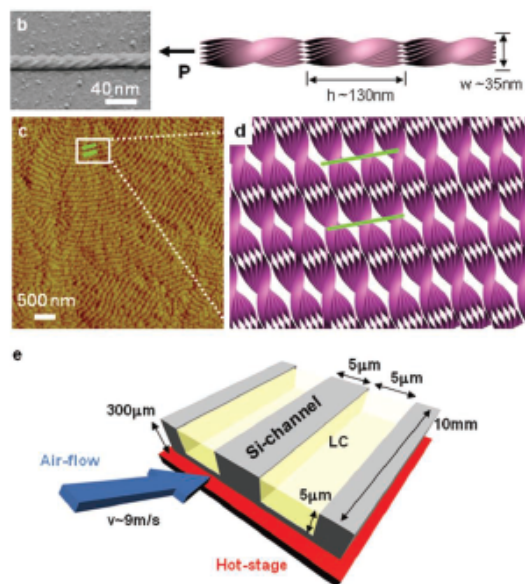


Figure 3-3. HNF's aligned with an induced temperature gradient. Hot samples are capillary filled into 10 μm channels of a Si substrate and exposed to a steady flow of gas as it cools. The HNFs align along the channels of the substrate. Image from Yoon et al.⁵⁰ Such methods could be employed to align HNFs in a photovoltaic device, thereby creating a direct charge transfer pathway between electrodes.

Several mesogens have been found to form HNFs.^{29, 52} Today, with only a few exceptions, all of the known HNF-forming mesogens contain a benzylideneaniline moiety. The nature of the HNF mesogen “structure space” has not been adequately explored, and it is

conceivable that HNF-forming mesogens with various conjugated aromatic systems will be found. This allows for the design of mesogens with favorable optical and electrochemical properties to capitalize on the advantageous HNF structural properties.

Previous work on HNFs using the freeze-fracture transmission electron microscopy (FFTEM) technique demonstrate that bulk HNF phase at a glass interface exhibit toric and parabolic focal conic surface structures as shown in Figure 3-4.⁵³ These surface structures occurred in a bulk sample and are revealed when the fracture takes place close to a substrate surface. These results illustrate the transition of the liquid crystal ordering between the glass substrate surface and the bulk HNFs. The present study focuses on characterizing very thin films at an air interface formed directly by spin-casting P-9-OPIMB from chloroform solution, as well as bulk and planar heterojunctions formed by these films. Strong surface effects are introduced in these samples by the large surface-to-volume ratio of the spin-cast thin films.

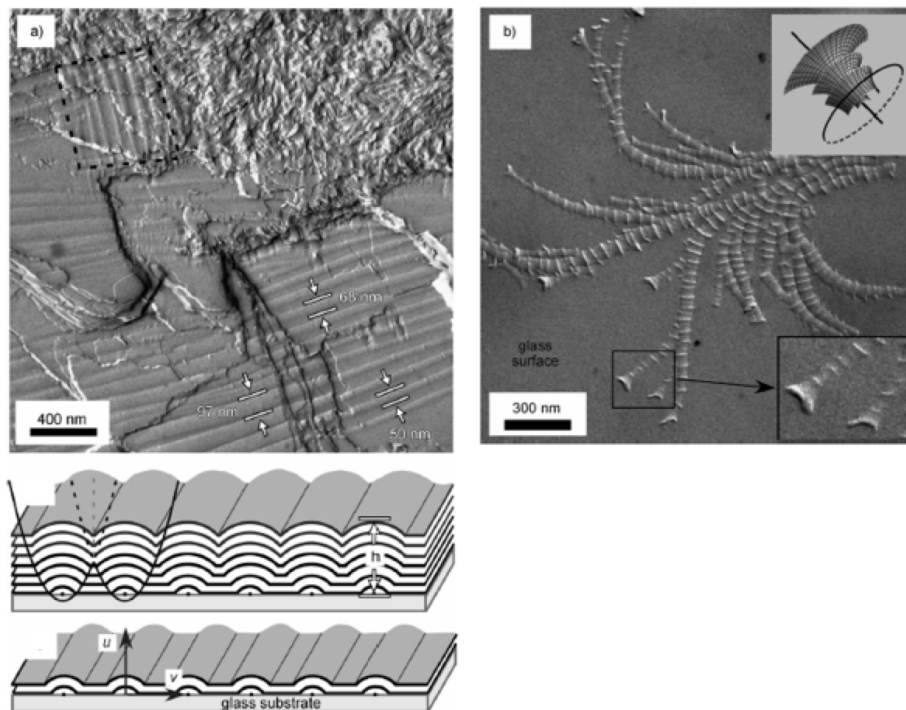


Figure 3-4. a) At a glass surface, parabolic focal conics are common. In these surface-induced structures the twist is suppressed, and layers with positive curvature are seen. The curved smectic layers of P-9-OPIMB stack from a point defect. In this study by Chen et al. HNFs were observed to grow on top of the focal conics. Image from Chen et al.⁵³ b) Toroidal focal conics, with negative curvature, are another commonly seen surface-induced structure obtained from films of P-9-OPIMB obtained by freeze-fracture.

One of the most ubiquitous techniques for liquid crystal characterization is polarized light microscopy (PLM.) However, the use of PLM in this work was limited by the characteristic low birefringence of the HNF phase²⁵ combined with the sample thinness leading to films that regardless of phase appeared isotropic under the microscope.

TEM is therefore the key technique employed to image the surface of the spin-cast thin films and thus identify the liquid crystalline structuring, similar to its use in previous bulk studies of this HNF phase. Representative images from across the sample were taken and thus provide information on how the microstructure changes across the substrate.

The largely topographical data from TEM is complemented with XRD, which probes liquid crystalline ordering throughout the sample and gives insight into the layered structuring of the sample. Additionally, in this work XRD is utilized to define the diffraction correlation lengths, which are then be used to determine whether the HNF phase, where the layering is necessarily short range, is formed in the sample.

Lastly, to characterize the sample microstructure differential scanning calorimetry (DSC) was employed on bulk and thin film samples. DSC quantifies the microstructure effects on phase transition temperatures and transition enthalpies. Together these techniques provide information on order and microstructure in films of neat P-9-OPIMB as well as for the fullerene-containing two-component samples.

3.2 Transmission Electron Microscopy (TEM)

Topographical images of liquid crystalline films are useful in determining the phase. In the case of these films, TEM is used to compare the effects of processing on the microstructure.

3.2.1 TEM of neat P-9-OPIMB films

Thin films of as-cast and annealed P-9-OPIMB are characterized with TEM to compare the well-studied bulk P-9-OPIMB microstructure with that of the thin films. Figure 3-5 shows the difference between as-cast and annealed films of P-9-OPIMB. In Figure 3-5A neat films of as-spun P-9-OPIMB present characteristics of the HNF phase, similar to the HNFs shown in Figure 3-2. Specifically the repeating, twisted texture seen in Figure 3-5A has previously been identified as characteristic of the HNF phase.^{25, 28, 53}

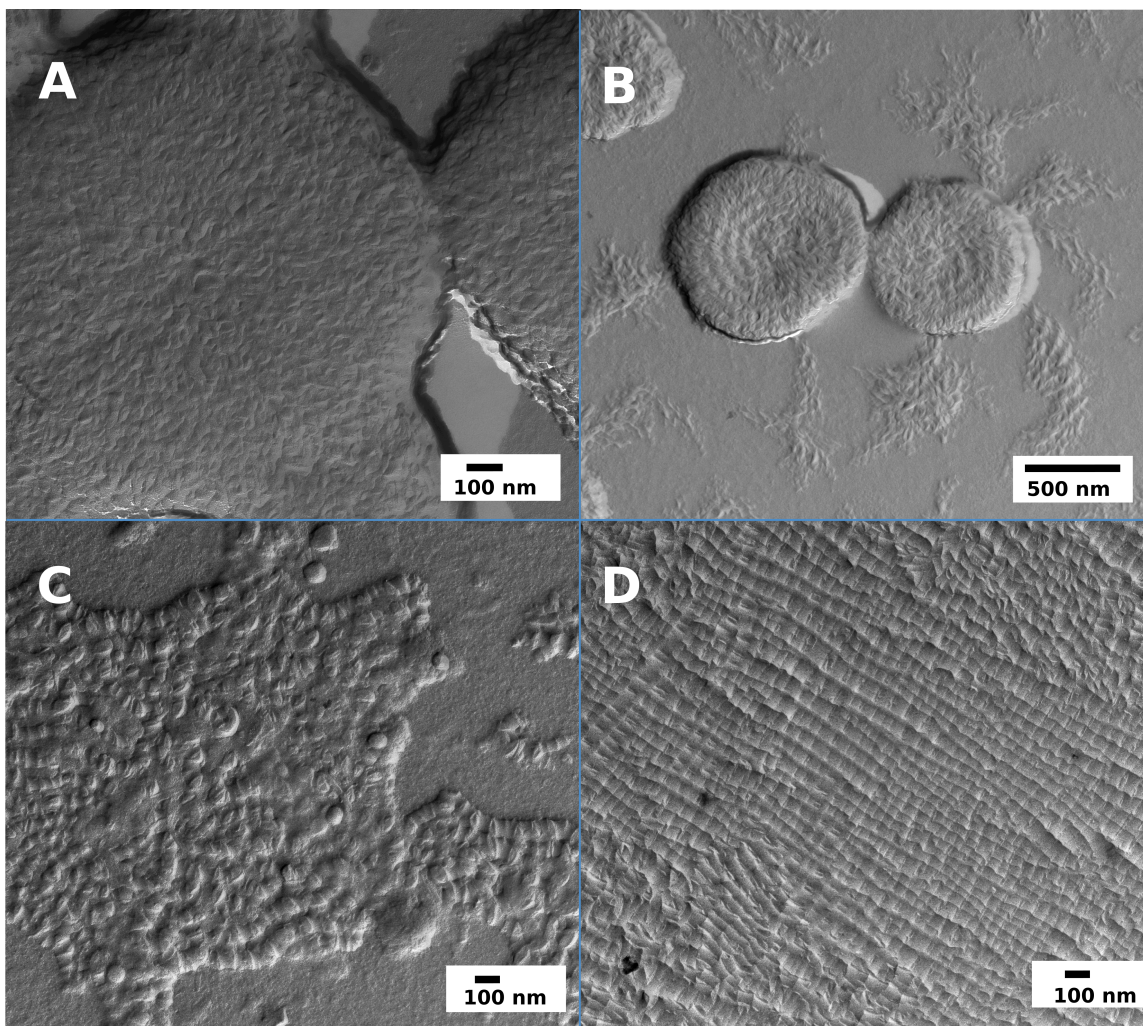


Figure 3-5. TEM images of as-spun and annealed P-9-OPIMB thin-films on quartz are presented. Images (A) and (B) are as-cast P-9-OPIMB films. Images (C) and (D) are annealed thin films. The texture of these images reveals surface topography obtained for a thin layer of Pt metal obtained by oblique incidence evaporation onto a cryo-cooled surface. The topography of the resulting Pt surface is essentially a replica of the organic thin film topography. HNFs are observed in the as-cast samples, in addition to the surface droplets. When annealed the films form surface-driven phases such as those shown in Figure 3-4. This differentiates between kinetic (as-cast) and thermodynamically (annealed) formed films.

Figure 3-5B shows HNF droplets on the substrate surface. This is a common feature in the as-spun films, where the concentric circles in the droplets match the width of the HNF's. The

HNF's appear to nucleate and grow from the center outwards, often with a single HNF droplet, the chirality is maintained.

The annealed samples (Figure 3-5C, D) contain several surface structures, predominately made up of the focal conics with a small amount of HNFs. This is similar to the structures found at a glass interface from a broken planchet sample in work by Chen et al. as described above.⁵³ The droplets seen in the as-spun sample are also observed, but to a significantly smaller extent. The droplets merge upon annealing and no longer contain the orientation of the as-spun samples.

Thus, spin-coating from a high vapor pressure solvent (chloroform) causes a macroscopically uneven surface, yet a well-ordered HNF texture is seen across most of the sample. Typically a thick film of P-9-OPIMB becomes better oriented and more regular upon annealing, yet this is not the case in the spin-cast thin films. Thin annealed films of P-9-OPIMB form thermodynamically favored surface-driven microstructures, namely the parabolic focal conics shown in Figure 3-5C and 3-5D.

3.2.2 TEM of P-9-OPIMB/PC60BM thin films

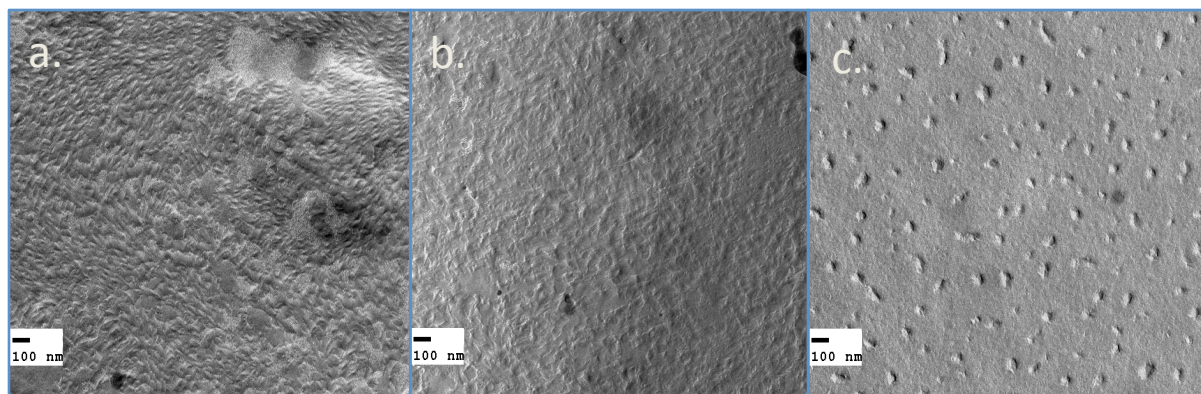


Figure 3-6. Thin films of P-9-OPIMB/PC₆₀BM composites made 50 wt%. Samples were annealed to different temperatures (A) 25 °C, (B) 150 °C and (C) 240 °C. In as-spun films HNFs

are the dominant phase while the two annealed samples show varying degrees of lamellar phase, in which the mesogen tails are oriented normal to the air interface.

Figure 3-6 shows similar TEM images to above containing 50% by weight PC₆₀BM in P-9-OPIMB. Surface structures were measured for composites processed under 3 different conditions, 1) as-spun, 2) annealed to 240 °C, above the clearing point of P-9-OPIMB 3) annealed to 150°C, above the glass transition temperature but below the transition to the smectic B2 phase (see Figure 3-1A for the phase sequence and transition temperatures of neat P-9-OPIMB).

Similar to the behavior of neat P-9-OPIMB as-spun films, as-spun mixtures of P-9-OPIMB and PC₆₀BM, Figure 3-6a, exhibit predominantly HNF textures. Several surface textures, like those in the annealed neat P-9-OPIMB films, are present in the films, though only in a small portion of the sample, as displayed below in Figure 3-7. Mixed P-9-OPIMB/PC₆₀BM films show more variation across the surface than the neat P-9-OPIMB films, and the mixed films do not contain the well-ordered droplets found with neat P-9-OPIMB samples. The composite samples include some larger droplets, but none similar to the symmetric, well-defined droplets in the neat as-spun samples. Despite the high levels of doping (50%_{wt} PC₆₀BM) the as-cast composite films form the HNF phase.

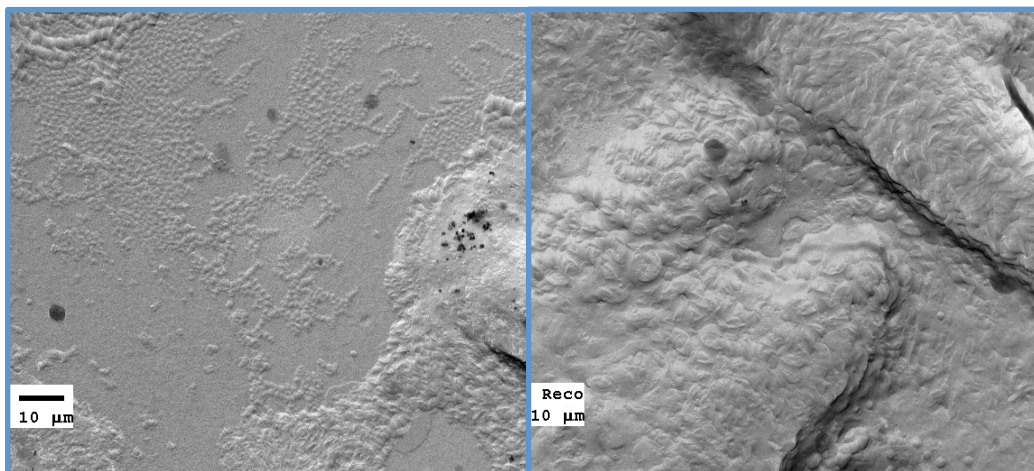


Figure 3-7. TEM images of 50/50 PCBM/P-9-OPIMB as-spun samples demonstrate parabolic focal conics, arising from concentric curved smectic layers.

Figure 3-6C shows imaging of a composite film annealed above the P-9-OPIMB clearing point. The texture is consistent with a flat lamellar structure, where the surface apparently completely expels curvature in some domains of the sample. While the as-cast film varies between HNF and other textures (with only a small portion of the area showing this lamellar texture), the entire annealed composite sample is lamellar.

One unusual feature of the annealed films is the presence of the ~ 50 nm protrusions from the lamellar surface. Similar features were seen in the bulk P-9-OPIMB-PC₆₀BM mixtures by Chen et al. and identified as pockets of PC₆₀BM crystallites.⁴⁸ Here we observe the fullerene, apparently expelled from the lamellar liquid crystal, forming aggregates at the air-liquid crystal interface.

Images from sample 3, annealed to 150 °C, are exemplified in Figure 3-6B. These films are best described by considering a transition between the HNF phases seen in the as-prepared sample and the lamellar microstructure of the sample annealed above the clearing-point. This

demonstrates that the clusters of PCBM have not formed or are not yet at a detectable level for the imaging technique.

From the TEM data it can be concluded that the as-cast films, both neat and composite, form the HNF phase upon rapid evaporation from the solvent. One-to-one by weight levels of doping (a molar ratio of approximately 1.128:1 P-9-OPIMB: PCBM) with a soluble fullerene present HNF phase formation, further demonstrating the robustness of the phase. With the composite films, annealing causes a transition to a surface-driven lamellar structure in which a large un-quantified amount of PC₆₀BM has migrated to the surface of the films, forming relatively large PCBM aggregates.

3.3 XRD of Thin-Film Samples

Diffraction experiments are used to compare the as-cast and annealed films imaged in the previous section. XRD is able to probe microstructure spacing and also correlation lengths.

3.3.1 XRD of Neat P-9-OPIMB

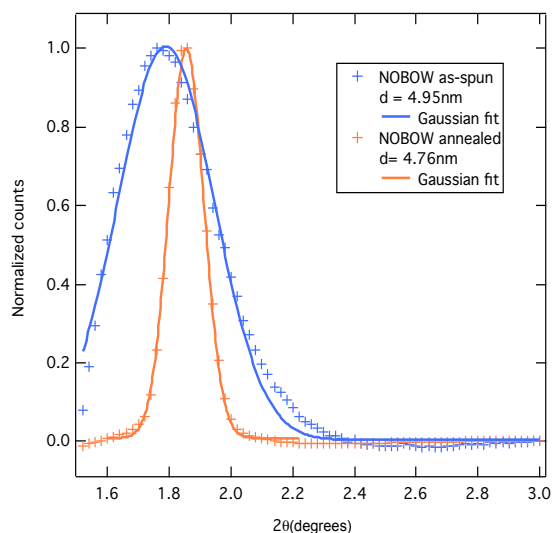


Figure 3-8. Diffractograms of as-spun and annealed (to 165 °C) NOBOW (P-9-OPIMB) thin films showing Bragg scattering from the layers are shown, along with their Gaussian fits. d is the smectic layer spacing. XRD of as-spun film, shown above by TEM to be composed of HNFs, demonstrates a broader diffraction peak than the annealed film, this indicates a shorter correlation length. Only in the annealed P-9-OPIMB sample was a higher order diffraction peak detected

Figure 3-8 shows X-ray diffractograms of as-spun and annealed P-9-OPIMB thin films, identically prepared to those characterized by TEM. In both the as-cast and annealed samples, diffraction occurs at approximately $2\theta = 1.8^\circ$. The diffraction peak of the annealed sample is considerably sharper than that of the as-cast peak. The annealed sample also presents a second-order diffraction peak of $0.05\times$ the peak height of the fundamental Bragg diffraction. Higher order peaks are more sensitive to the short-range disorder, in the as-cast film, the short-range disorder is greater, and thus no second-order peak is distinguishable

Helical nanofilaments have been previously characterized by XRD, with the primary identifying characteristic being the broad interlayer peak, arising from diffraction from the smectic layers near $2\theta = 1.8^\circ$, and multiple intralayer peaks, arising from intermolecular

diffraction within the smectic layers, near $2\theta = 21^\circ$.²⁵ The quartz substrates lead to a significant background between $10 - 25^\circ$, obscuring intralayer diffraction as well as PC₆₀BM crystallization peaks.⁵⁴

The Gaussian-fit full-width at half maximum (fwhm) is used to compare the correlation length of the smectic layers between samples. The correlation length increases as the number of continuously correlated smectic layers increase as described in chapter 2. The correlation length is inversely related to the peak widths. Thus, the HNF phase, where the number of correlated layers is limited to 5-8 layers due to the curvature-induced HNF formation, exhibits a broad peak, while annealing increases the correlation length of the layers leading to a sharper peak. The smectic layer spacing of the HNFs and lamellar layers can be calculated from the Bragg diffraction angle as described by Equation 3-1.

$$d(\text{\AA}) = \frac{\lambda}{2 \sin\left(\frac{2\theta_{\text{rad}}}{2}\right)} \quad \text{Equation 3-1}$$

The two samples (as-spun and annealed) show very similar layer spacing, calculated from the 2θ diffraction peak, indicating that the smectic layer spacing is largely unchanged for annealed samples. However, the peak width varies greatly between as-spun and annealed samples, as observed in Figure 3-8. Here, the fwhm is used to compare the as-spun and annealed peak widths. The peaks were fit to Gaussian functions and corrected from the instrument peak broadening as shown in Equation 3-2, where B is the measured fwhm, $B_{\text{instrument}}$ is the fwhm of the LaB₆ sample and B_{sample} is the corrected peak broadening from crystallite size. Sufficiently sharp diffraction peaks (as sharp as the instrument limited standard, LaB₆) are referred to as instrument response limited.

$$B_{sample} = \sqrt{B^2 - B_{instrument}^2} \quad \text{Equation 3-2}$$

Instrument related peak broadening was measured using the standard, LaB₆, measured with identical experimental parameters as the sample measurement. A full-width half max (fwhm) was determined for each Gaussian-fit diffraction peak between 2θ of 20° and 100° and then linearly extrapolated to the low values of 2θ corresponding to the P-9-OPIMB layer diffraction. An instrument-limited fwhm of 0.082° was determined. The Scherrer equation is often used in inorganic samples to determine correlation length values from diffraction peak widths, while it is not appropriate for use with the organic molecules measured herein, it is used to give a relative length scale to the instrument limited diffraction from the inorganic LaB₆ standard. The Scherrer equation, Equation 3-3, is calculated with a K-factor of 0.9, and an X-ray wavelength (λ) of 1.54 Å. To determine the peak resolution at the smectic layer diffraction peak a value of 2θ = 1.85° was used.^{55, 56}

$$S = \frac{K\lambda}{FWHM_{rad} \cos\left(\frac{2\theta_{rad}}{2}\right)} \quad \text{Equation 3-3}$$

Thus if a sample exhibited a peak width at half max of 0.082°, this would infer a correlation length of 96.9 nm. Any longer correlation length would not lead to a sharper diffraction peak and the correlation length cannot be accurately calculated. Therefore, above that value any peak with a fwhm of 0.08° was determined to have a correlation length of >95 nm and was called instrument resolution limited (IRL).

A limited number of layers, typically between five and eight, are present in a single nanofilament formed by P-9-OPIMB. The as-spun sample, determined by TEM to consist of

HNFs, diffracts with a fwhm of 0.200° . In the annealed sample the diffraction fwhm is instrument resolution limited, thus corresponding to a longer correlation length of over 95 nm as previously described. HNFs have a set correlation length due to the limited smectic layer width and thickness, but a lamellar smectic phase is not similarly constrained. The sharper fwhm of the annealed sample indicates a longer correlation of smectic layers than would typically be found from the five to eight layer nanofilament. XRD evidence complements the thin film TEM images to confirm that the surface structures are forming HNF versus lamellar/surface phases, making films easily distinguishable by the relatively less difficult XRD technique.

3.3.2 XRD of P-9-OPIMB with Fullerene Dopants

	As-cast		Annealed	
PC₆₀BM dopant	fwhm	d(nm)	fwhm	d(nm)
25% P-9-OPIMB	0.276	4.68	0.129	5.27
50% P-9-OPIMB	0.304	4.66	0.098	4.93
75% P-9-OPIMB	0.242	4.83	0 (RL)	4.62
100% P-9-OPIMB	0.200	4.94	0 (RL)	4.76
50% P-9-OPIMB	fwhm	d(nm)	fwhm	d(nm)
PC ₇₀ BM	0.455	4.64	0.182	4.87
Bis-PC ₆₀ BM	0.236	4.86	0 (RL)	4.71

Table 3-1. Comparison of as-cast and annealed samples with varying concentrations of soluble fullerenes. Fwhm correlation length is given along with the smectic layer spacing, d, for each sample. RL refers to an instrument resolution limited peak width. In each sample annealing led to a sharpening of the peak width.

The methodology is extended to other soluble fullerene and P-9-OPIMB samples, where fwhm and d are shown in Table 3-1. Samples include different wt% mixtures of PC₆₀BM and P-9-OPIMB in addition to 50% mixtures with two other common soluble fullerenes, bis-PC₆₀BM

and PC₇₀BM. Analogous to the neat P-9-OPIMB study above, in all cases here the annealed sample peak is measurably sharper than the as-spun (HNF) samples thus following the trend: annealing results in an HNF-to-lamellar transition in thin spin-cast films.

Across the samples of increasing PC₆₀BM loading the peak width of the annealed sample decreases. The as-spun films do not show a significant correlation between the amount of fullerene doping and lamellar layer correlation length. Since lamellar smectic layers typically prefer orienting parallel to an air interface, the layer correlation length would be expected to be the same as the film thickness, consistent with the observed measurements.

The smectic layer spacing does not consistently change as a result of the annealing certain samples show an increase in layer spacing whereas others show a decrease. The average change in peak spacing for the as-spun to annealed transition is 2.9 Å. This supports the hypothesis that the smectic layers and intermolecular structure of the B4 phase remain nearly the same in the HNF-to-lamellar transition during annealing, and that the HNF layers simply flatten to form smooth lamellar textures with more layers than are possible in the HNFs, without dramatically changing the internal structure of the layers, Figure 3-9.

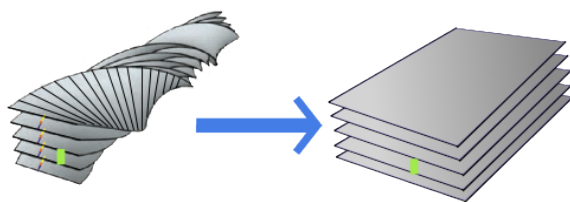


Figure 3-9. Schematic of HNF and lamellar packing illustrating the same layer spacing (green bar) a property measured with diffraction experiments.

XRD substantiates the TEM results that the as-spun P-9-OPIMB films form HNFs but upon annealing the mixed films change to either a lamellar or surface-driven microstructure

dependent on whether the sample is neat mesogen or a fullerene composite, respectively. These “flattened” HNFs are strained due to the deformation from the preferred negative Gaussian curvature of the HNF layers, but interaction with a flat surface and the air interface, and the fullerene clustering, apparently pays the energy cost of this strain.

3.4 Differential Scanning Calorimetry

DSC is used to accurately measure the phase transitions of the neat liquid crystal and multi-component mixtures of P-9-OPIMB and PCBM.

3.4.1 Mixed P-9-OPIMB/PCBM Differential Scanning Calorimetry

The final technique applied to characterize the heterojunction phases is differential scanning calorimetry (DSC). This technique is widely utilized in both the liquid crystal and organic photovoltaic fields. In DSC, a controlled amount of heat is added to the sample while monitoring the temperature change. A nonlinear correlation between heat and temperature occurs during a phase change, such as between liquid crystal transitions or an organic crystal melting. DSC has been widely used to characterize the B4 phase, including that of P-9-OPIMB.

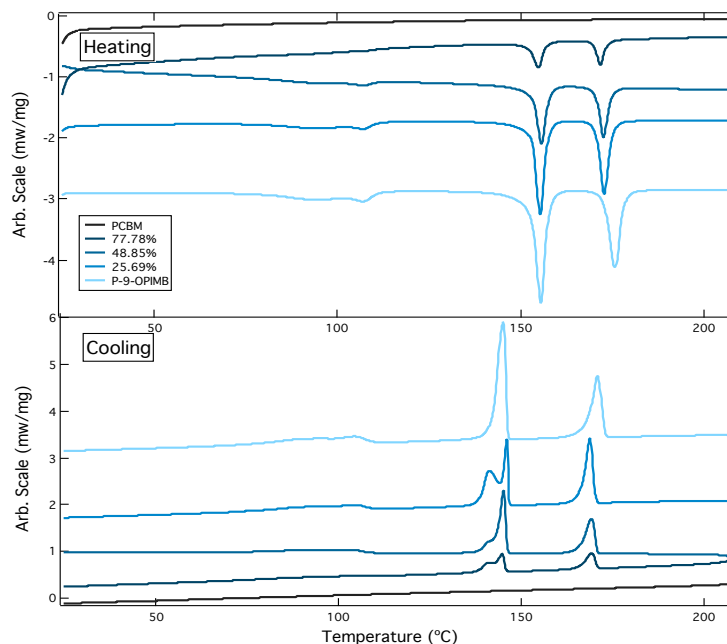


Figure 3-10. Heating and cooling DSC curves of blends of PCBM and P-9-OPIMB are shown. All curves are the second heating and cooling cycle. On heating the HNF to B2 transition is nearly unchanged across the blend series, whereas the Isotropic transition is sensitive to PCBM doping. On cooling the phase transitions are nearly identical.

The DSC curves for bulk P-9-OPIMB have several distinguishable transitions, as shown in Figure 3-9. Upon heating from 25°C a phase transition is observed around 100°C. At this temperature, it is proposed that the alkyl tails of the P-9-OPIMB molecules melt from a glassy state but that the HNFs remain intact. A sharp HNF to B2 transition occurs at 150°C. The B2 phase clears to isotropic at 172°C. These transitions, in addition to a monotropic B3 phase between HNF and B2, are present in the DSC curve on cooling. Both B2 and B3 are Smectic phases that are extensively described elsewhere, the B2 phase has been identified as $SmC_A P_A$. C_A refers to anticlinic smectic C, in which the director tilt alternates from layer to layer, and, C_S refers to synclinic smectic C, in which the director tilt is uniform from layer to layer.⁵⁷ The layer polarization, P_F and P_A , indicate Ferroelectric and Antiferroelectric layer, respectively. The Ferroelectricity originates from the polar (C_2) symmetry of the layer structure, and the

polarization is parallel to the layers. If the polarization parallel from layer to layer the phase is Ferroelectric, while if the polarization alternates sign from layer to layer, in the case of B2 the phase is Antiferroelectric. Thus the B2 phase consists of tilted Smectic C layers, which form chiral layers with both symmetric polarization and alternating polarization.

As mentioned in the sections on TEM and XRD, this study encompasses the mixing of P-9-OPIMB with soluble fullerenes, in particular PCBM. It is relevant to note that over the temperature range of 25-200°C no phase changes were observed for neat PCBM samples. This is consistent with previous work on PCBM over that temperature range. Though a residual solvent peak was seen in the first DSC curve of PCBM at 240°C, thermo-gravimetric analysis of PCBM has shown the melting temperature for PCBM crystallites is near 280°C.⁵⁸ In the annealed samples used in this work, temperatures never exceed the melting point of PCBM.

Figure 3-10 demonstrates that the HNF to B2 phase transition (155°C) remains nearly static throughout the mixing profiles, ranging from 0 to 100% PCBM, indicating that the HNF structure and melting transition remains constant in the mixtures. This is also observed in the subtle glass transition at 100°C. Interestingly, the B2 to isotropic transition is the only phase change significantly affected by the doping. A DSC curve of a neat PCBM sample is also shown and verifies the lack of phase changes in PCBM in the liquid crystalline window of P-9-OPIMB.

Sample	χ_{PCBM}	$T_1(^{\circ}\text{C})$	$\Delta H_1(\text{J/mg})$	$T_2(^{\circ}\text{C})$	$\Delta H_2(\text{J/mg})$	$T_3(^{\circ}\text{C})$
1	0	107	6.81	155.5	4.34	175.67
2	0.235	107	4.86	155.33	2.49	172.83
3	0.459	107	3.23	155.67	1.69	172.67
4	0.757	106.17	1.50	154.83	0.79	171.67
5	1	---	---	---	---	---

Table 3-2. Enthalpies and temperatures of transition for various molar mixing ratios of PCBM and P-9-OPIMB.

Table 3-2 includes the enthalpy changes for the various phase transitions that the mixtures go through. Additionally the enthalpy changes of the phase transitions are plotted against the PCBM loading in Figure 3-11. The enthalpy changes map the PCBM molar ratio, which indicates that the enthalpies of each phase change are solely originating from the P-9-OPIMB and that they are experiencing a phase transition identical to the corresponding transitions in bulk samples. Both phase change enthalpies fit linearly with the ratio of PCBM to P-9-OPIMB with an x-intercept near 100% PCBM.

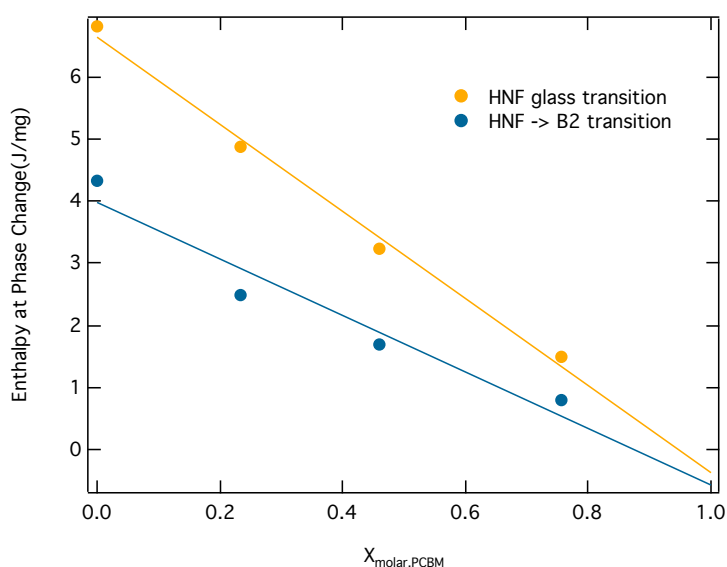


Figure 3-11. Enthalpy of phase transitions plotted against molar ratio of PCBM in P-9-OPIMB. The slopes of both enthalpies come close to crossing zero at 100% PCBM.

3.4.2 Calorimetry of P-9-OPIMB Thin Films

Figure 3-12 shows DSC curves of neat P-9-OPIMB processed as thin films. Thin films of the liquid crystal mixture were prepared as before on quartz substrates and annealed to 170°C. Samples were then scraped from the substrate into a DSC aluminum crucible. Surface effects are destroyed after a single heating (the sample is now just flakes in a crucible) thus the first heating

cycle is the most relevant to thin film-dependent structure, though in the aforementioned bulk DSC 2nd heating curves are studied.

As can be seen in the DSC curves of Figure 3-12 the glass transition of the as-spun (HNF) film is slightly shifted to a higher temperature in comparison to both the bulk P-9-OPIMB and annealed lamellar thin film sample. The phase transition temperatures and enthalpies are summarized in Table 3. The glass transition of P-9-OPIMB is largely a melting of the mesogen tails and thus the tails exist in a more stable state as part of the HNFs in the thin film. This is further confirmed by the larger change in enthalpy of the transition, as seen in Table 3-3. The 155°C phase transition remains generally unchanged in either film (as-spun or annealed). Since the tails have already melted in all samples this is indicative of the intermolecular (HNF/lamellar to SmC_{AP}A) phase change. The enthalpy change for this transition is nearly identical in the two thin film samples. If we assume that the end state of the transition, the SmC_{AP}A phase, has the same enthalpy then we can assume the same starting enthalpy. Thus the enthalpy of the intermolecular interactions in both low temperature states is similar.

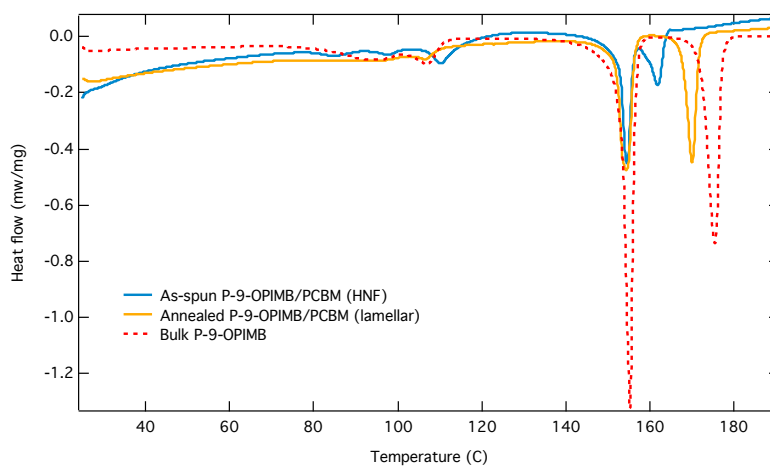


Figure 3-12. Thin films of annealed and as-cast P-9-OPIMB/PCBM films and bulk P-9-OPIMB.

Sample	Phase	T _G	ΔH(kJ/mol)	T _{G-B2}	ΔH	T _{B2-I}	ΔH
As-spun	HNF	110.17	24.7	154.5	54.7	161.83	65.3
Annealed	lamellar	106.5	14.6	154.25	56.0	170.0	97.1
Bulk	HNF	107.0	16.3	155.5	64.9	175.67	99.2

Table 3-3. Temperatures of phase transitions in thin films of PCBM/P-9-OPIMB as compared to bulk P-9-OPIMB. The glass and isotropic transitions are significantly affected in the thin films, though the B2 transition is almost unchanged in all samples.

Remarkably, in all mixing profiles (except neat PCBM) of the bulk P-9-OPIMB/PCBM samples the HNF phase behaved the same. Additionally the DSC curves of bulk mixtures made at varying concentrations of PCBM further confirm the existence of the HNFs as part of a mixture.

Finally, The formation of B4 on subsequent heating cycles demonstrates that the PCBM and P-9-OPIMB are not reacting when annealed. This is significant in the following chapter which studies charge transfer variances in different microstructures.

3.5 Conclusion

We characterized thin films of P-9-OPIMB and found that spin-casting films leads to the formation of HNFs but that the films transition to curved surface-driven smectic phases upon annealing. The microstructure is also dependent on the presence of a fullerene dopant. Soluble fullerenes trigger the formation of a lamellar P-9-OPIMB phase in which the fullerene macro-phase separates as clusters on the surface of the liquid crystal. The extent to which the PCBM clusters penetrate into the P-9-OPIMB layer is unknown.

It is of particular interest to note that the fullerene dopants, even at a modest 25 wt% doping, significantly impacted the thin film microstructure of the PCBM. This particular observation is important to the vast array of potential mixing that occurs in small molecule and polymer heterojunctions. The semiconducting polymer is often discussed as the primary driving

Chapter IV: Charge Transfer in the Helical Nanofilament System

4.1 Introduction to HNFs as a Donor-Acceptor Heterojunction

Organic photovoltaics rely on an optimization of both the active layer energetic profiles and morphological mixing. Herein the effects of the donor-acceptor microstructure (morphology) are studied, particularly regarding implications for photo-induced charge generation in OPV. P-9-OPIMB and PCBM were identified to form unique microstructures in chapter 3, here they are explored and compared as charge transfer surfaces.

A brief overview of charge generation in OPV follows to emphasize the motivation for studying HNFs as an ordered heterojunction. Efficient photovoltaics depend on the absorption, which typically requires hundreds of nanometer thick layers of the electron donor and acceptor materials, known as the active layer. Once an exciton is generated in the active layer it migrates to a donor-acceptor interface. Excitons, unaffected by electric fields, move through energy-transfer processes between adjacent molecules, resulting in mostly direction-less exciton diffusion. The exciton diffusion length, d_L , is dependent on the lifetime of the excited state, the rate of energy transfer between molecules, and the presence of lower energy trap states.^{2, 22, 23} The exciton diffusion length is largely related to the energetics of the specific molecule as well as its microstructure. In the prototypical electron-donating polymer, P3HT, d_L is commonly reported at 10-15 nm. Ordered systems have been shown to increase the d_L over an analogous amorphous structuring,²³ such as a highly ordered rubrene triplet-state exciton shown to diffuse distances up to microns.²² Donor-acceptor material mixing is often used to counterbalance a

short exciton diffusion length thus increasing the likelihood of an exciton will approach the donor-acceptor interface. The materials must be mixed on the order of exciton diffusion length.²

Photo-induced electron transfer (PET) is also microstructure-dependent. The relative donor and acceptor energetics largely dictate the rate of photo-induced charge generation as described in chapter 1. Recent work by Coffey et al. has further demonstrated that charge transfer in organic photovoltaics follow the Marcus theory rate of electron transfer, as shown in Equation 4-1.⁴ ΔG° is the Gibb's energy offset between the initial and final energies of the electron before and after PET and λ the reorganization energy of the system, which acts as a charge transfer activation barrier.

$$k_{PET} = A_{PET} e^{-\frac{(\Delta G^{\circ} + \lambda)^2}{4\lambda RT}} \quad \text{Equation 4-1}$$

Once generated, the electron and hole must move away from interface to an electrode. The ability for a charge to move through a material is its charge carrier mobility. A small molecule in two different crystalline packing configurations may exhibit dissimilar carrier transport properties. Other studies have included the comparison of charge carrier mobility in different small molecule liquid crystal phases.^{31, 32, 59} Highly ordered crystalline phases tend towards better transport properties. Intermolecular spacing and orientation allow for sufficient HOMO and LUMO orbital overlap, leading to hole and electron mobility respectively.⁶⁰

Finally, the charges must be able to move to an electrode. Many novel and highly structured heterojunctions have been proposed, in effort to create a direct charge pathway between the D-A interface, where charges are generated, and the electrodes, where they are

extracted from the device. These range from self-assembling systems to templated heterojunctions.^{33, 60-63}

The optimized active layer microstructure is commonly achieved through a blended composite of the donor and acceptor entities, and is referred to as the bulk heterojunction (a bilayer structuring of the same materials is a homojunction.)^{1, 2} Following the identification of two energetically suitable materials, most often a conducting polymer and a soluble fullerene, the materials are mixed at various wt% ratios, in different solvents, with thermal and/or solvent-vapor annealing in order to create the optimum device.^{64, 65}

Often only the conditions of the best device are reported, with the accompanying solved microstructure. This haphazard process is repeated as new active layer materials are developed. And where one scheme of solvents, temperatures and processing may work well for P3HT it may not have the same effect on a new polymer or small molecule system. In this work a self-assembling heterojunction with precise control over microstructure is presented.

HNFs present a potential solution to the necessary blended microstructure characteristics identified above. The self-assembling formation of nano-scale aggregates with well-defined structure makes HNFs a promising active layer component. The HNFs behave essentially as organic nanorods with diameter ~ 25 -30 nm, approximately twice typical exciton diffusion lengths found for many conjugated polymers.⁶⁶ In addition, the smectic layers of the HNFs are crystalline,³⁰ which has been correlated with enhanced carrier mobility and exciton diffusion in small molecule systems. The nanofilaments are alignable^{26, 50, 51} and have the potential to orient perpendicular between the electrodes, allowing direct charge transport to the electrodes for

extraction. The alignability and diffusion length mixing of HNFs would allow for thicker active layers.

In comparison to other self-assembling small molecule systems the HNFs have a particular advantage in that half of the surface area of the nanofilament is composed of layer edges, which allow for contact between the P-9-OPIMB molecule and the electron acceptor. We postulate that the large contact area between electron acceptors and electron donors will lead to HNFs acting as an effective PET microstructure. These properties of HNFs suggest suitability for incorporation in excitonic photovoltaics, this is the first work exploring this phase for use in donor-acceptor heterojunctions.

It should be noted, however, that P-9-OPIMB is not an ideal material for OPV in most respects. The material represents a model for studying the effects of the heterojunction microstructure on photo-induced charge transfer. Specifically, the minimally-conjugated benzilideneaniline arms of P-9-OPIMB lead to a maximum absorption at 360nm. Design of small bandgap mesogens based on HNF-forming mesogens will be necessary for their use in OPV devices. What's more, while HNFs have properties that may be advantageous in charge extraction, such as orientational alignment, this study is focused on morphological effects on photoinduced charge transfer.

Several different techniques are applied to gauge the effectiveness of HNFs as a PET interface. This work builds on the microstructure work of chapter 3 in which two unique microstructures are identified. In all cases the two blended morphologies being compared contain the same components, and only differ in film processing, thereby reducing energetic differences

between the samples so that the differences in photoinduced electron transfer between microstructures is in fact due to the microstructure environment.

4.2 Solid-State Spectroscopy

The films are characterized with optical absorption and photoluminescence spectroscopy, photoluminescence quenching, and time-resolved microwave conductivity. The solid-state absorption of the P-9-OPIMB films are studied as films. Previous studies of P-9-OPIMB films showed a significant blue shift in the absorption,⁶⁷ which was attributed to an H-aggregate effect. The photoluminescence (PL) of films of P-9-OPIMB and PCBM are measured. PL quenching is used to confirm that P-9-OPIMB is able to quench the PCBM excited state.

The electrodeless time-resolved microwave conductivity (TRMC) technique, described in chapter 2, is used to probe the formation of mobile carriers in the heterojunction system indicating photoinduced electron transfer in a donor-acceptor system. Herein, photoconductivity is measured in P-9-OPIMB/C60 bilayers and blends of P-9-OPIMB and PCBM, specifically in the heterojunction microstructures described in chapter 3. Various experiments on temperature, lifetime and excitation wavelength are also included.

4.2.1 Thin-film Optical Absorption of P-9-OPIMB and Blends

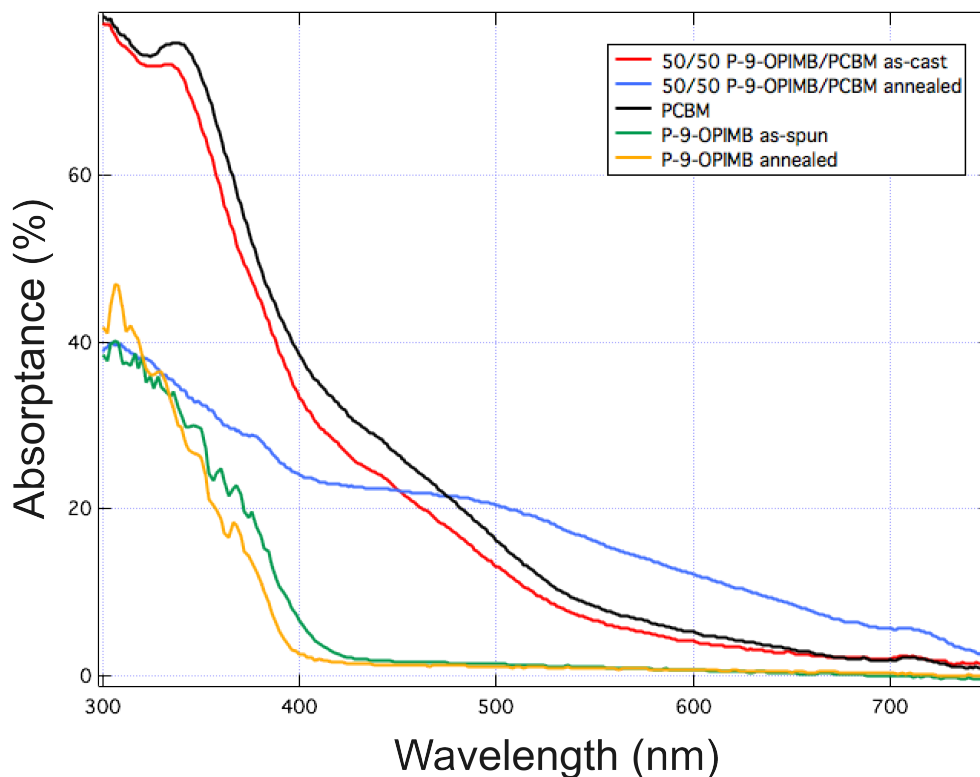


Figure 4-1. Thin film absorbance of P-9-OPIMB, PCBM and mixtures as measured in an integrating sphere. Annealed P-9-OPIMB/PCBM thin films show a distinct broad absorption at 500 nm.

Figure 4-1 shows the scattering and reflection corrected absorbance of different thin films on quartz. P-9-OPIMB absorbance varies minimally between as-cast and annealed films, though it is distinctly blue-shifted from the solution absorption of the monomer. The lack of absorption change between the films is evidence that the in-layer packing is similar between the microstructures; also hypothesized from the calorimetry results in chapter 3. It has previously been shown that P-9-OPIMB molecules in the HNF phase form an H-aggregate.⁶⁷ Absorption of mixed films are also shown in Figure 4-1, 50/50 as-spun samples have a very similar absorption

to neat PCBM while the annealed film has a reduced peak at 340 nm and a broad shoulder at 500 nm. The 50/50 films were otherwise identically prepared and should be similar thicknesses.

Previous studies by Cook et al. identified a charge-transfer absorption in films of neat PCBM at 500 nm.⁶⁸ This charge-transfer peak is present in lamellar (annealed) films of P-9-OPIMB/PCBM and is less pronounced in both the neat PCBM film and the as-cast sample. Additionally, the CT shoulder in the lamellar sample is slightly redshifted relative to that in the neat PCBM sample. A wavelength shift could be because the CT is formed between P-9-OPIMB and PCBM not solely PCBM molecules.

4.2.2 P-9-OPIMB Thin-film Photoluminescence

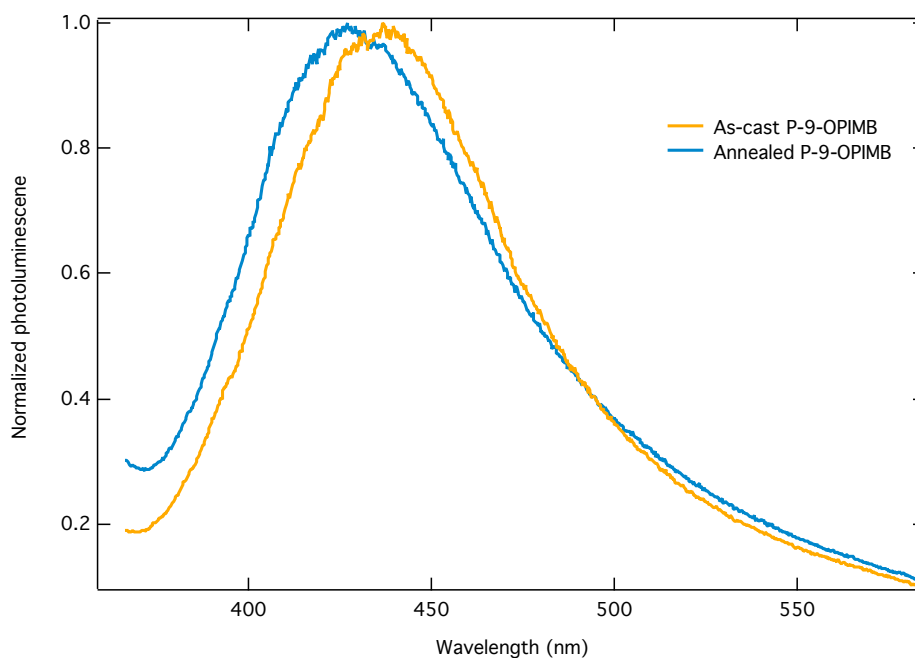


Figure 4-2. Solid-state photoluminescence of P-9-OPIMB films shows an emission peak at 440 nm. Slight differences are observed between the as-cast (orange) and annealed (blue) samples.

As-cast and annealed film photoluminescence is shown in Figure 4-2. Film thickness varies between the samples and thus the normalized emission is shown. The annealed sample

emits at a slightly higher energy than the as-cast sample. Both samples exhibit low photoluminescence intensity and the Stokes shift, as determined from the peak absorbance and fluorescence, is about 600 meV. A large Stokes shift and low emissivity is common to H-aggregate films.

4.2.3 PCBM Photoluminescence and Quenching with HNFs

Though excited-state quenching can be employed to study a variety of charge transfer and energy transfer phenomena, in the following section TRMC experiments show that these heterojunction films undergo photoinduced electron transfer (PET) and thus we attribute the PL quenching here to be associated with PET. Quenched excitations from photo-induced electron transfer is widely used to study efficiency of charge transfer, as it signifies that excitons are able to diffuse to the interface where they are quenched. Here we are using PL quenching to compare the PET in 50/50 P-9-OPIMB/PCBM films prepared to three different temperatures, 25°C, 150°C and 240°C.

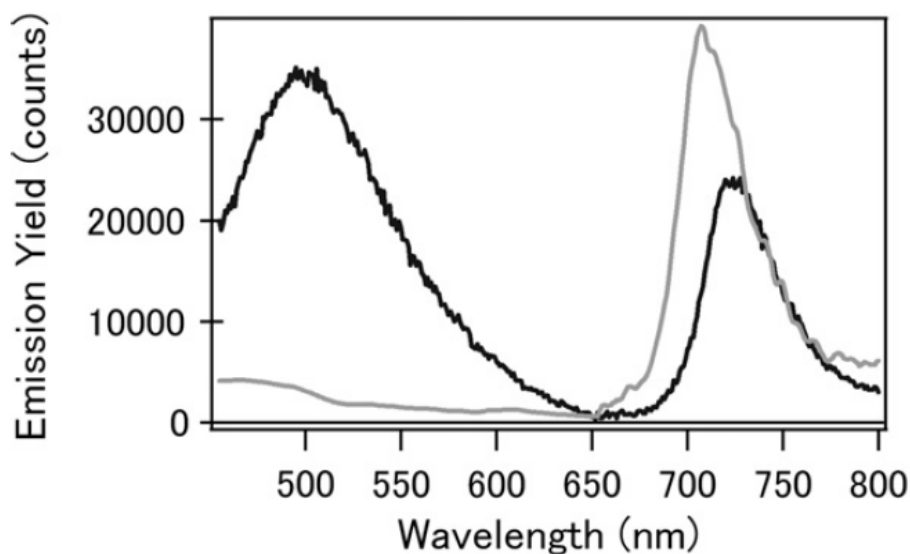


Figure 4-3. Figure from Cook et al. showing the CT-state emission and S_1 - S_0 emission of PCBM films of isolated (grey) and aggregated (black) PCBM molecules. $\lambda_{ex}=433$ nm.⁶⁸

In the same study of CT-state absorption, emission was observed from the CT-state as shown in Figure 4-3 (from Cook et al.).^{68, 69} Though the P-9-OPIMB/PCBM films do not show the exact same emission, a lower energy emission band is seen in the films, as shown in Figure 4-4. A long pass filter in these spectra obscures emission from P-9-OPIMB. The predominant S_1 - S_0 emission in PCBM is at 720 nm. The emission is quenched most in the as-spun (HNF) film and as the annealing temperature is increased the PCBM emission appears less quenched, recall that this occurs as the sample transitions from the HNF to the lamellar phase, chapter 3. Interestingly as the sample transitions from HNF to lamellar the emission at 590 nm is enhanced. This is not emission from the PCBM S_1 - S_0 or P-9-OPIMB. It is red-shifted relative to the reported PCBM CT state emission, but recall that the CT absorption in annealed films is also redshifted. It may be a charge transfer state formed between the two materials, which is enhanced with thermal annealing. Notably in neat films of PCBM I was not able to recreate the charge transfer state emission as shown in the cited work.

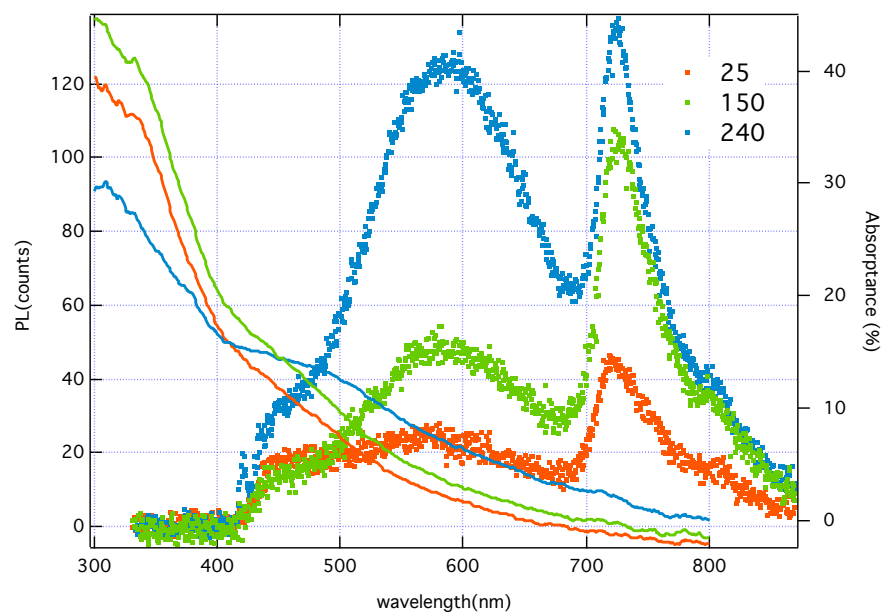


Figure 4-4. Absorption and photoluminescence of P-9-OPIMB/PCBM films annealed to three different temperatures, red is as-cast (annealed to 25°C), green is 150°C and blue is annealed to 240°C. The absorption of the CT state increases with increasing annealing temperature and the PL quenching rates decreases with increasing annealing temperature.

4.3 Photoconductivity of P-9-OPIMB in a Bilayer and Heterojunction

4.3.1 Photoconductivity Studies on P-9-OPIMB-C₆₀ Bilayer

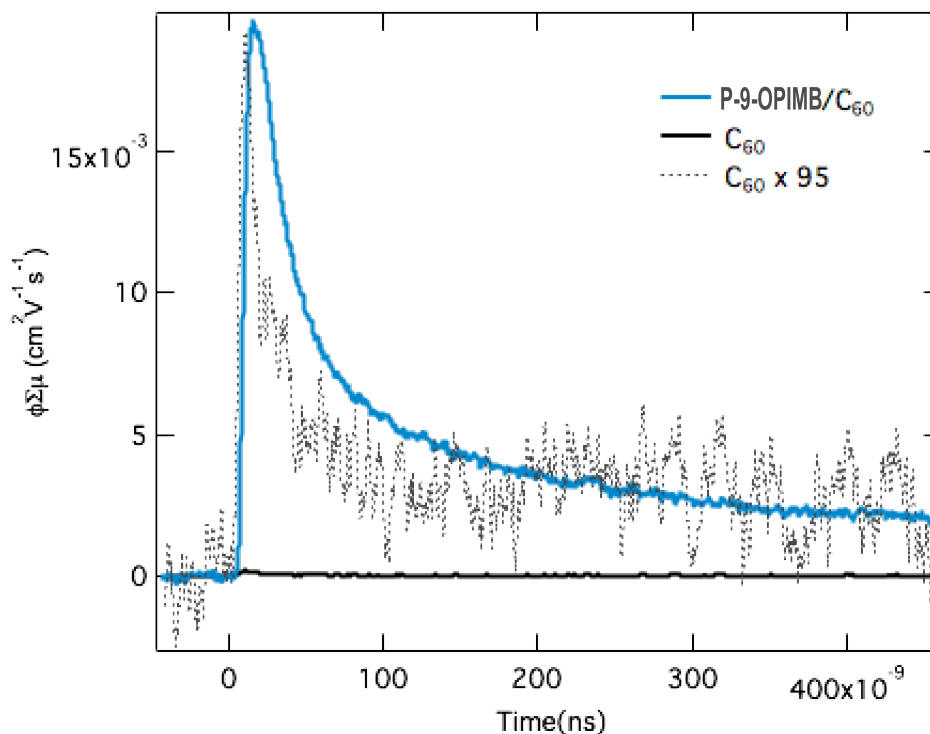


Figure 4-5. Yield-mobility product transients ($\Phi\Sigma\mu$) for films of neat C_{60} and bilayers of C_{60} on P-9-OPIMB nanofilaments. The P-9-OPIMB/ C_{60} sample has a 95x larger yield-mobility signal indicating a generation of photo-induced charges.

The system is first evaluated as a bilayer to measure photo-induced electron transfer between C_{60} and P-9-OPIMB helical nanofilaments. Extending on the thin film characterization above, here we deposit a 30 nm layer of C_{60} onto a thin-film of helical nanofilaments. C_{60} deposition minimizes the influence of the electron acceptor on the solid-state microstructure such as that shown in chapter 3 when incorporating a soluble fullerene into the P-9-OPIMB structure. In both samples, C_{60} is the sole absorbing species, and thus all excitons originate in the C_{60} layer. It should be noted that the bilayer films are likely not a true bilayer with a smooth interface, the

P-9-OPIMB thin film has a rough surface and the C₆₀ may penetrate into the P-9-OPIMB layer. Thus the two components may have a larger surface area than that of a discrete bilayer system.

Figure 4-5 compares the photoconductivity transient of a P-9-OPIMB-C₆₀ bilayer (blue trace) and a neat C₆₀ film (black trace) excited at 470 nm (6x10¹² photons/cm²). The photoconductivity of the bilayer films is 95 times larger than the neat C₆₀ film.

$$\phi\Sigma\mu = n_{eA}\mu_{eA} + n_{pA}\mu_{pA} + n_{eD}\mu_{eD} + n_{pD}\mu_{pD} \quad \text{Equation 4-2}$$

A direct relation can be made to the product of the number of charges in the system, ϕ , and their carrier mobility, μ , at ~8.9 GHz, as described in chapter 2. The complete yield-mobility product, $\phi\Sigma\mu$, is written out in Equation 4-2 (e is electron, p is hole, A is electron acceptor, and D is electron donor.) This simplifies when a donor and acceptor system are more efficient at generating charges between them than they are at generating charges within the same material. For example, photoexcited neat C₆₀ will yield some holes and electrons, despite the absence of an electron donor. Yet when photoexcited in the vicinity of an electron donor, such as P3HT, the energy of transfer to the donor is much more favorable and only electrons on C₆₀ significantly contribute to the yield-mobility signal. Analogously only holes remain on the electron donor. The product thus simplifies to Equation 4-3.

$$\phi\Sigma\mu = n_{eA}\mu_{eA} + n_{pD}\mu_{pD} \quad \text{Equation 4-3}$$

In a comparison of TRMC transients such as that in Figure 4-5 the signal enhancement may arise from a change in the maximum yield of charges generated per photon in the system or an increase in the overall carrier mobility. In this work, we disregard the charge generation mechanism, as the generation occurs in the time window of our excitation pulse (5 ns). The

signal decays rapidly as the charges recombine and encounter traps. Long-lived charges with the potential for extraction, such as those present at several hundred nanoseconds, are of particular interest to photovoltaic applications.

Photoconductance transients for the bilayer are evaluated by fitting the measured decays to a triexponential function, $F(t)$ (Equation 4-4), convolved with an instrument response function. The neat C_{60} film is better fit to a biexponential decay function. A maximum signal is obtained by extrapolating the decays to $t = 0$, a point in time that represents the largest number of photo-induced charges in the system.

$$F(t) = A_1 e^{-\frac{t}{\tau_1}} + A_2 e^{-\frac{t}{\tau_2}} + A_3 e^{-\frac{t}{\tau_3}} \quad \text{Equation 4-4}$$

The extrapolated, $t = 0$ post-pulse signal is the maximum yield-mobility product (Equation 4-3). The significant signal increase between the C_{60} and bilayer films suggests that the P-9-OPIMB helical nanofilaments are acting as a charge acceptor.

A sample consisting of 1 wt% $PC_{60}BM$ in P-9-OPIMB is measured to assess the liquid crystals' microwave mobility contribution. It will be shown in the following section that $PC_{60}BM$ undergoes photoinduced electron transfer with P-9-OPIMB, similar to C_{60} . The low weight percent mixing is used to minimize $PC_{60}BM$ clustering, and in so reduce the $PC_{60}BM$ electron contribution to the signal, as well as minimizing the structural changes in the HNFs. It is determined in the next section that the P-9-OPIMB microwave mobility (and consequently absorption component) is two orders of magnitude lower than that of C_{60} and thus does not contribute to the overall yield-mobility product. This allows for the direct comparison of the number of charges between the neat C_{60} and bilayer.

The initial $\phi\Sigma\mu_{t=0}$ signal is measured and plotted for a variety of light intensities and can be seen to follow the charge-exciton annihilation model previously described by Ferguson et al.³⁸ This is observed as an increasing signal yield with decreasing light intensity. The double-logarithm plotted data is fit to the empirical modified-Dicker equation, Equation 4-5, and shown in Figure 4-6.⁷⁰ At lower light intensities the signal asymptotically approaches A, where carrier yield is independent of the light intensity, and predictive of the signal at solar flux.

$$\phi_{t=0}\Sigma\mu = \frac{A}{1 + \sqrt{BI_0F_A + CI_0F_A}}$$

Equation 4-5

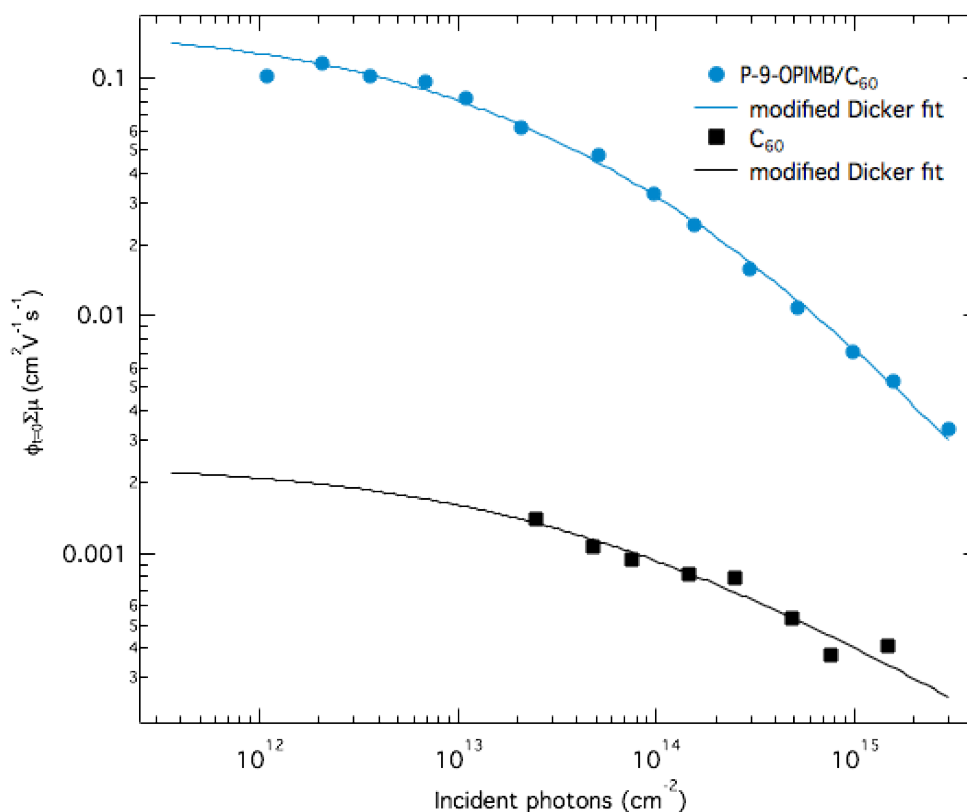


Figure 4-6. TRMC of P-9-OPIMB and C₆₀ bilayer films. Extrapolated $t = 0$ signal measured and plotted over different light intensities. The A value of the modified Dicker fit for the P-9-OPIMB/C₆₀ bilayer is 0.166 and 0.00240 for the C₆₀ film.

At low light intensity in the neat C₆₀ film the yield-mobility product contains the sum of the number of both electrons and holes and their respective mobilities. We estimate the yield from the value of A, with the assumption that the total number of photogenerated holes and electrons in the C₆₀ are equivalent, for each photogenerated electron there must be a corresponding hole and they will exist until combining with their respective counter-charge (though this is not a perfect assumption as charge trapping does occur and trapped charges do not contribute to the microwave absorption.) The signal is equal to the yield of electrons and C₆₀ electron mobility product, as shown in Equation 4-6.

$$\phi \Sigma \mu = n_{eC_{60}} \mu_{eC_{60}} + n_{pC_{60}} \mu_{pC_{60}} = n(\mu_{eC_{60}} + \mu_{pC_{60}}) \quad \text{Equation 4-6}$$

The lower-limit microwave mobility of the sum of the electron and hole charges in neat C₆₀ was previously determined using PR-TRMC, $\Sigma \mu_{C_{60}} = 0.29 \pm 0.07 \text{ cm}^2 \text{V}^{-1} \text{s}^{-1}$.^{45, 69} The large uncertainty associated with this mobility is a product of the pulse-radiolysis experiment, where the sample excitation arises from bombardment with electrons instead of photoexcitation. From an estimated charge yield, a mobility sum of holes and electrons in C₆₀ is extracted from the yield-mobility product. The charge carrier mobility of C₆₀ is dependent on crystallite size. Thus the previously reported C₆₀ electron mobility is merely an estimate of the mobility in these samples. Here we used the half PR-TRMC mobility to account for our observing only mobile electrons in the C₆₀/P-9-OPIMB samples.

Charge-generation yields are compared between the neat and bilayer samples by normalizing the signal by the measured C₆₀ microwave sum-of-mobility. Assuming the C₆₀ electron mobility dominates in both samples, a charge generation yield can be compared between the two samples. The neat C₆₀ film has a charge-generation yield of <1%, whereas the bilayer has

a yield of 100%, with error margins of 25%. The charge-generation yield increases by two orders of magnitude between neat C₆₀ and the bilayer, and the photoinduced charge generation for the bilayer is therefore high.

The large increase in charge generation shows that (1) the electron transfer from P-9-OPIMB to photo-excited C₆₀ is favorable and (2) the HNF surface leads to favorable contact between the P-9-OPIMB molecules and C₆₀ for efficient photoinduced electron transfer. This warrants further study as a charge-transfer interface.

4.3.2 P-9-OPIMB Microwave Conductivity Contribution

Samples of 1% PCBM in P-9-OPIMB were measured with TRMC, Figure 4-7, in order to evaluate the P-9-OPIMB mobility contribution. Samples were excited with 355 nm light, exciting both species in the thin films, as well as PCBM excited alone at 420 nm. Previous studies have demonstrated that low loadings of the donor can be used to isolate the mobility of a single constituent. In the work by Coffey et al., this was utilized to hold the mobility the same across a series of samples containing different electron acceptors to study the charge generation yield. In this case, a low acceptor ratio generates charges and the resulting yield-mobility is monitored. PCBM loading is low so that PCBM clustering is minimized, the electrons are immobilized and PCBM does not contribute to the TRMC yield-mobility product. The resulting yield-mobility product is the yield of holes and the hole carrier mobility of P-9-OPIMB, thus Equation 4-2 can be reduced to Equation 4-7.

$$\phi \sum_i \mu = n_{eA} \mu_{eA} + n_{pA} \mu_{pA} + n_{eD} \mu_{eD} + n_{pD} \mu_{pD} = n(\mu_{pP-9-OPIMB}) \quad \text{Equation 4-7}$$

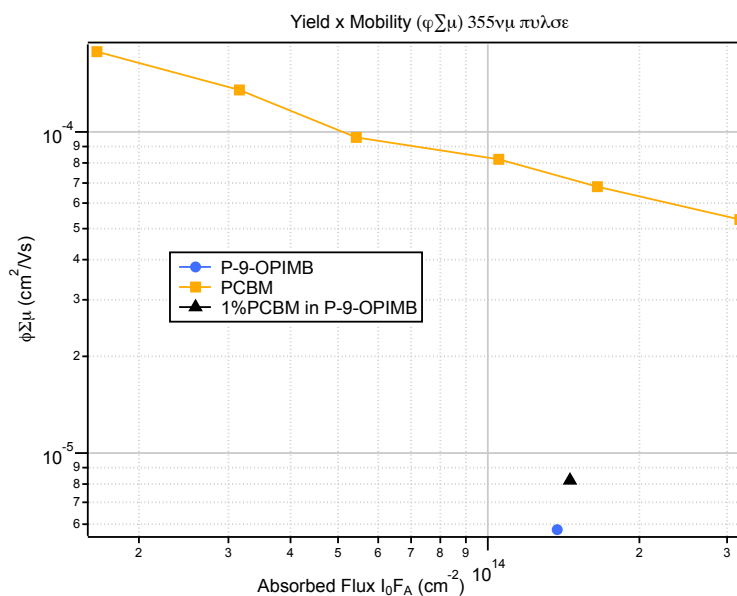


Figure 4-7. P-9-OPIMB, PCBM and 1% PCBM in P-9-OPIMB films measured with TRMC at different light intensity.

Neat P-9-OPIMB films yielded an order of magnitude smaller signal than neat PCBM films. Even with 1% PCBM doping excited at 355 nm, as in Figure 4-8, in which PET should occur from photoexcited PCBM to P-9-OPIMB the signal is low. P-9-OPIMB is also absorbing at this wavelength and appears to not contribute to the yield-mobility product.

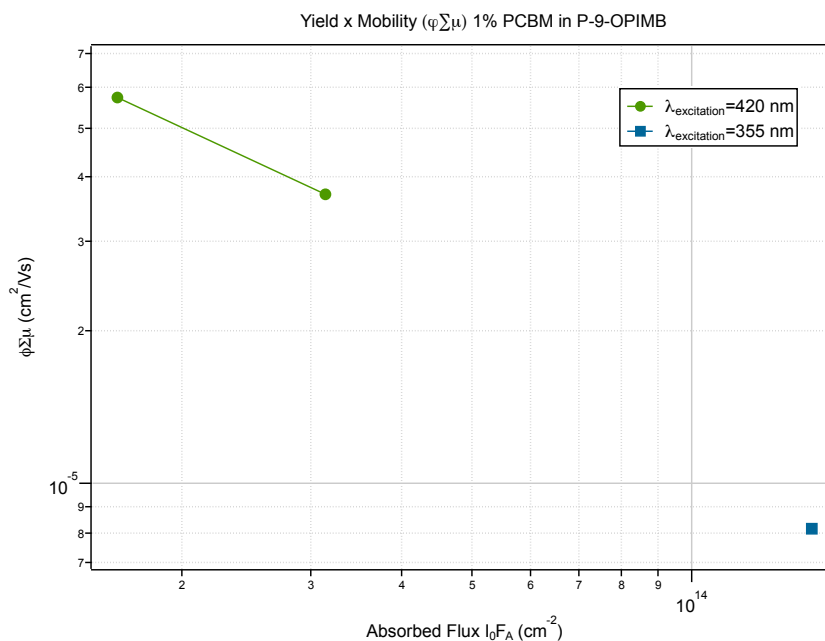


Figure 4-8. Yield-mobility product of 1% PCBM in P-9-OPIMB excited at 420 nm and 355 nm. The decrease in signal is attributed to P-9-OPIMB absorbing light at 355 nm at the expense of the PCBM absorption.

A higher signal is observed in sample excited at 420 nm sample, in which only PCBM is absorbing. The upper limit on charge generation yield should be 100%. Therefore we can extract a lower limit mobility for P-9-OPIMB of approximately $5 \times 10^{-5} \text{ cm}^2/\text{Vs}$. This yield-mobility value is derived from a high light intensity, in which nonlinear charge-exciton annihilation occurs, leading to a further underestimated of mobility. Though it is not an unusually low value, the P-9-OPIMB hole mobility is substantially lower than C_{60} and PCBM, 0.29 and $0.05 \text{ cm}^2 \text{V}^{-1} \text{s}^{-1}$ respectively, and is not considered a contributing mobility in the bilayer and heterojunction TRMC signals.

4.3.3 PCBM Photoconductivity at Different Wavelengths

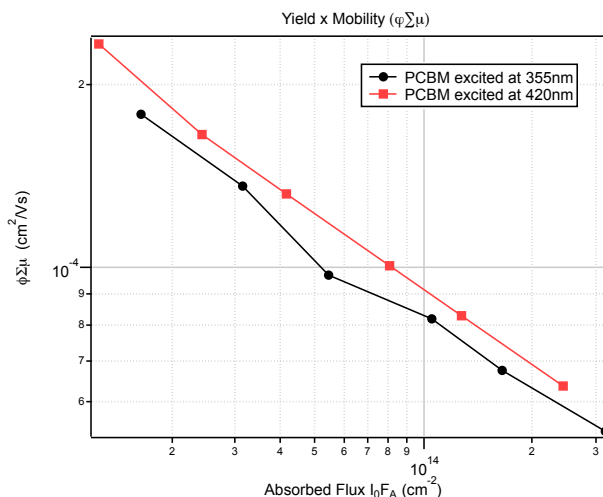


Figure 4-9. Comparison of the yield-mobility product for the same film of PCBM excited at different wavelengths. The difference in signal is within the error range of the measurement.

Neat PCBM films demonstrate a very similar yield-mobility product when excited at either 355 nm or 420 nm, Figure 4-9. Thus the generation of charges in the neat PCBM sample is wavelength independent.

4.3.4 Photoconductivity Studies on P-9-OPIMB-PC₆₀BM Blends

As was determined from the TEM and XRD data, two distinct morphologies are created when mixing P-9-OPIMB and PC₆₀BM and processing under different conditions. Here we compare those morphologies as bulk heterojunctions and probe charge-generation with TRMC.

Just as in the comparison made between carrier mobilities in P-9-OPIMB and C₆₀, electrons in the PC₆₀BM have a larger mobility than holes in P-9-OPIMB. Thus in the 50/50 mixtures, the microwave mobility contribution of holes in P-9-OPIMB is also minimal, and the signal in these samples is dominated by electrons in the clustered PC₆₀BM.

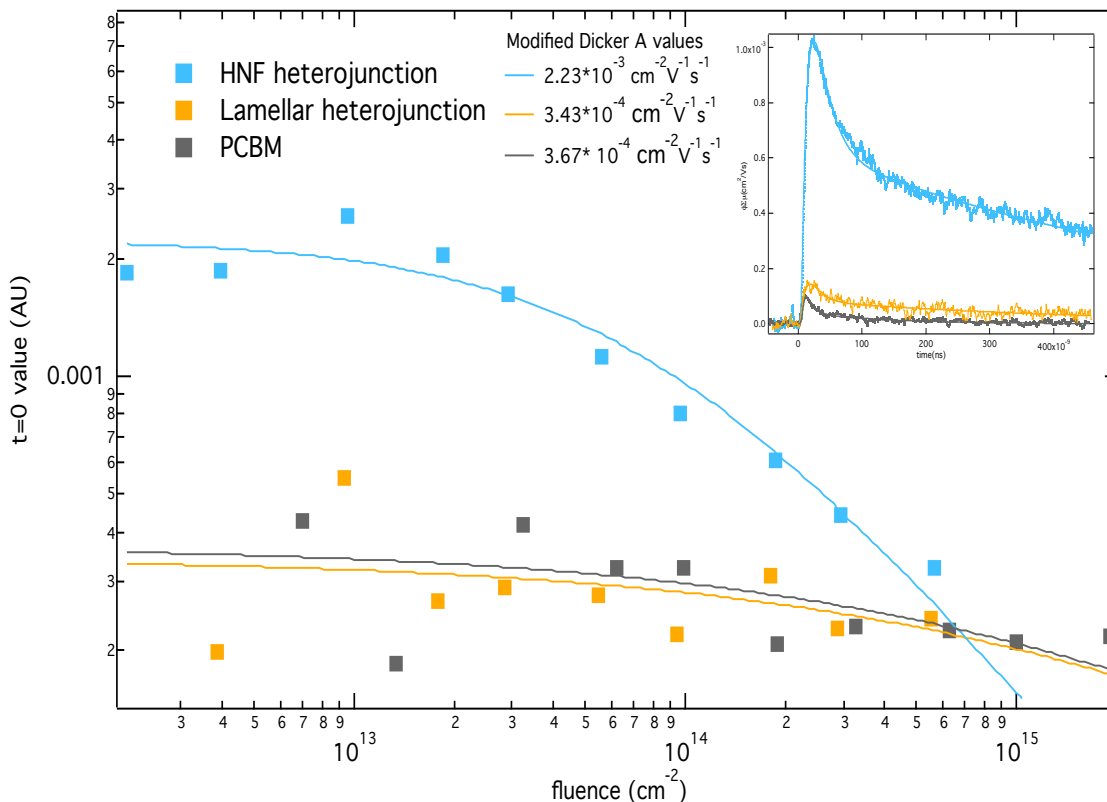


Figure 4-10. Similar to the charge generation results from the HNF-C₆₀ bilayer the HNF heterojunction thin films confirms that HNFs act as a “good charge-generating interface”. In addition to the increase in t = 0 signal. The HNF heterojunctions have much longer-lived charges (inset).

Figure 4-10 shows the TRMC yield-mobility product signal for HNF and lamellar P-9-OPIMB/PC₆₀BM films as well as neat PC₆₀BM films as a function of light intensity. The HNF heterojunction shows nearly an order of magnitude larger signal than the lamellar sample. Additionally, the lamellar heterojunction signal is very similar to that of neat PC₆₀BM. Modified Dicker A-values showed that at low light intensity the HNF sample has an order of magnitude larger signal than the lamellar sample. Two possible explanations for this finding are presented below; the first is a morphological explanation and the second is a photophysical explanation.

The TEM images of the lamellar annealed P-9-OPIMB/PC₆₀BM heterojunction show the presence of large ~50 nm PC₆₀BM clusters. From the images it is unclear whether these clusters exist as droplets on the lamellar surface or spheres that penetrate into the lamellar layers. The lack of charge transfer that occurs between PC₆₀BM and P-9-OPIMB in this system suggests that it may exist as the former. The layer of P-9-OPIMB alkyl tails may be acting as an insulator between PC₆₀BM and the electron-donating P-9-OPIMB core at the heterojunction interface; ultimately inhibiting PET.

Another conjecture for the lack of photogenerated charges in the lamellar system relates to the CT-state presented in the lamellar heterojunction absorption and photoluminescence. Recall from the kinetic scheme in Figure 2-6 that separated charges must pass through a charge transfer intermediate state. But if the charge transfer state is itself emissive, as is the case for the lamellar heterojunction, the two pathways are in competition. Therefore the charge transfer state formed between the PCBM and P-9-OPIMB in the lamellar microstructured heterojunction may be acting as a trap when going from the excited state, D*, to the separated charges.

The HNF phase is shown to have an effective interface as a bilayer with C₆₀ for PET. Additionally, it is shown to increase the charge-generation in a heterojunction with PC₆₀BM as compared to a lamellar packing of the same materials.

4.3.5 Heterojunction P-9-OPIMB/PCBM Lifetime

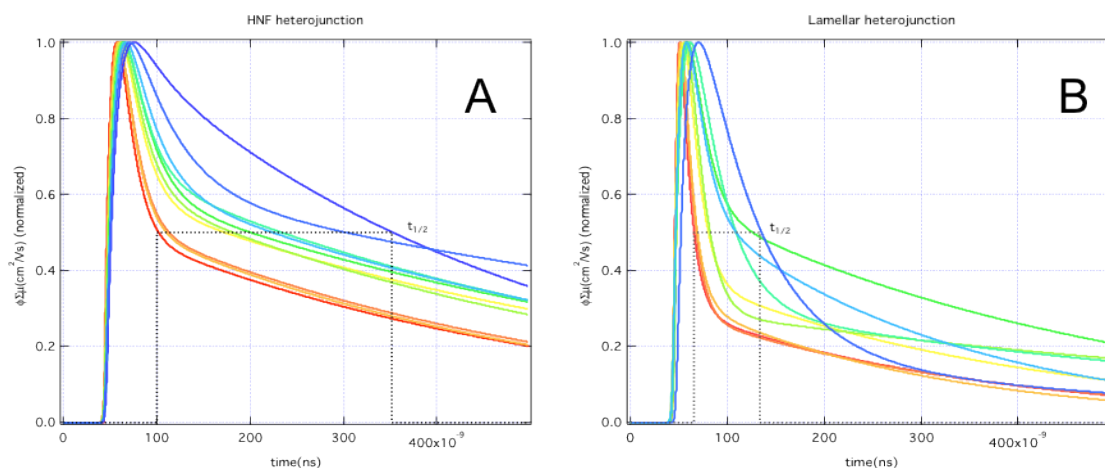


Figure 4-11. Normalized TRMC transients over different light intensities in A) HNF heterojunction sample of P-9-OPIMB and PCBM and B) a lamellar microstructured heterojunction of the same components.

Charge lifetimes were compared with half-life decays ($t_{1/2}$) of the normalized microwave conductivity transients excited at different light intensities in HNF and lamellar heterojunction samples. In HNF heterojunction films, Figure 4-11A, the $t_{1/2}$ was highly dependent on light intensity, and was shown to be over 300 ns at low ($\sim 10^{12}$ photons/cm²) light intensities. The lamellar heterojunction samples, Figure 4-11B, showed minimal light dependence on the decays and the longest $t_{1/2}$ was below 100 ns, a sample of neat PCBM has a $t_{1/2}$ of less than 20 ns. This shows that in addition to an overall larger microwave absorption signal, the charges in the HNF heterojunction are considerably longer lived than those in the lamellar heterojunction. This is an indication that charges are able to move away from each other once generated in the HNF film, whereas they may remain localized near PCBM and recombine in the lamellar sample.

4.3.6 Temperature Dependency of P-9-OPIMB/PCBM Blend Photoconductivity

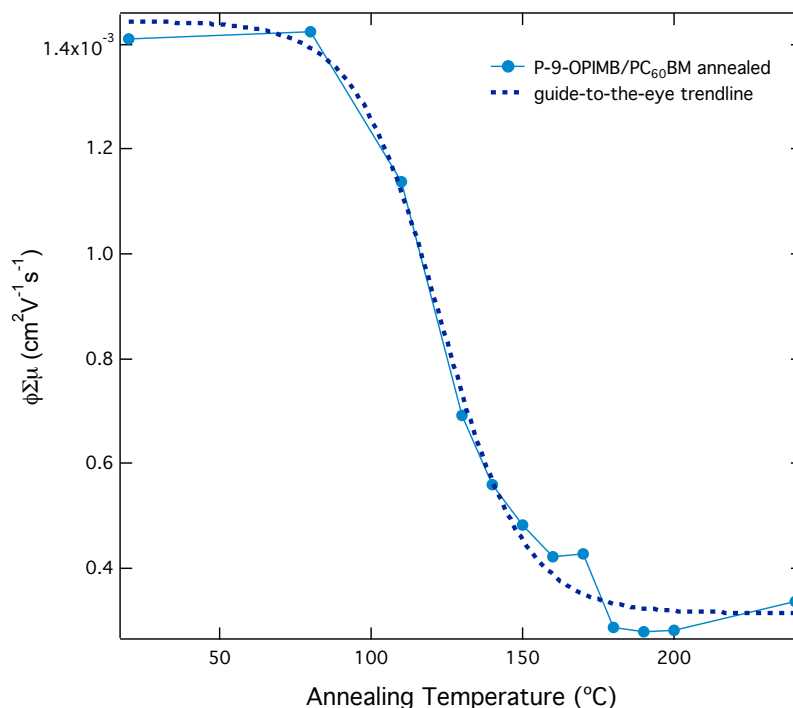


Figure 4-12. Yield-mobility product of heterojunction samples as a function of annealing temperature. The yield-mobility product decreases with increasing annealed temperature.

Samples of 50/50 P-9-OPIMB/PCBM annealed at different temperatures are studied with TRMC. The yield-mobility product is plotted against annealing temperature in Figure 4-12. Annealing temperatures up to 80°C, below the glass transition of HNFs, has no noticeable effect on the yield-mobility. Yield-mobility is inversely related to annealing temperature between the onset of the glass transition and the $\text{SmC}_{\text{A}}\text{P}_{\text{A}}$ phase. Samples annealed above the isotropic transition were the lowest yield-mobility and increasing temperature no longer led to a lower signal.

The thin film is gradually transitioning between the HNF phase and a lamellar structuring. The lamellar transition “turns-on” at the glass transition, and slowly turns to lamellar

through the melting point, at which it is fully transitioned and no longer changes with temperature.

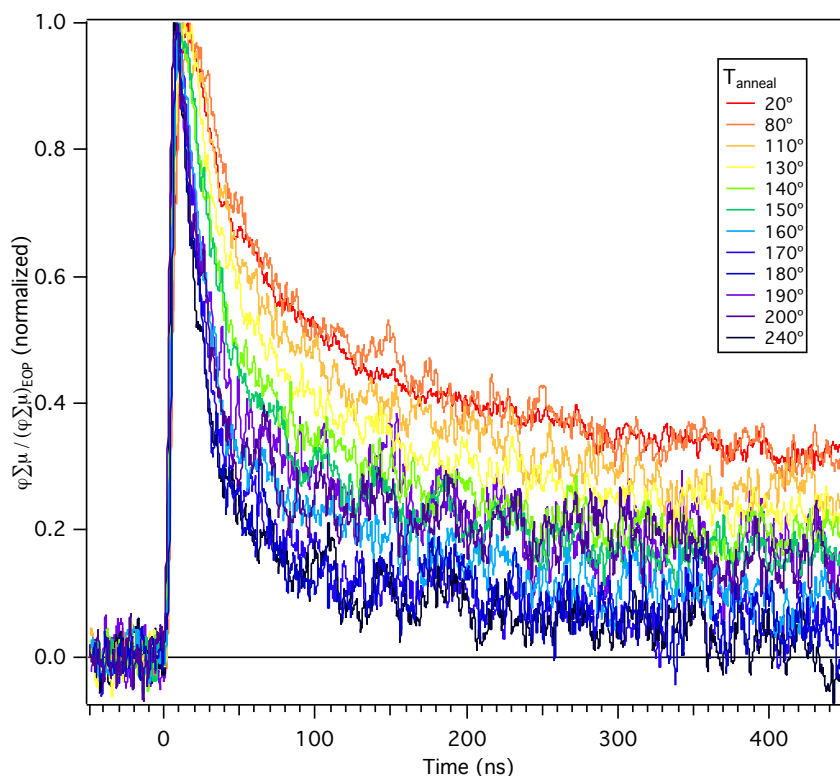


Figure 4-13. Photoconductivity decay comparison of P-9-OPIMB/PC₆₀BM samples annealed to various temperatures between room temperature and 240°C. All photoconductance transients excited at 420 nm with an absorbed flux of 1×10^{13} photons/cm².

Transient lifetimes were also greatly affected by the temperature of annealing, as demonstrated in the normalized photo-transients shown in Figure 4-13 and similar to that seen in Figure 4-11. The lifetime follows a similar trend to the yield described above. The lifetime gradually transitions between the long-lived charges in the room temperature annealed sample to the quick decay of the 160°C sample (SmC_AP_A phase.) Thus samples annealed to SmC_AP_A are different from those annealed above the glass transition temperature.

4.3.7 Photoconductivity of PC₇₀BM/HNF Heterojunctions

One interesting and unaccounted for result that was found in this work is that PC₇₀BM and PC₆₀BM gave disparate charge generation results, as shown in Figure 4-14. Typically, the HOMO and LUMO energy levels of these two fullerenes are reported to be similar, within 30 meV of one another.⁴ The microstructure studies of chapter 3 showed that PC₇₀BM causes a similar microstructure as PC₆₀BM when annealed, yet the increase in photoconductivity is not seen in these yield-mobility products. This may indicate that the HOMO of P-9-OPIMB is favorable for charge transfer to the HOMO of PC₆₀BM yet unfavorably to that of PC₇₀BM.

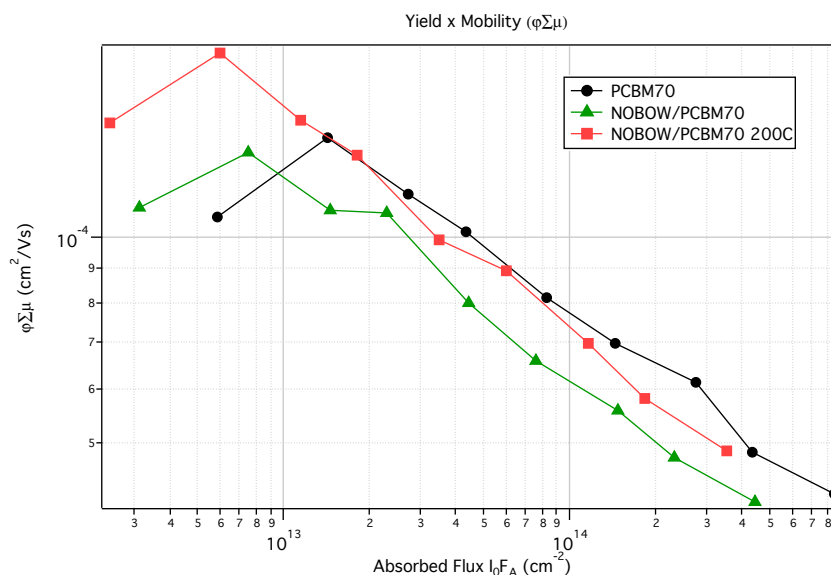


Figure 4-14. P-9-OPIMB/PC₇₀BM HNF and lamellar heterojunctions microwave absorption measured at different light intensities and compared to neat PC₇₀BM. Photoinduced electron transfer does not occur.

4.4 Conclusions

Photoinduced charge generation in HNF films was studied with a variety of experiments in order to verify the viability of the HNF phase as an OPV ordered heterojunction. In bilayers of

HNF/C₆₀, the HNF phase is shown to readily undergo photoinduced charge separation. This is very promising for HNFs in OPV, yet the story gets more complicated as it is mixed with electron acceptors, particularly PC₆₀BM.

A distinct difference in TRMC signal is measured between the 2 microstructures of the P-9-OPIMB/PCBM heterojunction and may be attributable to several issues. As shown in chapter 3, PCBM tends to cluster in the thin films when annealed. This could be physically separating the two components and leading to a decrease in total yield-mobility. What is more the microstructuring of the annealed film forms a homeotropic lamellar phase with the tops of the layers covered in aliphatic P-9-OPIMB tails. This may be creating a physical separation from the PC₆₀BM. Another conjecture is that an emissive charge-transfer state has created a competing pathway in the heterojunction samples. It was seen that an emissive charge-transfer state is generated between the PCBM and P-9-OPIMB in annealed samples that increased in emissivity as a function of annealing temperature. Similarly a decrease in the yield-mobility product is seen as a function of annealing temperature. The rate of electron transfer and rate of charge transfer state emission are in competition and may be hindering the charge generation.

The growth of large (50 nm) PCBM clusters, may also be causing the unusual charge transfer emission, and thus it is likely a tradeoff between these two phenomenon that leads to the substantial photoconductivity differences between the HNF and lamellar samples. The slow transition of the yield-mobility product and slow change in decay dynamics with temperature points to this being the case.

The HNF phase is shown to be an effective exciton dissociation interface but it is also a cautionary tail about soluble fullerenes role in active layer microstructure and the subsequent

Chapter V: Solution Optical and Electrochemical Characterization of n,2-OBTTT

5.1 Introduction to the n,2-OBTTT Series

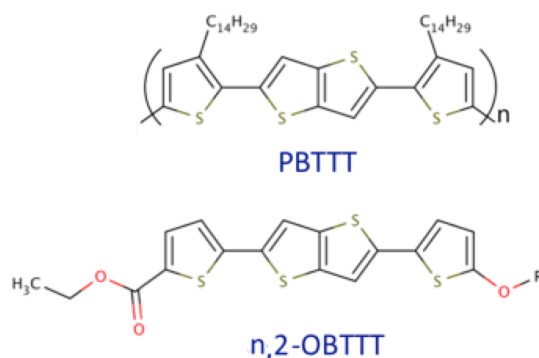


Figure 5-1. Molecular structures of PBTTT and the newly designed and synthesized model compound, n,2-OBTTT, characterized in this work, where $R = C_nH_{2n+1}$ and $n = 1-13$. The photophysical and electrochemical properties show no variation between molecules with different tail lengths.

The solution photophysical and electrochemical characterization of oligothiophenic small molecules, ethyl 5-(5-(5-alkoxythiophen-2-yl)thieno[3,2-b]thiophen-2-yl)thiophene-2-carboxylate, n,2-OBTTT, Figure 5-1, are included in this chapter. These molecules are designed as a modified monomer of the highly cited, high carrier mobility polymer, poly[2,5-bis(3-alkylthiophen-2-yl)thieno[3,2-b]thiophene], PBTTT, Figure 5-1.^{71, 72} This polymer has received significant attention in the OPV community for its exceptionally high hole carrier mobility and distinct mixing with solution fullerenes, in which fullerenes intercalate between the alkyl sidegroups of the crystallized polymer.^{73, 74} Absorption, photoluminescence and cyclic voltammetry measurements are used herein to compare the molecular properties across a series in which the alkoxy tail length is the only molecular modification. The linear aliphatic tails in the

series, R, vary from 1 to 13 carbons. The chromophore is unchanged across the series and would be expected to yield interchangeable optical and electronic properties between any two monomers.

5.1.1 Small Molecule Model Compound Studies

Small molecular model compounds are a useful way to systematically characterize the basic physical characteristics of a polymer species.⁷⁵ High molecular weight polymers suffer from varying solubility and which limits solution-phase characterization techniques. What is more, polymer samples exist as of a distribution of molecular weights and thus repeating monomer lengths (defined as the polydispersity), this leads to a broadening of properties, an obstacle to determining the origins of many optical, morphological and electronic properties. Even within a soluble and minimally polydisperse sample, i.e. uniform length, polymers are particularly susceptible to solvent effects, and may exist as dissolved isolate chains, small aggregates or large aggregates and a variety of morphologies within any specific solvent, Figure 5-2. Studying a small portion of the polymer structure or a derivatized portion is one way to work around these effects. The property effects of one molecular modification can be characterized and extrapolated to approximate a polymer.

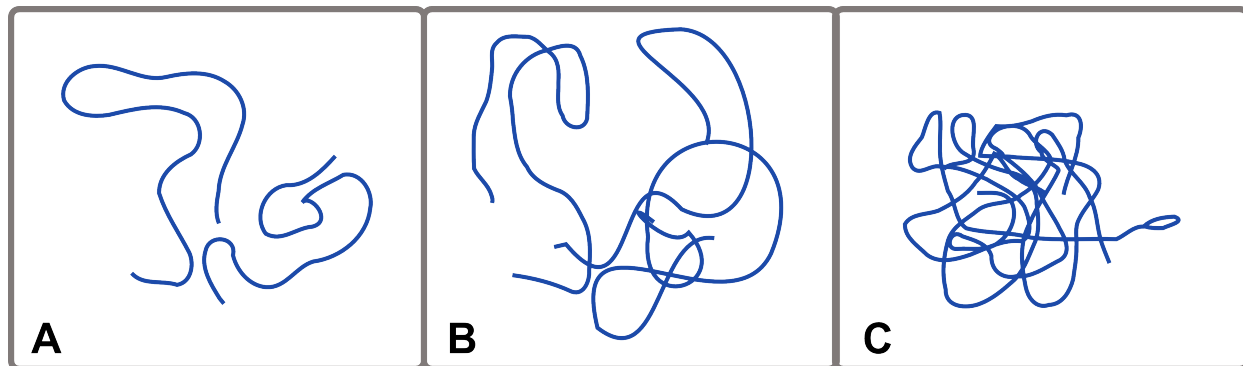


Figure 5-2. Simplified schematic depicting three different dissolved polymers in solution, A) the non-interacting polymer, B) polymer chains interacting and C) clustered polymers. Polymers exhibit clustering to different degrees in different solvents, in particular the intermolecular interactions in clustered polymer chains can lead to a shifting of properties, e.g. H- or J-aggregation.

5.1.2 Previously Reported Model Compound Studies

Model compounds for other conducting polymer systems include molecules such as oligothiophenes to study P3HT. One oligothiophene photophysical study showed that substitution of furan or pyrrole can substantially influence the resulting spin-orbit coupling and consequently triplet formation.⁷⁶ Oligomeric phenylenevinylene were used to elucidate the correlation between morphology and optical properties in PPV (poly-phenylenevinylene) for LED and OPV applications.⁷⁷ Lastly oligofluorenes were utilized to identify the origins of a strong green absorption feature (previously speculated to come from inter-chain absorption but tri-fluorenes proved the absorption to occur directly onto the chain.)⁷⁸

One distinct aspect of the molecules studied herein is the presence of the fused thiophene unit, thienothiophene. Only a few references were found to thienothiophene containing and in particular BTTT-containing small molecule studies, this highlights the relevance and value of this basic characterization work.^{12, 79, 80}

5.1.3 Previous work on PBTTT

As mentioned, this work is focused on PBTTT model compounds. PBTTT is known for its exceptionally high hole carrier mobility, measured up to $0.7 \text{ cm}^2\text{V}^{-1}\text{s}^{-1}$, which is similar to the mobility of amorphous silicon.⁷¹ Despite high carrier mobility and superior absorption properties, the highly anticipated PBTTT photovoltaic devices had an unremarkable power conversion efficiency of just over 2% when blended with PCBM at an optimized ratio of 1:4 by weight.⁷² Diffraction experiments showed that fullerenes intercalate in between the polymer alkyl tails, thereby isolating fullerenes in these pockets and shutting down electron transport through fullerenes. Thus devices required a high loading of fullerenes, in which electrons transport through the excess fullerenes, for functioning devices.⁷³ Notably this polymer was demonstrated to form the high carrier mobility crystal phases after cooling from a liquid crystal transition.

5.1.4 Helical Nanofilament Forming Mesogen Motivation

In the previous chapter, HNFs were shown to be an efficient photo-induced charge generation microstructure. One limitation of currently known HNF-forming mesogens is their limited absorptive overlap with the solar spectrum. Solar absorption is essential to a functioning solar device, necessitating the design of low band gap mesogens that absorb more of the solar spectrum. The molecules studied herein were originally synthesized as a protected-building block for such a mesogen. The ethyl ester protects the carboxylic acid designed for coupling via Steglich esterification to resorcinol or 3,4-biphenol. Ultimately these will make the target mesogens A and B, Figure 5-3. Future work in the Walba lab will include the synthesis and full characterization of A and B to determine if HNF phases are formed.

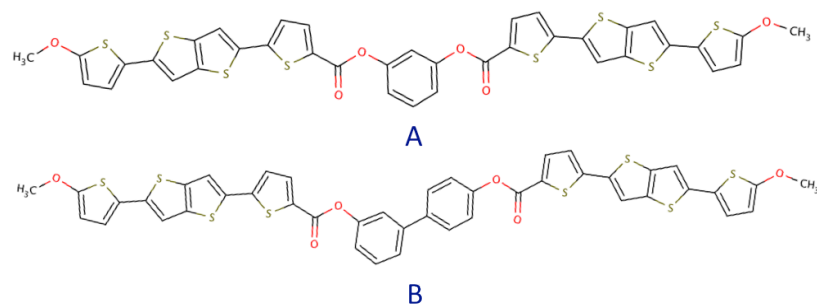


Figure 5-3. Target PBTTT-inspired small molecule mesogens designed to form helical nanofilaments. The arm units are identical to those characterized herein, with two different core units that are used in other HNF-forming mesogens.

The OBTTT molecules contain the entire chromophore that will be incorporated into the A and B mesogens, though there will actually be two uncoupled chromophores per molecule. The solution characterization in this chapter is a good predictor of the final product solution-phase optical and electrochemical properties.

5.1.5 Basic Properties of n,2-OBTTT

N,2-OBTTT, Figure 5-1, molecules range in tail length from methoxy to tridecyloxy (1 to 13 carbons) alkyl tails connected to the chromophore through an ether linkage. All compounds are yellow in solution but range from yellow to orange as crystals, indicating a shift in absorption properties between solution and solid as well as across the series of tail lengths. Each of the homologues undergoes liquid crystal phase transitions on heating. Solid-state properties of the n,2-OBTTT series are described in chapter 6. The n,2-OBTTT molecules are soluble in a variety of organic solvents, including chloroform, toluene, dichlorobenzene and sparingly soluble in acetonitrile. The longer-tail homologues are somewhat less soluble than the shorter tails, contrary to standard perceptions regarding the effect of tail length on solubility.

The alkoxy tail unit is included to mimic the P-9-OPIMB arm unit tail, as well as to aid the formation of liquid crystal phases. In addition to their use in liquid crystals, alkoxy tails can be found as polymer sidechains incorporated to increase solubility, such as in the P3HT analog P3HOT, poly-3-hexyloxythiophene, or MEH-PPV.⁸¹ PBTTT itself does not contain alkoxy sidechains, but instead alkyl sidechains. As mentioned above the solubility of PBTTT is very low, and often requires hot chlorinated solvents for dissolution, leading to complicated solution characterization techniques.

5.2 Absorption Characterization of n,2-OBTTT Solutions

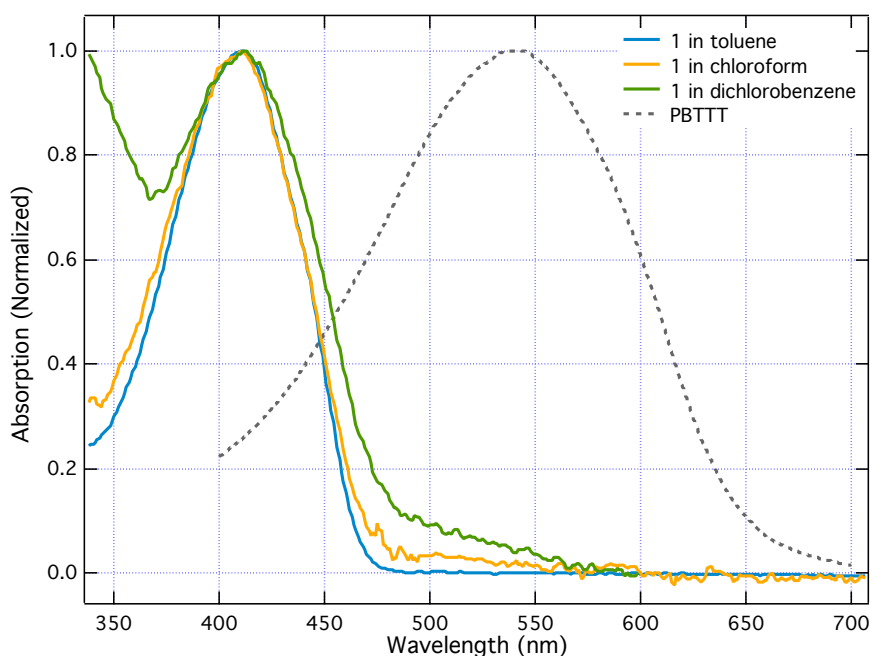


Figure 5-4. Normalized absorption spectra of 1,2-OBTTT in various solvents compared to PBTTT. Solvent is shown to have minimal effect on the absorption profile. The small molecule absorption is blue-shifted (410 nm) from the polymer absorption (540 nm).

As shown in Figure 5-4 the peak molecular absorption across the series is at 410 nm (3.02 eV). There is a subtle absorption shoulder at 445 nm. As shown in Figure 5-4, 1,2-OBTTT peak absorption of the model compound is blueshifted 720 meV relative to the continuously

conjugated PBTTT. Minimal differences are observed in the n,2-OBTTT absorption spectra as measured in different solvents.

Similar model compounds have been previously studied that consist of the thiophene-sandwiched thienothiophene unit 'BTTT' capped with benzene and naphthyl units on both sides of the central chromophore, with alkyl tails at the 3 (beta) position.¹⁰ Interestingly, the model compounds herein absorb a slightly lower energy than those compounds (peak absorption of 410 nm versus 400 nm). This may indicate that the benzene unit on the published molecules are actually not planar with the BTTT unit and thus is not further delocalizing the LUMO level and in the case of n,2-OBTTT the alkoxy group is contributing to the frontier orbital energy levels. Woodward-Fieser rules of substitutional effects on absorption predict a red shift of 6nm for an alkoxy group substituted onto an alkene chromophore.

Molar absorptivity is calculated from the peak absorption in toluene is presented in Table 5-1 with other measured photophysical properties. No systematic change in absorption spectral features or molar absorptivity is observed across the series, thus the tail length has minimal effect on the absorption. The variation in absorptivity values can be used as an indication of the error in the sample preparation and measurement. Moderate variation of photophysical properties is observed in different solvents indicating some solvent effects, for clarity we are reporting values as measured in toluene.

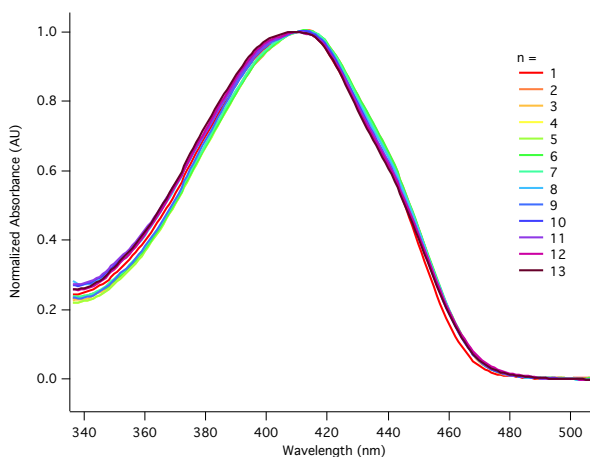


Figure 5-5. Normalized absorption curves of n,2-OBTTT in toluene demonstrate the general absorption shape uniformity across the series, though a subtle shift in the peak absorption is seen to vary, shifting to lower energy with increasing tail length.

Absorption normalized by the peak, shown in Figure 5-5, confirms the minimal change in the structure of the absorption (shifting from $\lambda_{\text{max}} = 400$ nm for 1,2-OBTTT to $\lambda_{\text{max}} = 410$ nm for 13,2-OBTTT) across the series. The peak absorption shifts slightly with increasing tail length, which could be an electronic shift or an apparent shift due to a higher energy absorption growing in.

5.3 Steady-State Photoluminescence of n,2-OBTTT Solutions

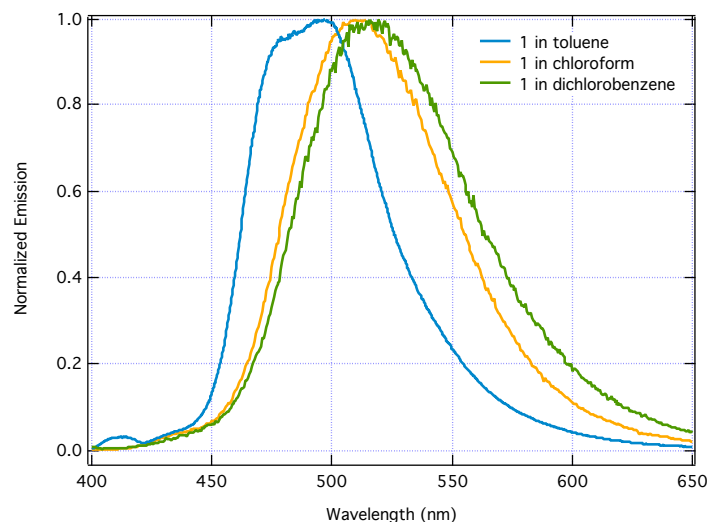


Figure 5-6. Photoluminescence spectra of 1,2-OBTTT in different solvents indicate a change in Stokes shift between the molecules in toluene and chloroform/dichlorobenzene. The latter solvents have a higher dielectric constant compared to toluene.

Photoluminescence was measured across the series in solutions of toluene, chlorobenzene and chloroform. Normalized emission spectra of 1,2-OBTTT in each solvent are shown in Figure 5-5. The PL spectrum changes modestly between toluene and the chlorinated solvents, both in the energy of the emitted radiation and the spectral shape. Recall that the absorption is nearly identical in toluene and chloroform, yet radiative emission in toluene is a higher energy emission than in the chlorinated solvents, from 520 nm to 490 nm. The additional structural features of the fluorescence in toluene are not mirrored in the absorption, Figure 5-4.

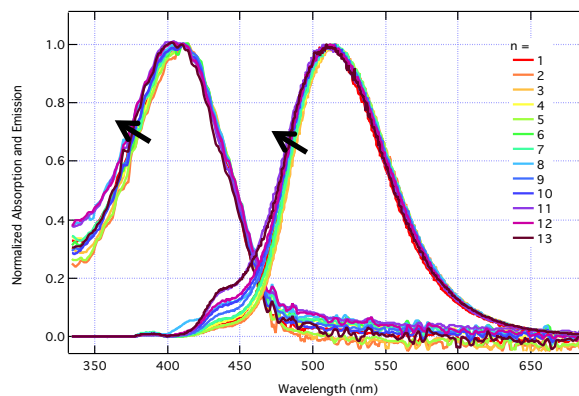


Figure 5-7. Normalized absorption and emission of n,2-OBTtT in chloroform. The arrows are a guide to the eye demonstrating the subtle shift of absorption and emission to higher energies with increasing tail lengths.

Emission shapes within a single solvent across the series are indistinguishable. Although a subtle shift in peak fluorescence is observed across the series, similar to the absorption, Figure 5-7. Again this may be due to a higher energy emission growing in.

5.3.1 Relative Fluorescence Quantum Yield Determination for n,2-OBTtT

Relative quantum yields were determined by comparing the total fluorescence of each n,2-OBTtT to the fluorescence of a standard dye, Lumogen yellow 083. The yield is calculated from Equation 5-1,⁴⁶ all measurements were made in toluene ($n = 1.5$) with optical densities of about 0.1. The excitation wavelength was chosen as 420 nm to match an absorption peak in the reference absorption. Lumogen yellow 083, a perylene derivative, has a quantum yield of 1.⁸²

$$\Phi_{sample} = \Phi_{ref} \frac{F(1 - \exp(-A_{ref} \ln 10))n^2}{F_{ref}(1 - \exp(-A \ln 10))n_{ref}^2}$$

Equation 5-1

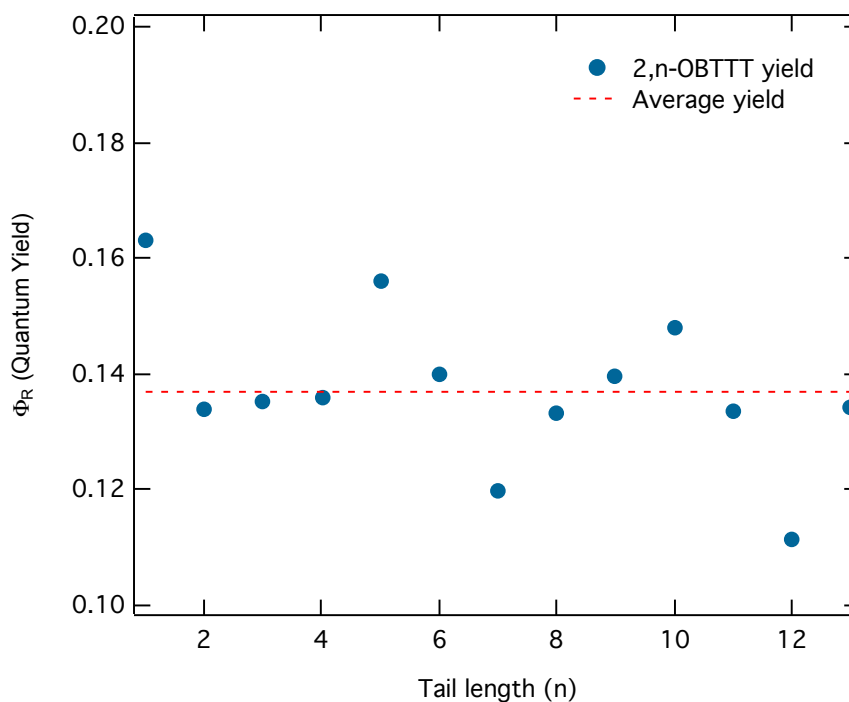


Figure 5-8. Measured relative quantum yields of the model compounds in toluene are plotted versus tail length, indicating a lack of quantum yield trend with tail length. The dashed line corresponds to an average across the series for contrast.

As Figure 5-8 shows the averaged *n*,2-OBTTT quantum yield is in good correlation with the average quantum yield, $\Phi = 13.7\%$. $\Phi_{\min} = 11.2\%$ and $\Phi_{\max} = 16.3\%$ and are the dodecyloxy and methyloxy respectively.

The fluorescence quantum yield of a solution of degassed 6,2-OBTTT is compared to that of as-prepared 6,2-OBTTT to evaluate the effect of oxygen on the emission of *n*,2-OBTTT. When evaluated using the degassed solution as the reference in Equation 5-1, the relative yield was 99.5% of a degassed sample, far within the experimental error of the measurement. Thus dissolved oxygen has minimal effect on the fluorescence of *n*,2-OBTTT.

A set of samples made from toluene stock solutions of *n*,2-OBTTT were also measured for quantum yield and show a tail-length dependence on yield. A higher energy absorption band

is also observed to grow in the samples with lower yield. Photoluminescence was measured from this higher energy absorption and showed a distinct and blue-shifted emission from the n,2-OBT TT molecules. Sonication was used to test if the effect was due to the formation of H-aggregates, aggregates would break up with sonication and dissolve into the toluene leading to a shift of the absorption and fluorescence back to that previously measured. But sonication further enhanced the observed higher energy absorption and emission. Thus the energy shift is likely due to the degradation of the chromophore, indicating that the molecules are likely indicating the instability of the molecules in solution over long periods of time (stock solutions were three months old). The stability of the molecules, which were in identical concentrations and otherwise treated identically, is shown to depend on tail length; methoxyloxy-hexyloxy tails are stable and the heptyloxy-tridecyloxy tails are increasingly less-stable with increasing tail length.

5.3.2 Time-Resolved Photoluminescence of n,2-OBTTT

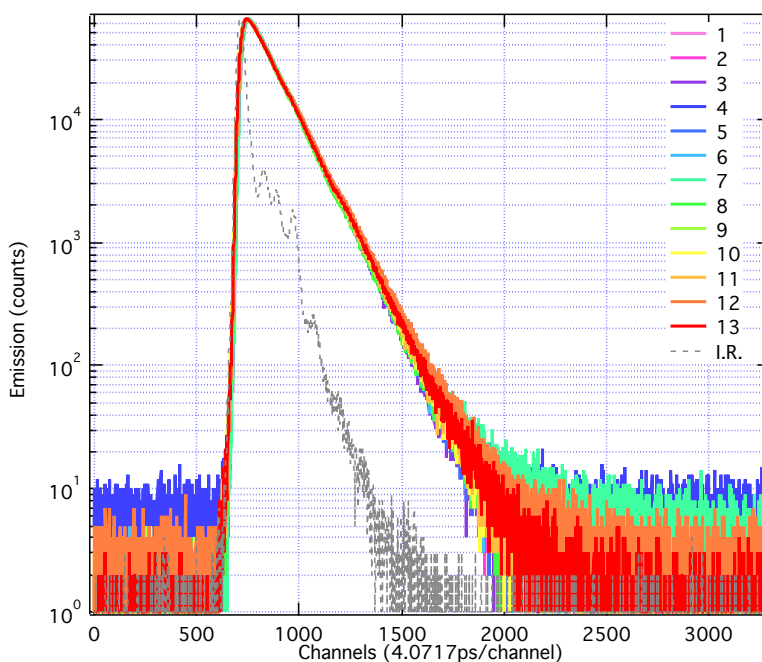


Figure 5-9. Time-resolved photoluminescence of the n,2-OBTTT series shown with the instrument response function, I.R. (dashed line). The signals of all n,2-OBTTT molecules are indistinguishable thus the rate of radiant emission is not changing with different tail lengths.

Fluorescence decay rates are measured across the n,2-OBTTT series in toluene and dichlorobenzene with time-correlated single photon counting (TCSPC), transients shown in Figure 5-9. The measured transient is fit with a monoexponential decay function, τ_{PL} , convoluted with a measured instrument response. For molecules in toluene the average time-constant, τ_{PL} , is 0.4 ns, specific measured values are shown in Table 5-2. The time constant in chlorobenzene is about 0.7 ns.

5.3.3 Determination of k_r and Oscillator Strength (f_{nm})

Using the measured quantum yields, ϕ , and fluorescence time constant, τ_{PL} , we can calculate the natural radiative rate constant, k_r , of the species, as in Equation 5-2.

$$\Phi = \frac{k_r}{k_r + k_{nr}} = k_r \tau_{PL} \quad \text{Equation 5-2}$$

$$k_{SB} = \frac{8\pi 2303 n^2 c}{N_A} \langle \nu_f^{-3} \rangle^{-1} \int \frac{\epsilon}{\nu} d\nu \quad \text{Equation 5-3}$$

The natural radiative rate constant, k_{SB} , can also be calculated independently from the absorption and fluorescence spectra with the Equation 5-3 from work by Strickler and Berg.⁸³ The original equation also accounts for the degeneracy in the S_1 and S_0 energy states, but here they are assumed to be single states. The absorption peak of a very dilute solution (OD = 0.04 AU) was fit to a Gaussian distribution to accurately calculate the absorption area ($1.971 \times 10^8 \text{ M}^{-1} \text{ cm}^2$), with energy of maximum absorption, $\nu = 24750 \text{ cm}^{-1}$. The fluorescence expectation value was calculated as described in the work by Strickler and Berg, $\langle \nu_f^{-3} \rangle = 7.59 \times 10^{12} \text{ cm}^{-1}$ and a refractive index of 1.5 is used for toluene (at 500 nm). The calculated k_r value for 1,2-OBTTT is 0.39 ns^{-1} , a value in good agreement with the measured k_r value (0.38 ns^{-1}). The Strickler-Berg relation can also be used to back calculate an absorptive area from a known k_r , then used to determine the oscillator strength, f_{nm} , of the S_0 - S_1 transition.

Sample	ϵ_{\max} (toluene)	Φ	τ_{PL} (ns)	k_r (ns^{-1})	$A(10^6 \text{ cm}^2 \text{ M}^{-1})$	f_{nm}
1,2-OBTTT	17430	0.16	0.43	0.38	191	0.83
2,2-OBTTT	17720	0.13	0.42	0.32	161	0.70
3,2-OBTTT	18450	0.14	0.41	0.33	166	0.72
4,2-OBTTT	19270	0.14	0.43	0.32	161	0.70
5,2-OBTTT	19270	0.16	0.42	0.38	186	0.80
6,2-OBTTT	18390	0.14	0.42	0.33	166	0.72
7,2-OBTTT	17320	0.12	0.41	0.29	146	0.63
8,2-OBTTT	16980	0.13	0.40	0.33	166	0.72
9,2-OBTTT	19370	0.14	0.42	0.33	166	0.72
10,2-OBTTT	19250	0.15	0.42	0.35	176	0.76

11,2-OBTTT	19550	0.13	0.42	0.32	161	0.70
12,2-OBTTT	17770	0.11	0.43	0.26	131	0.56
13,2-OBTTT	22650	0.13	0.42	0.32	161	0.70
Average	18720	0.14	0.42	0.33	164	0.71
Standard Dev.	1480	0.01	0.01	0.03	15	0.07

Table 5-1. Measured and calculated photophysical properties of the n,2-OBTTT series in toluene. Values show no variation between different molecules of varying tail length.

5.4 Electrochemical Determination of Frontier Orbital Energy Levels in n,2-OBTTT

Cyclic voltammetry (CV) measurements were executed for several of the n,2-OBTTT compounds to measure the reduction and oxidation potentials, E_{red} and E_{ox} respectively, and determine if there is any correlation between energy levels and tail length. In the OPV literature, electrochemically determined potentials are commonly compared and converted to orbital energy levels.⁸⁴ While these values are fundamentally related, solution electrochemistry is subject to an assortment of environmental properties that ultimately affect the measured potentials. Solvent, temperature, concentration, electrode choice, ramp rate, and, in particular, reference electrode choice can each have a significant influence over the measured potential. To account for these effects experimental conditions (including electrodes, analyte concentrations, and solvent) were all kept the same and ferrocene was used as an internal standard for each measurement. Although it is often considered a standard value, ferrocene is subject to solvent and other environmental effects, and a spread of reported values can be found in the literature.

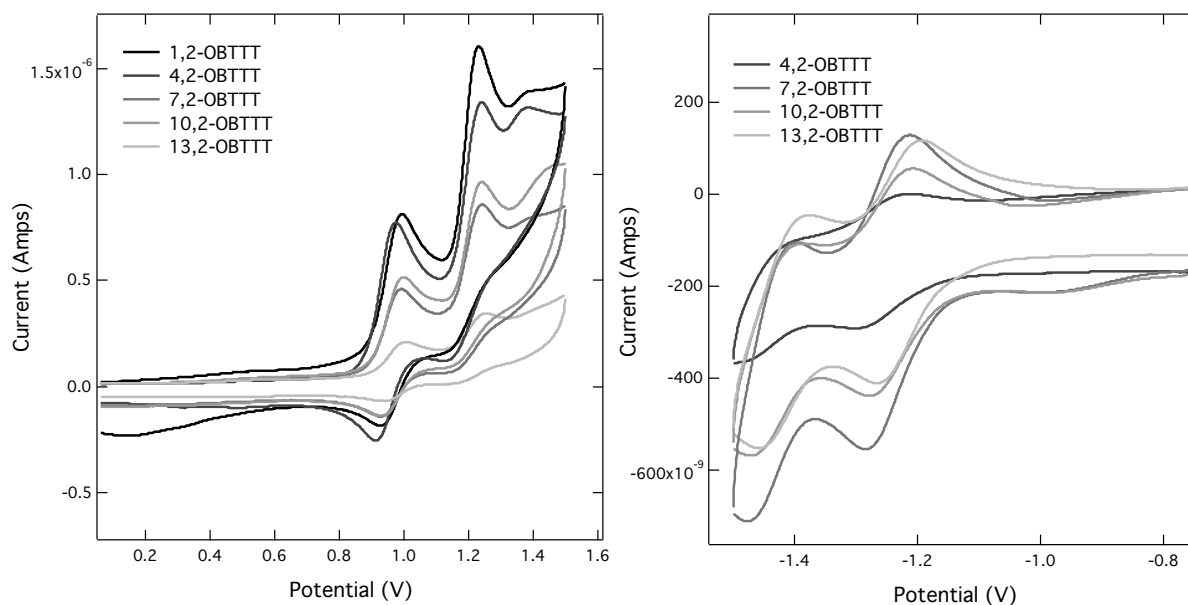


Figure 5-10. Voltammograms of $n,2\text{-OBTTT}$ $n = 1, 4, 7, 10, 13$, showing electrochemical reduction on the right and oxidation on the left. The oxidation and reduction potentials are calculated relative to the Fc^+/Fc peak, which is added to the sample as an internal reference. The average E_{red} is -1.75 V. The average first and second oxidation potentials are 0.46 V and 0.70 V.

The methoxy, butyloxy, heptyloxy, decyloxy and tridecyloxy ($n = 1, 4, 7, 10, 13$) were chosen as analytes to give both a spread of tail lengths and mix of even and odd tail lengths across the series. All samples showed several quasi-reversible peaks, one reduction and two oxidation (see Figure 5-10.) The peaks are deemed quasi-reversible as they differ from the ideal peak energy difference, $\Delta E_p = \frac{0.59}{n}$. Additionally, the cathodic and anodic currents are not equivalent. This may indicate that the ionic species is reacting in solution prior to reaching its corresponding reduction/oxidation potential.

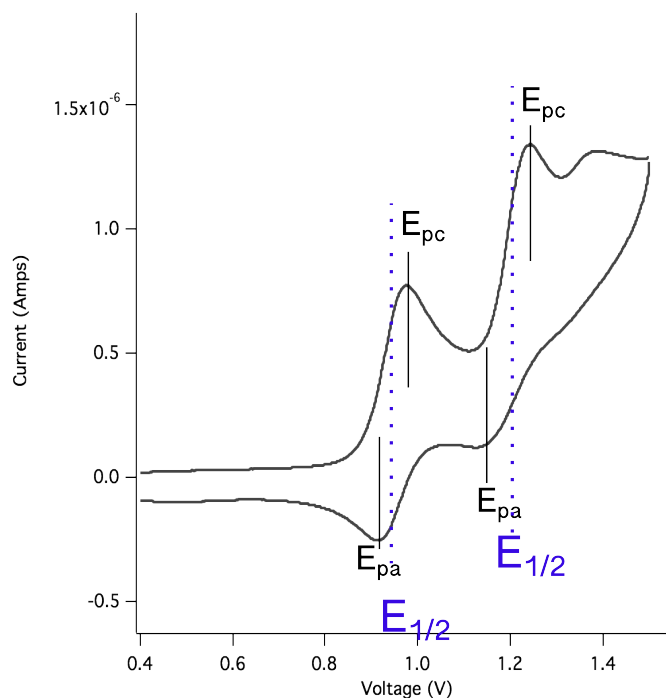


Figure 5-11. Oxidation voltammogram of 1,2-OBTTT demonstrating the cathodic and anodic peak energies indicated, E_{pc} and E_{pa} , along with the determination of $E_{1/2}$, dashed line. $E_{1/2}$ is used to determine the E_{red} and E_{ox} potentials.

The $E_{1/2}$ value was determined as the halfway point between the cathodic and anodic peak potentials, E_{pc} and E_{pa} , as shown in Figure 5-11. Two oxidation potentials and a single reduction potential were calculated relative to the ferrocene oxidation potential for each sample. A second reduction potential is also visible but was not explicitly measured.

Sample	E_{ox1} (V)	E_{ox2} (V)	E_{red} (V)
1,2-OBTTT	0.473	0.701	
4,2-OBTTT	0.451	0.696	-1.751
7,2-OBTTT	0.459	0.7	-1.754
10,2-OBTTT	0.458	0.687	-1.747
13,2-OBTTT	0.463	0.698	-1.743
Average	0.46	0.70	-1.75
Standard Dev.	0.01	0.01	0.01

Table 5-2. Calculated energies of first and second oxidation and reduction relative to Fc^+/Fc .

Samples were measured in a standard three-electrode setup, using a Teflon coated Pt working electrode, Ag/AgCl reference electrode, Ag counter electrode and with 0.1 M tetrabutylammonium hexafluorophosphate, $\text{Bu}_4\text{N}^+\text{PF}_6^-$, added as an electrolyte. A mixture of toluene and acetonitrile (5:3) was used as the solvent, allowing for the dissolution of the n,2-OBTTT analyte as well as the electrolyte and a sufficiently high dielectric for the electrochemistry. Voltage was changed at a ramp rate of 100 meVs^{-1} and ranged from 1.5 V to -1.5 V. Electrochemistry was measured in both polarities, potentials were unchanged by the direction of voltage ramp. Samples were degassed with N_2 for 5 minutes to minimize both reactions between oxygen and the sample as well as to reduce the signal from the reduction of oxygen. Despite these precautions the 1,2-OBTTT reduction potential was obscured by residual O_2 . After measurement of the solvent/sample/electrolyte a solution of ferrocene in degassed acetonitrile was injected into the solution cell and the experiment was repeated. By using ferrocene as an internal standard in each sample the measured potential can be compared directly to the Fc^+/Fc reaction.⁸⁵

The ferrocene oxidation potential as measured with Ag/AgCl reference electrodes has been measured as 5.1 eV by Cardona et al.⁸⁴ and is used to estimate ionization potential (IP) and electron affinity (EA) energies of these model compounds. Though it should be noted that IP and EA values are generally gas phase properties while the electrochemical measurements herein are solution measurements (and the estimated HOMO and LUMO levels described in chapter 6 are solid-state properties.) The average energies across the series are an EA of 3.4 eV and an IP of 5.6 eV. These levels are compared to prototypical OPV donors and acceptors in Figure 5-12.

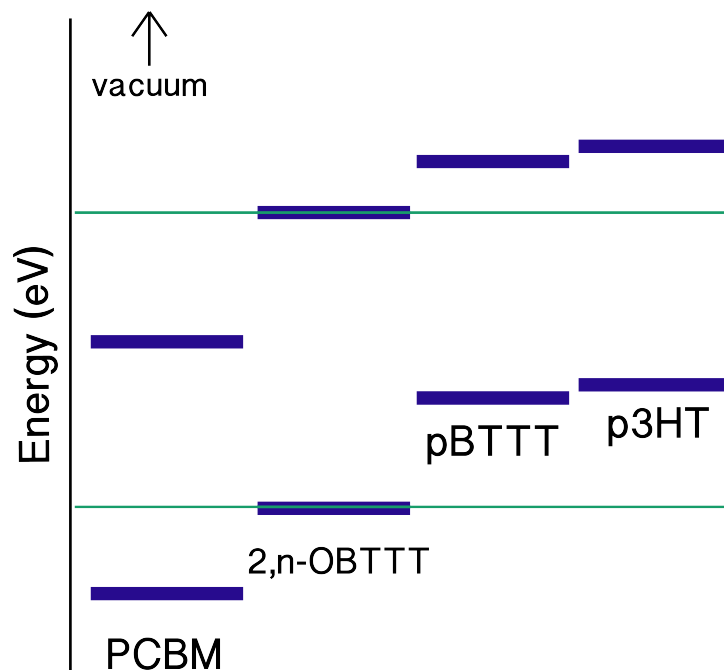


Figure 5-12. Relative HOMO and LUMO values for the n,2-OBTTT molecules and some common OPV electron donors and acceptors as measured electrochemically. The molecules studied herein fall into a range to exhibit favorable electron transfer to PCBM and also act as an electron acceptor with the conducting polymers, PBTTT and P3HT. The energy axis is left blank to indicate the general uncertainty in converting solution measured electrochemical energies to solid-state HOMO/LUMO values.

The average difference between E_{red} and E_{ox} across the n,2-OBTTT series is 2.2 eV. In the literature the optical bandgap, E_{gap} , is occasionally used to calculate E_{LUMO} level relative to E_{HOMO} , in which one level is electrochemically measured. Analogously, the E_{LUMO} of these materials would be overestimated by 800 meV if calculated from the optical bandgap of 3.02 eV. Even if the absorption band edge was considered (470 nm) it would lead to an optical gap of \sim 2.6 eV, 400meV larger than the measured $\Delta E_{\text{IP-EA}}$. Thus if a LUMO was calculated for these materials it would look like a type-I heterojunction offset with P3HT, but it will be demonstrated in chapter 6 that P3HT undergoes photoinduced charge transfer with 3,2-OBTTT, thus it is actually a type-II offset, as electrochemically measured herein. This is further confirmation that

electrochemically measured energy levels should not be commingled with optical energies in solid-state energy diagrams without considerable acknowledgment of the approximations.

The error associated with this technique is generally large, but with appropriate controls and internal standards it can be minimized yielding useful measured levels of reduction and oxidation potentials.

5.5 Conclusion

Property	Average Value
ϵ_{\max}	18720
Φ	0.14
τ_F (ns)	0.42
k_r (ns ⁻¹)	0.33
f_{nm}	0.71
E_{ox} (V)	0.46
E_{red} (V)	-1.75

Table 5-3. Average values measured in this chapter for n,2-OBTTT molecules. No systematic change was seen for molecules with different tail lengths.

Through various solution-phase photophysical and electrochemical experiments it is shown that the alkoxy tail length has negligible effect on the optical or electrochemical properties of the n,2-OBTTT model compounds. Average measured property values of n,2-OBTTT are reported in Table 5-3. Additionally, reduction and oxidation potentials fall into a favorable range to exhibit charge transfer with P3HT and PCBM, common electron donors and acceptors respectively. The final particularly interesting result is that the stability of the compounds in solution is shown to depend on the tail length. While the compounds in solution have identical properties, solid-state microstructure has previously been shown (chapter 4) to greatly influence optical and electronic properties. Chapter 6 will cover the microstructural effects on the photophysical and electronic properties of thin films of n,2-OBTTT.

Chapter VI: Solid-State Photophysics and Charge Transfer of n,2-OBTTT

Films

6.1 Overview of Experiments

This chapter chronicles the subtle differences tail length has on the solid-state properties of the n,2-OBTTT series, expanding on the solution characterization presented in chapter 5. As is presented in chapters 3 and 4, solid-state properties are affected by dopants as well as surface influences, herein it is shown that the solid-state properties are also influenced by the molecular tail length. Solid-state single crystal and thin film properties of n,2-OBTTT are reported along with the corresponding optical properties. A systematic, albeit subtle, change in the absorption edge wavelength combines with a similar shift in photoluminescence wavelength and is evidence that the n,2-OBTTT energy levels are changed slightly with increasing tail length. Postulations about the microstructural origins of this energy shift are included.

In chapter 5 solution electrochemical measurements showed that the n,2-OBTTT may be well-suited to undergo photoinduced charge transfer with PCBM. The absorption properties are shown to change systematically with tail-length so here TRMC is used to determine whether an analogous tail length trend is seen for photoinduced charge transfer in neat n,2-OBTTT, low wt% blends of PCBM in n,2-OBTTT and 50/50 mixtures. Additionally solution measurements predict that n,2-OBTTT may act as an electron acceptor with the prototypical OPV polymer, P3HT. TRMC is again used to determine photoinduced charge transfer in the donor-acceptor blends. Finally, it is shown that the addition of n,2-OBTTT increases the yield-mobility product in blends of P3HT/PCBM, and may be acting as a high energy sensitizer.

6.2 Bulk n,2-OBTTT Properties and Single Crystal Studies

The solid phase properties of n,2-OBTTT differ from that of the solution, characterized in chapter 5. Each of the n,2-OBTTT molecules contain high temperature liquid crystal smectic phases. All samples reported herein are studied at room temperature but the liquid crystal morphology has control over the resulting low temperature sample microstructure. Thus it is relevant to mention that the lowest temperature phase of these liquid crystals is the Smectic E (SmE) phase. This phase has recently received attention for its connection to mesogens with very high carrier mobility crystal phases. The SmE phase is a highly ordered, low temperature smectic phase, in which the mesogens are packed in a herringbone fashion within the smectic layers. As with other smectic phases, the SmE phase is made from calamitic (elongated) mesogens with a single or double tail.

Single crystals were grown for single crystal x-ray diffraction (the crystals were grown by Mike Springer and measured at Johns Hopkins X-Ray Facility.) Only samples of 1,2-OBTTT, 3,2-OBTTT and 9,2-OBTTT were measured, though empirically the rest of the series with the exclusion of 1,2-OBTTT formed similar crystals when grown from solution. These single crystal results are further described in work currently in preparation for publication.

Select crystal properties remain unchanged between the three different tailed mesogens measured (methoxy, propoxy and nonyloxy.) In all three tail lengths of the n,2-OBTTT crystals the thiophene and thienothiophene rings orient so that the sulfur in the ring is in alternating directions, akin to that measured in the PBTTT polymeric crystal structure. Crystal structures also show that the rings in the BTTT chromophore are coplanar (flat). The 3,2-OBTTT crystal is symmetric at C10 (center bond of the thienothiophene unit) and the torsion angle is

179°, while the 9,2-OBTTT is asymmetric but the angle for each thiophene and thienothiophene is 175°. The thiophene rings all orient in a single plane so the electron orbitals delocalize across the chromophore and roughly fulfill Hückel's rules of aromaticity. Finally, both molecules pack with a herringbone structure between adjacent molecules.

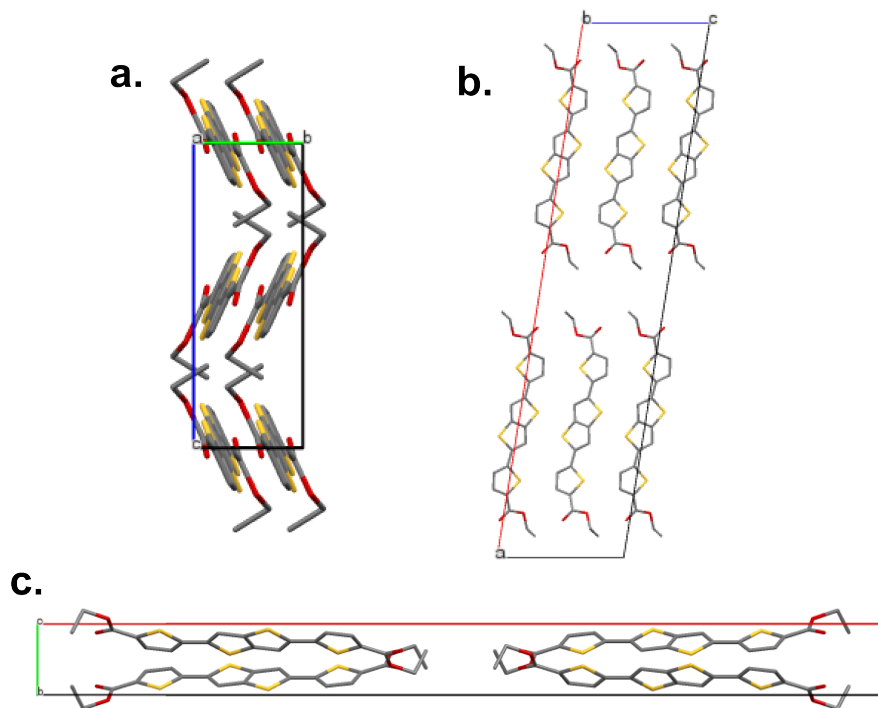


Figure 6-1. Unit cell axes of the 3,2-OBTTT crystal structure, letters correspond to viewing the crystal down the axes, a) shows the general herringbone packing in the crystal, b) and c) elucidate the layers formed in the crystal.

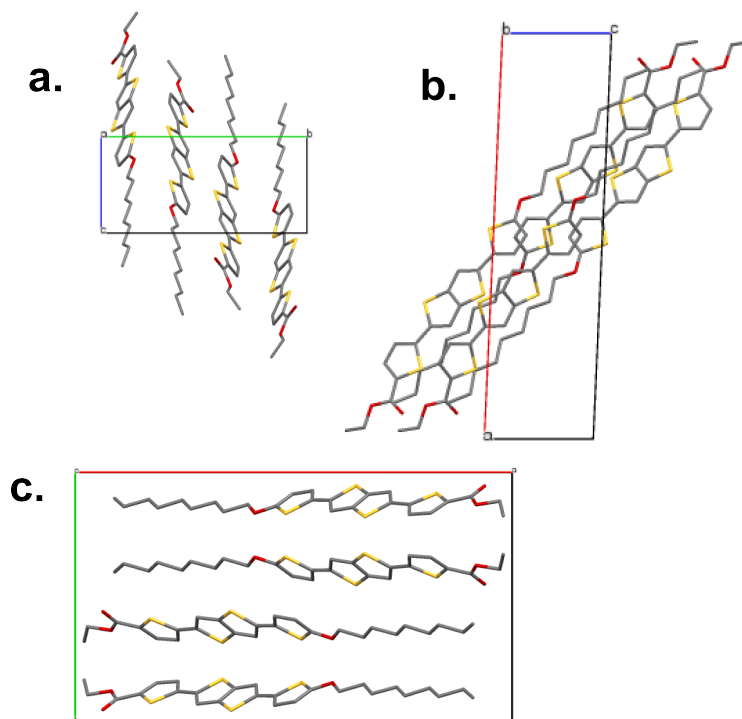


Figure 6-2. Unit cell axes of the 9,2-OBTTT crystal structure, letters correspond to viewing the crystal down the axes, a) and b) shows the general herringbone packing in the crystal, and b) and c) elucidate the presence of sheets of alternate tail-direction. The slipped chromophores in these sheets are proposed to lead to specific absorption trends.

Several differences in the crystal properties are exhibited between the propyloxy and nonyloxy crystal structures. (It should be noted that the methyloxy differs quite substantially across all measured properties and thus it has been omitted from this chapter.) The 3,2-OBTTT crystal structure shows no differentiation between the propyloxy and ethanoate tails, thus the structure appears averaged over both tails signifying that the orientation of molecular packing is indiscriminant of tail type. This is not the case for the nonyloxy homologue. The 9,2-OBTTT crystals show a distinct difference between the nonyloxy and ethanoate tail, Figure 6-2C. Another difference between the crystals is the degree of intermolecular chromophore overlap. The chromophores in 3,2-OBTTT directly overlap with the chromophore of adjacent molecules in two dimensions, Figure 6-1B and C, forming layers of interacting chromophores. In contrast to this, the BTTT unit on 9,2-OBTTT is in the same plane in one direction but as shown above

the molecule direction is flipped in the c axes direction, Figure 6-2C. This is difficult to visualize from the unit cell so an expanded crystal structure is shown in Figure 6-3. This creates alternating layers of chromophore pairs. This will become particularly important in the following sections on the absorptive properties of the molecules.

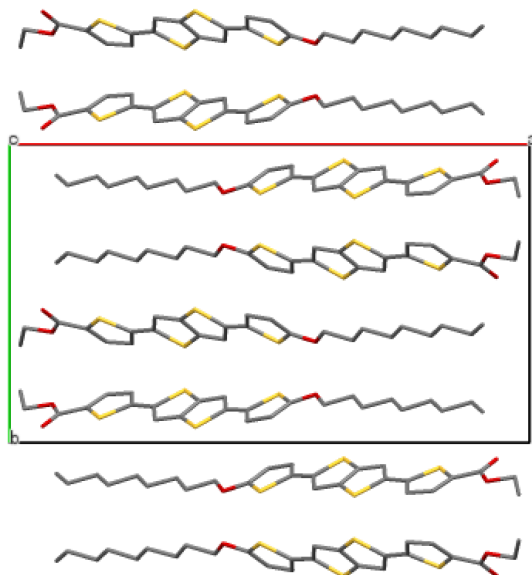


Figure 6-3. Expanded unit cell along the c axis of 9,2-OBTTT demonstrates the alternating direction of pairs of 9,2-OBTTT molecules. Molecules are all tilted into the plane.

The different tail length molecules tilt to differing extents; 3,2-OBTTT is nearly untilted but, as is seen in Figure 6-2B, 9,2-OBTTT is titled $\sim 45^\circ$. This is relevant to the powder diffraction measured in thin films and will be readdressed in a following section. The total molecular length for the molecule is measured to be 21.0 Å for 1,2-OBTTT and 31.1 Å for 9,1-OBTTT, while just the BTTT chromophore is 15.8 Å.

Two main features need to be emphasized from these realized structures 1) that the BTTT units are packing in layers of molecules and are places within the layer in a herringbone structure and 2) that the slipping of molecules in the 9,2-OBTTT crystal structure is leading to biaxial

chromophore overlap. The former point is relevant to both optical absorption and charge carrier mobility. The layers of OBTTT will lead to alignment of the transition dipoles and thus contribute to an H-aggregate character in the absorption. The π - π overlap between adjacent molecules may be useful for charge transport between molecules, as this typically is dependent on molecular orbital overlap. The second point to be made from the crystal data is that the slipping of molecular layers, as seen in Figure 6-3, leads to slipped orientation of the transition dipoles (possibly less H-aggregate character) and possibly a difference in the carrier mobility (orbitals are overlapping less in the b direction than the c).

Without crystal structures for the remaining mesogens two assumptions can be made about the molecular crystals from the two solved structures. The first assumption is that the thiophenes in the chromophore are oriented in a single plane (as opposed to exhibiting a twist between thiophene rings.) The second is that sulfur direction in the thiophene rings is alternating between rings on the same molecule. Optical properties will be used to further characterize the n,2-OBTTT intermolecular packing.

6.3 Thin films of n,2-OBTTT

In chapter 3 the P-9-OPIMB thin film structure was shown to diverge from that of the bulk, similarly thin films of n,2-OBTTT differ from the measured single crystal structures. Powder diffraction is used here to quantify the difference between the bulk measured by single crystal x-ray and the thin films formed by spincoating and annealing (to 200°C). Unfortunately, the highly detailed structural information presented in the single crystal studies is not accessible by powder diffraction, which limits analysis to only layer spacing and peak width as in the HNF studies of chapter 3.

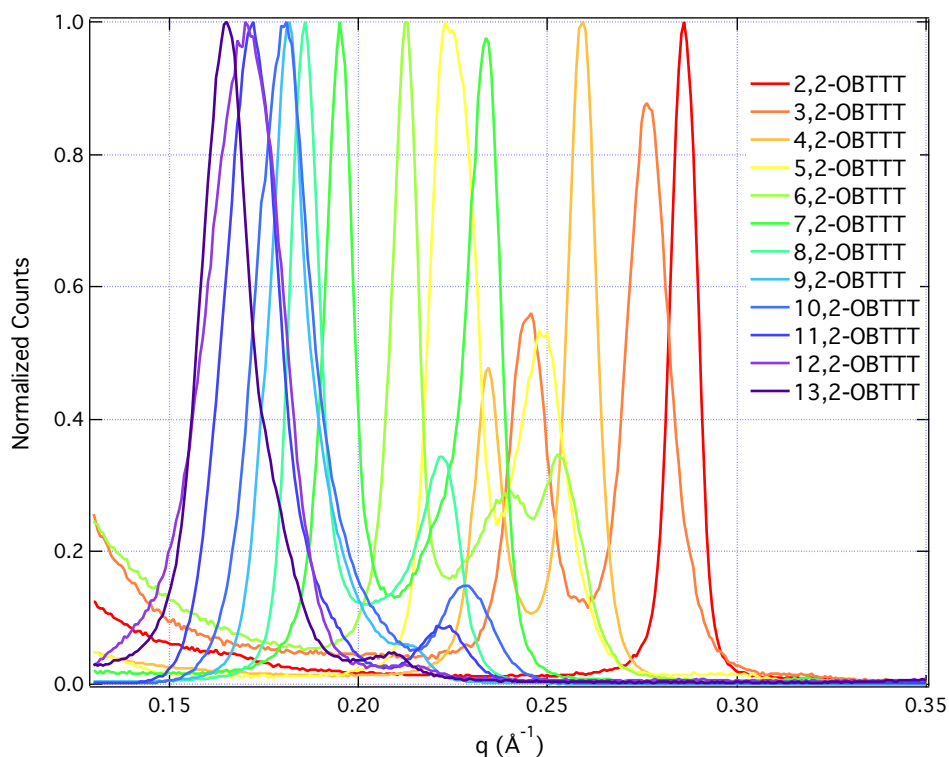


Figure 6-4. Diffraction of annealed $n,2$ -OBTTT thin films on quartz. Diffraction spacing, q , is highly dependent on the tail length and consequently shows the layer spacing is increasing with tail length.

X-ray diffraction for thin films in the series is shown in Figure 6-4. The color-coded molecules, ranging from red to blue with increasing tail length, easily show the increasing layer spacing trend of the molecules. As would be expected, the shortest tailed molecules have the smallest layer spacing (largest reciprocal spacing, q) and the longest tail lengths show the largest layer spacing. Each molecule also demonstrates multiple low angle peaks, similar to the data reported in chapter 3, the wide angle diffraction is obscured by the samples substrate. The presence of multiple low angle peaks may be due to multiple crystal polymorphs in the samples or the presence of multiple preferential crystal orientations on the substrate surface. The measured samples have been thermally annealed which lessens the likelihood of multiple polymorphs.

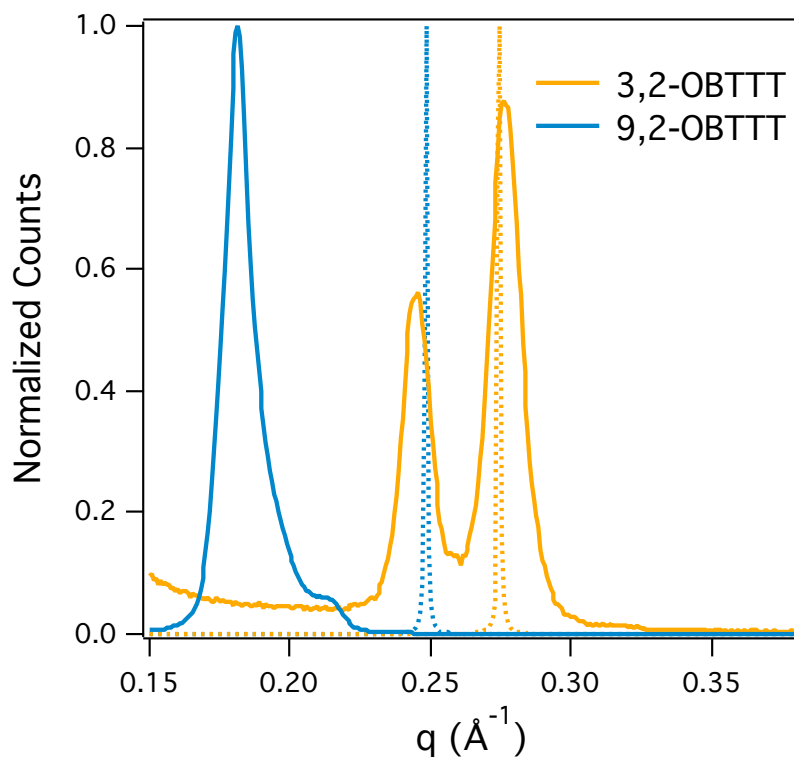


Figure 6-5. Calculated powder pattern made in Mercury from the measured single crystal data (dashed line) and measured thin film (solid line). The calculated powder peak location varies substantially from the thin film XRD. In the case of the shorter-tailed homologue, the larger q peak matches closely with the calculated diffraction pattern, indicating a similar packing geometry to the single crystal. In the longer tail homologue the diffraction spacing differs substantially, the calculated peak at $q = 2.5 \text{ \AA}^{-1}$ is from a smaller layer spacing than either of the measured diffraction peaks.

A comparison of the calculated powder pattern and measured XRD of the thin films of 3,2-OBTTT and 9,2-OBTTT is shown in Figure 6-5. The calculated powder patterns vary substantially from the thin film XRD peaks both in peak location and width (the latter due mainly to instrument broadening.) In the case of the shorter-tailed homologue, the larger q peak matches closely with the calculated diffraction pattern, indicating a similar packing geometry to the single crystal. In the longer tail homologue the diffraction spacing differs substantially, the calculated peak at $q = 2.5 \text{ \AA}^{-1}$ is from a smaller layer spacing than either of the measured diffraction peaks.

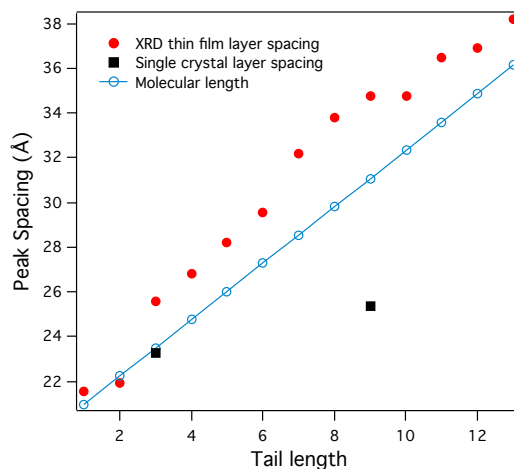


Figure 6-6. Measured powder X-ray diffraction spacing from thin films (red circles) is compared to the calculated powder diffraction (black squares) and the extended molecular length (blue open circles.) The measured thin film diffraction shows layer spacing just larger than that of the molecular length, indicating that the molecules exist in untilted layers of molecules.

Molecular lengths of *n*,2-OBTTT were determined by measuring along the length of the 9,2-OBTTT and 1,2-OBTTT crystal structures (distance between the terminal hydrogen atoms), calculating the contribution to length by added methylene linkers in the tail and then figuring the length for alternate molecular lengths (each $-\text{CH}_2$ group added 1.265 \AA to the molecular length.) The molecular lengths range from 20.961 \AA to 36.135 \AA across the series, and are compared to the measured powder XRD spacing from the measured thin films in Figure 6-6. The computed single crystal powder diffraction is smaller than the molecular length indicating a tilted layer structure, which is also observed in the realized crystal structure. But peaks from the measured thin film samples actually showed layer spacing just larger than the molecular length, indicating a lack of molecular tilt in the layers of the thin film samples.

Though the layer spacing is shown to differ between the single crystals and the thin films, the intramolecular packing is inconclusively changed, and possibly retains the alternating dimer packing directions seen in the 9,2-OBTTT single crystal sample. Due to the lack of

intramolecular data in the powder diffraction data this cannot be used to determine π - π spacing necessitating further analysis to determine the intralayer structuring of the molecules.

6.4 Solid-State Photophysics of n,2-OBTTT Thin Films

Solid-state absorption can differ significantly from the isolated molecule, solution-phase absorption.²⁰ Just as the solution phase measurement differs from gas photophysical properties because of intermolecular interactions between analyte and solvent, state-state absorption differs due to intermolecular interaction between adjacent molecules.¹⁶ As described in chapter 1, molecular dimers may have S_0 - S_1 absorption energies shifted to a higher or lower energy relative to the single molecule property. The direction and extent of the energy shift is dependent on the orientation of the transition dipoles relative to one another.¹⁶ Generally speaking, a parallel alignment of dipoles leads to a higher energy absorption, H-aggregate, whereas an end-to-end alignment leads to an energy lowering, J-aggregate, as shown in Figure 6-7. As the orientation of the chromophores differ between these two geometries both energy levels become “allowed” and contribute to the absorption profile. In the case of larger aggregates and crystallites the energy shift is increasingly complicated; contributions from both H- and J-aggregation may coexist leading to split energy levels with optically allowable transitions to the both energies,⁸⁶ as described in detail in chapter 1.

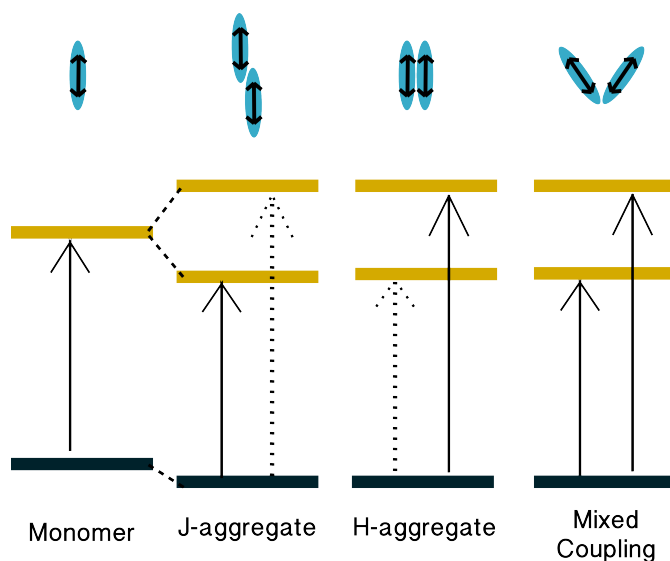


Figure 6-7. Simplified examples of chromophore interaction effects on molecular absorption, solid and dashed lines represent allowed and forbidden transitions respectively. The blue oval represents the chromophore in which the black arrow is the absorption transition dipole. Parallel orientation of the dipoles leads to an allowed transition to higher energy. Slipped dipole alignment, J-aggregate, leads to a lower energy absorption. In more complicated (and common) crystal orientations both transitions are allowable to varying degrees.

6.4.1 Solid-State Absorption

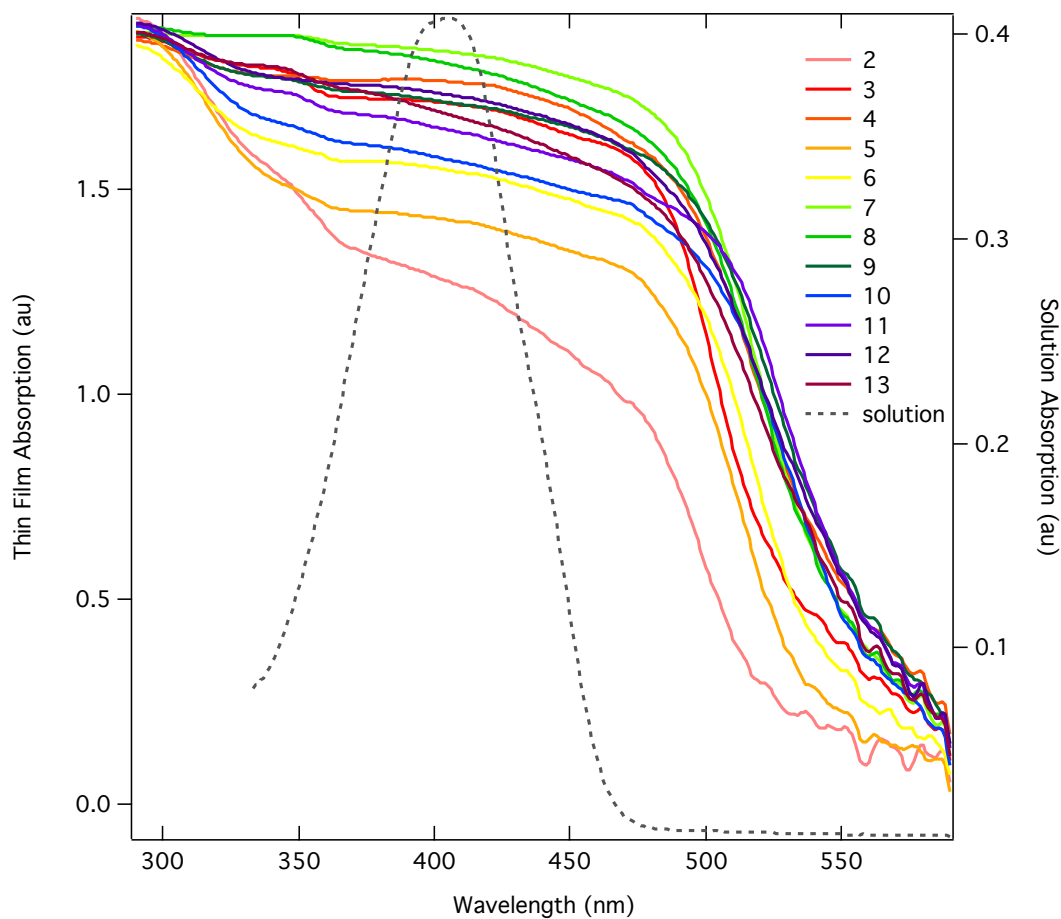


Figure 6-8. Thin film absorption for dropcast films of the n,2-OBTTT series between glass slides annealed to 200 °C. A peak is seen at about 340 nm with a shoulder extending out to ~ 550 nm. The solution absorption is also shown for comparison. The film thickness varies some between different samples, but notably the 2,2-OBTTT shows a less intense low-energy shoulder and the absorption edge ~550 increases with increasing tail length.

Figure 6-8 shows the absorption across the n,2-OBTTT series in annealed dropcast films. The films' absorbance lacks definition but several features are immediately evident. The film absorption edge, around 550 nm, is significantly red-shifted relative to the absorption edge of 2,2-OBTTT in toluene, 470 nm. The solid-state spectral shift from the monomer is larger than that would originate from solely the solid-state absorption broadening.⁸⁷ The absorption is still

significantly higher in energy than the polymeric absorption edge at 660 nm ($\lambda_{\text{max}} = 540$ nm.) Another peak is observed in the samples at 340 nm, a peak blue-shifted relative to the solution absorption. Below ~ 290 nm the optical density of the film obscures structural absorption resolution. The absorption of 1,2-OBTTT substantially differs from the rest of the n,2-OBTTT series, with a single peak at 260 nm and a broad shoulder to the absorption edge and will be otherwise omitted from this thin film study.

As mentioned earlier, interactions between adjacent chromophores can lead to the splitting of S_1 energy levels and consequent absorption into higher or lower energy transitions depending on the relative orientation of dipoles between neighboring chromophore. The presence of the higher (340 nm) and lower energy (490 nm) transitions in the n,2-OBTTT films relative to the monomer (solution) absorption is clear though the origins of these transitions is unknown, here a conjecture is made about the origins of these transitions. The relative location to the monomer absorption, indicated that both the 340 nm and 490 nm absorptions are originating from split S_0 - S_1 transitions (and not higher singlet levels.) The terms H-like and J-like will be used to refer to the higher and lower energy absorptions (the absorption near 340 nm is H-like and the broad absorption shoulder at 500 nm is J-like, although traditional J-aggregates show a sharp absorption.) On first glance, the relative magnitudes of the H-like and J-like transition magnitudes appear to vary across the series though quantification of this difference through the ratio of H- and J-like transitions as determined from the peak 340 and 450 nm peak magnitudes shows that the ratio is remarkably unchanged across the series Figure 6-9. Though 2,2-OBTTT has anomalously high level of H-character.

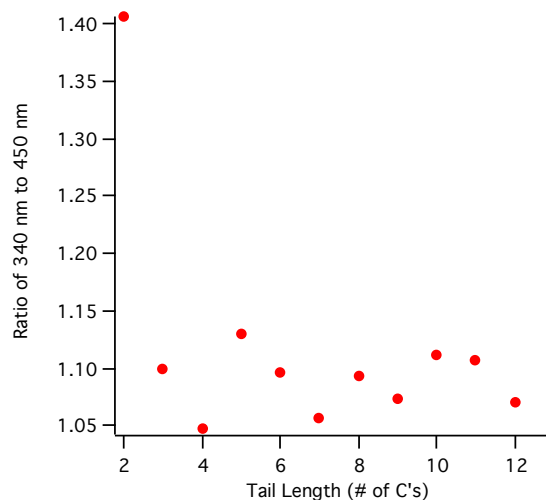


Figure 6-9. Ratio of the peak magnitudes of the H- and J-like absorption features, 340 and 450 nm respectively shows a lack of tail length trend, although again 2,2-OBTTT is anomalous. The ratio is also used to account for differences in film thickness.

The magnitude of the two transitions is shown to be unchanged across the series. Yet there are measurable differences in the absorption spectra of the n,2-OBTTT series, Figure 6-8. In the H-like peak the absorption wavelength is 340 nm for all tail lengths. This indicates that the energy of transition (originating from dipole-dipole alignment, as shown in Figure 6-7) is unchanged and thus the dipole-dipole spacing is also unchanged for different n,2-OBTTT tails. Recall that both crystal structures reported in section 6.2.2 showed alignment of the chromophores (Figures 6-1A and 6-2C) and also that alignment of transition dipoles causes an optically active higher energy transition. Thus the packing demonstrated in the single crystal studies is one possible origin for the 340 nm absorption.

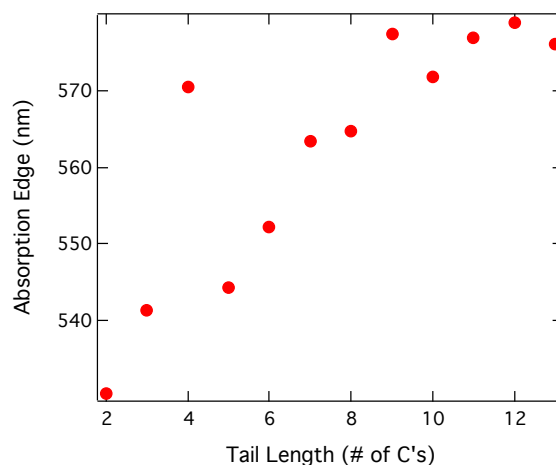


Figure 6-10. The absorption edge, determined from a fit to the absorption edge, of the lower energy “J-like” transition is plotted against tail length. The absorption edge is determined by fitting a line to the steep shoulder and extracting this value to the baseline. The absorption edge shifts to a lower energy as tail length increases. This indicates that there is a systematic effect of tail length on the intermolecular packing.

Figure 6-10 shows a nearly linear relationship between absorption edge and tail length of the n,2-OBTTT films. Though the higher energy is unchanged for different tail lengths, the lower energy (~490 nm) absorption varies with increasing tail length. A definite trend exists between the tail length and absorption edge, specifically the absorption edge is shifting to a lower energy for increased tail length. This indicates that there is a systematic effect of tail length on the intermolecular packing.

The purpose of this study is to quantify the effect of tail length on the photophysical properties. The film thicknesses vary somewhat across the series and thus the exact effect of tail length on the absorption is complicated, photoluminescence data in the following section will further elucidate the variation across the series.

6.4.2 Solid-State Film Photoluminescence

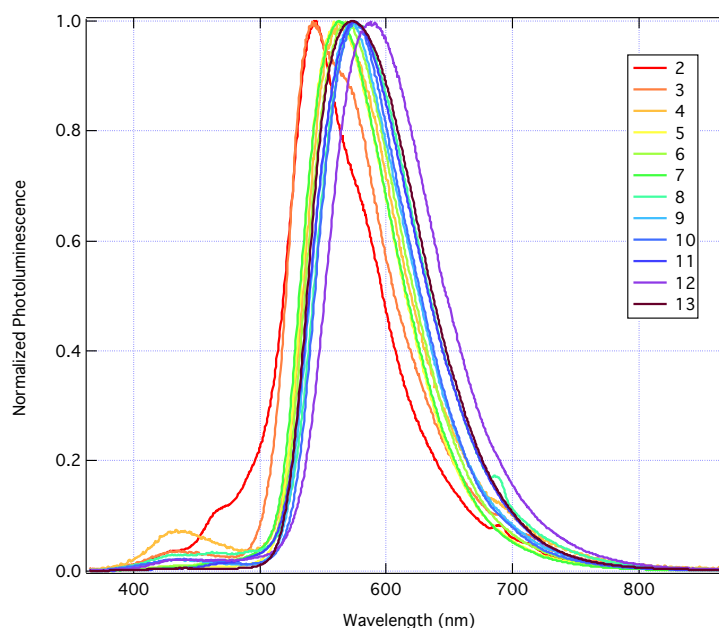


Figure 6-11. Thin film photoluminescence shown for the n,2-OBTTT, with $n = 2 - 13$, series excited at 355 nm. For all films measured two peaks were observed, a peak at 420 nm from a weak emission and a much more intense peak at ~ 550 nm. The peak location of the higher energy peak (420 nm) remained constant for different tail lengths while the lower energy (~ 550 nm) peak shifts to longer wavelengths (lower energy) with increasing tail length.

Two peaks are prominent in the annealed thin film photoluminescence shown in Figure 6-11, a minor peak at ~ 420 nm and a larger, lower energy peak which varies with tail length, ~ 570 nm. Interestingly, the photoluminescence peak shifts with increasing tail length, ultimately varying the emission wavelength from 543 nm to 588 nm, a total energetic difference of 175 meV. In thinner, spin-cast samples of the n,2-OBTTT it is apparent that thinner films showed more of the 420 nm emission. In the case of the higher energy emission (420 nm) it is likely due to its similar higher energy absorption (340 nm), originating from H-aggregation. H-type aggregates are known to have a low emissivity, due to the internal conversion to the lower lying

energy state. Thus the weakness of the 420 nm emission peak is congruent with the observation that the 340 nm absorption is a H-type aggregation.

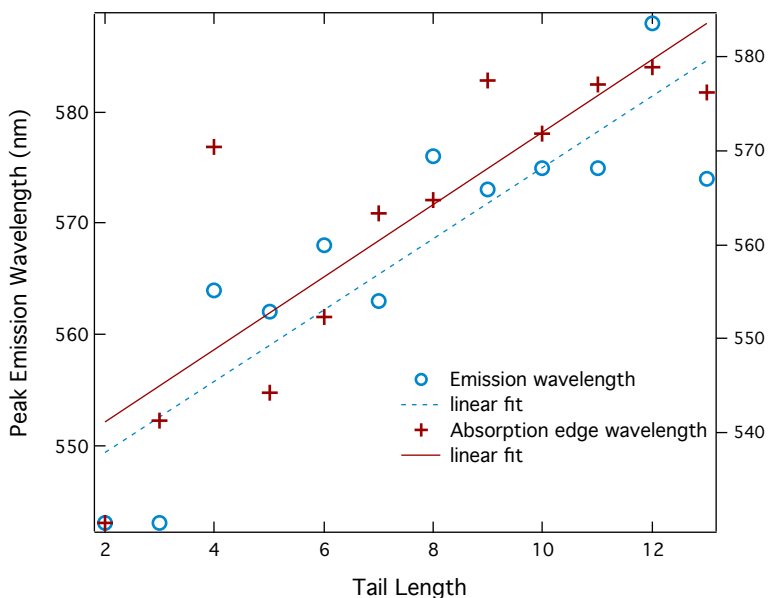


Figure 6-12. Peak emission wavelength (blue circles) and absorption edge wavelength (red crosses) plotted versus the tail length of the n,2-OBTBT mesogens. Both features follow the trend that increasing tail length leads to lower energy features. The absorption shoulder can be used to account for the change in emission wavelength for different tail lengths.

The lower energy peak emission, ~560 nm, changes with tail length. Figure 6-12 shows that the photoluminescence wavelength increases across the series from 2 – 13 carbon tails, demonstrating an emission shift to lower energy with increasing tail length. This systematic change possibly manifests from a shift in coupling between adjacent chromophores, and is also shown in the absorption edge. An illustration of the resulting spectroscopic features and proposed energy transitions is shown in Figure 6-13.

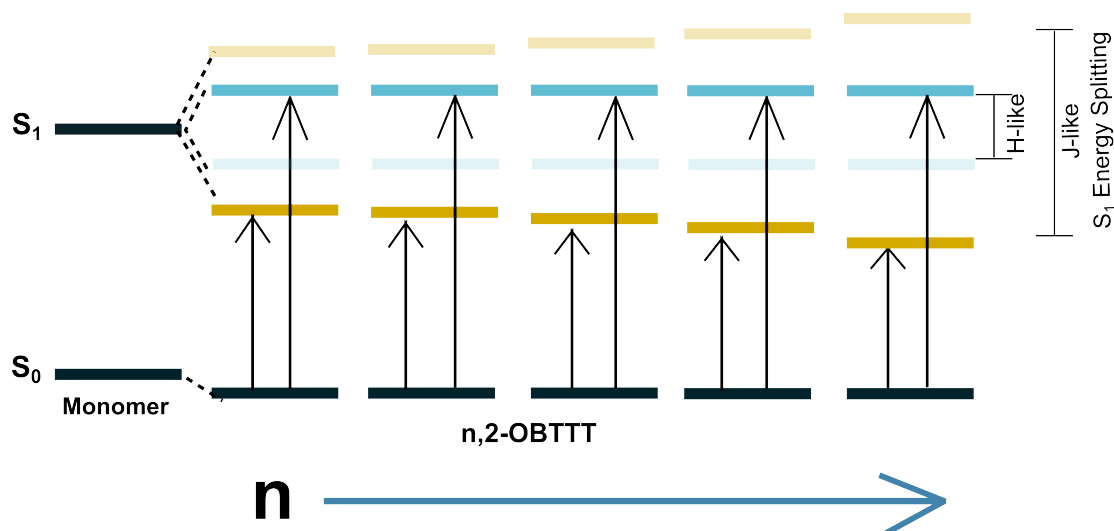


Figure 6-13. Schematic summarizing the absorption trends from the H-like and J-like split S_1 energy levels are shown for different tail lengths. The dark blue and orange levels indicated the optically active level of the transition, while the semitransparent bars indicate the inactive transition. The H-like transition, blue bar, originates from parallel dipole alignment and is unchanged with tail length. The J-like energy level, orange, is shown to decrease in energy with increasing tail length.

The existence of the lower energy (J-like) transition in the thin films is apparent though the origin of this transition can only be speculated. Recall from the single crystal structures that 9,2-OBTTT crystals contain planes of alternating tail directions in the b axis direction, as shown in Figure 6-2. At the interfaces of these planes, the transition dipoles would be oriented in a traditional J-aggregation (slipped) positioning (see Figure 6-7.) This could account of the J-like absorption and emission seen in the present work. Though in the 3,2-OBTTT no such slipping of the chromophores is seen, which leaves the source of the J-like aggregation in 3,2-OBTTT unknown. It is also important to distinguish that the thin films were shown with XRD to differ from the single crystal diffraction studies, and that the layer spacing as measured with powder XRD was shown to increase linearly with tail length (shown in Figure 6-6). If the alternating tail-directions of 9,2-OBTTT are the origin of the J-like transition then the degree of the splitting (larger split energy level leads to lower energy transition) may be increasing with tail length, see

Figure 6-14. Thus the structural-photophysical trend exists but the physical origin of the trend is only speculated. Future work will elucidate the source of the energetic splitting in n,2-OBTTT films.

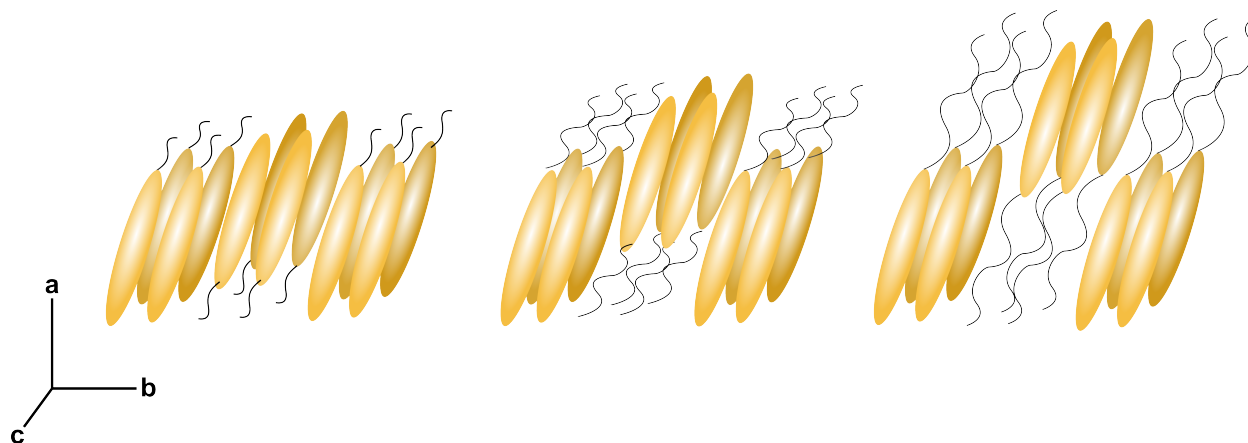


Figure 6-14. Proposed scheme for the source of H- and J-like spectral features using cartoon molecules, the orange oval represents the chromophore and the line represents an alkoxy tail. The dipole alignment of the chromophore in the b and c directions leads to the H-like absorption (which was observed to **not** vary with tail length.) Whereas the slipped orientation of the dipoles is leading to the J-like absorption, the varying degree of slipped leads to the different total splitting in the energy level (the longest tails have the most-slipped dipoles and thus the lowest energy transition.)

6.4.3 Selective Emission From H-like and J-like Absorption

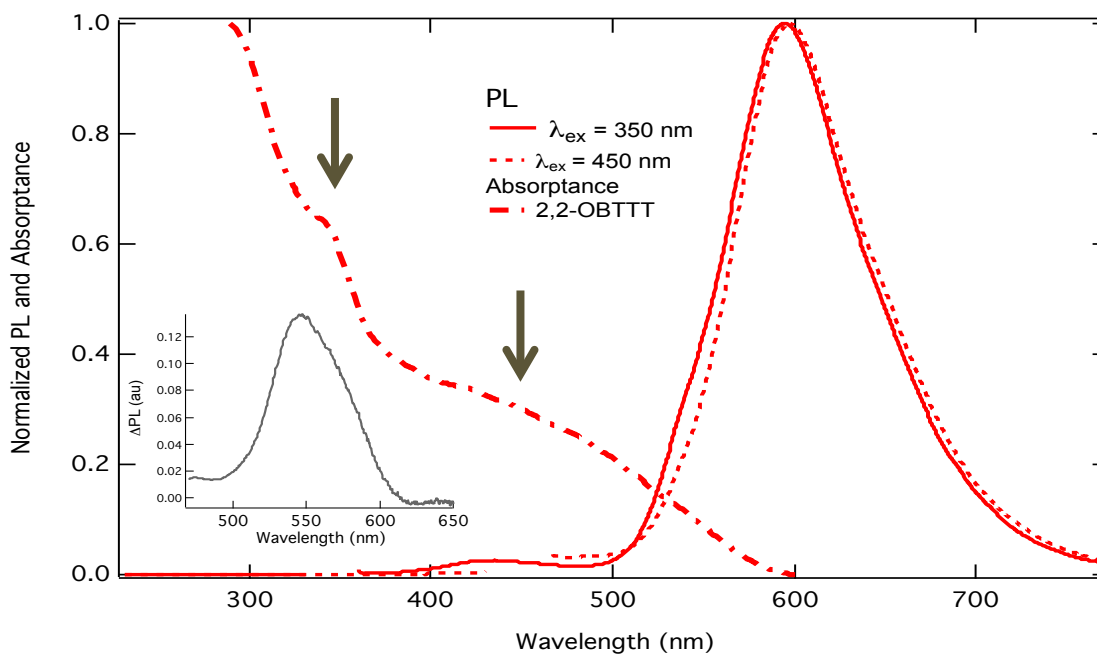


Figure 6-15. Photoemission is shown from two different excitation wavelengths in a sample of as-cast 2,2-OBTBT, 350 nm and 450 nm, indicated with arrows. The inset graph depicts the difference between the two PL emissions demonstrating a peak at 550 nm, which originates solely from the 350 nm absorption.

Figure 6-13 demonstrates the different emissivity from excitation at H-like ($\lambda_H = 350$ nm) and J-like ($\lambda_J = 450$ nm) wavelength in an as-cast sample of 2,2-OBTBT. The λ_H excitation is able to excite both energy levels whereas the λ_J only excited the lower energy absorption peak. Emission from λ_H shows a slightly blue shifted emission of the most prominent peak, 590 nm, in addition to the peak at about 420 nm. The peak shift is due to a second emission present at 530 nm, leading to an apparent peak shift from 597 nm to 594 nm, a difference of 10 meV. This emission is further resolved by subtracting λ_J emission from λ_H emission (inset Figure 6-13.) The presence of a second lower energy emission from λ_H is possibly due to a relaxation and emission from the lower (forbidden) energy level.

6.5 Photoconductivity Studies of n,2-OBTTT

In chapter 5 the n,2-OBTTT molecules in solution were shown to be isoenergetic, yet certain spectral properties of the films vary moderately as a function of tail length in the series. It is of interest to study whether the minor changes in absorption at various tail lengths will have an effect on charge generation. Thus similar to the HNF studies of chapter 4, the charge transfer of n,2-OBTTT is studied here with the microwave conductivity technique. TRMC is used to characterize the neat films, n,2-OBTTT as an electron donor and electron acceptor. Additionally, as mentioned in chapter 5, these molecules were designed as arm units for novel HNF-forming mesogens, which will ultimately be studied for photoinduced charge generation properties. Quantifying the photoinduced charge transfer properties of n,2-OBTTT with electron donors and acceptors in the solid-state will be useful to the future characterization studies of the n,2-OBTTT-containing HNF mesogens.

6.5.1 Microwave Mobility Contribution of n,2-OBTTT

TRMC photoconductivity of the neat molecules is used as a gauge of the microwave carrier mobility of the n,2-OBTTT across the series and the yield-mobility product is determined as described in chapters 2 and 4. The yield of charges in these neat samples is unknown but has no reason to systematically vary with tail length towards more or less photogenerated charges. This can be considered a rough estimate of the microwave contribution because the measurement is dependent on relative yield of photogenerated charges.

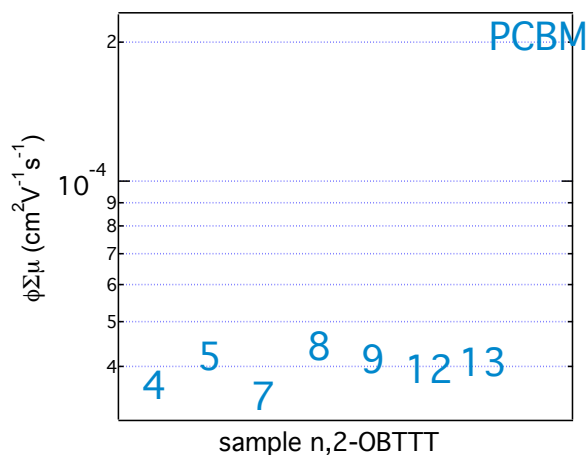


Figure 6-16. A maximum yield-mobility product for samples of neat n,2-OBTTT excited at 430 nm (2×10^{13} photon/cm²) is plotted for several films demonstrating the lack of variation in yield-mobility between tail lengths. This is used to demonstrate that the microwave carrier mobility of n,2-OBTTT is constant between different tail lengths.

Figure 6-16 shows the peak yield-mobility product at a relatively low light intensity (2×10^{13} photons/cm²) for select films of n,2-OBTTT, n = 4, 5, 7, 8, 9, 12, 13, along with a film of neat PCBM for reference. A variety of tail lengths with odd and even tail lengths are included to measure tail length dependent and parity dependent mobility properties. Photogenerated charges had a fast and slow decay component, as demonstrated in the transients of 9,2-OBTTT, Figure 6-17, indicating two types of charges being generated in the films 1) those which rapidly trap or recombine and 2) those that are able to move away from the charge generation interface.

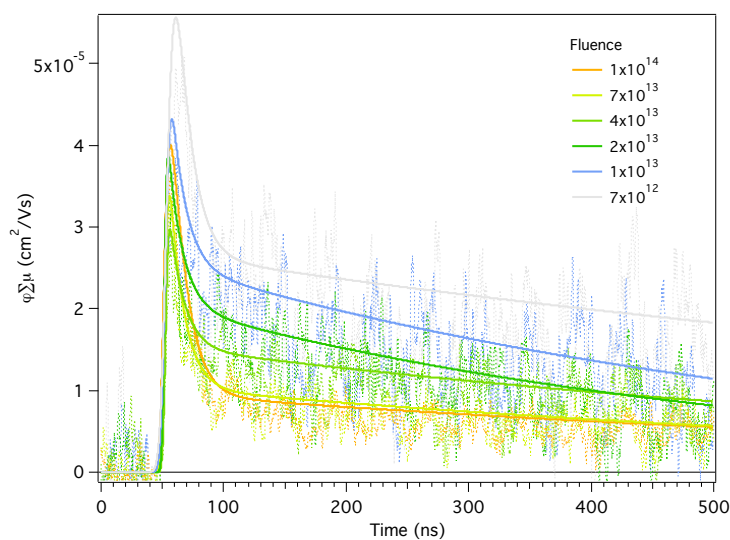


Figure 6-17. Yield-mobility product transients of a neat 9,2-OBTTT film excited at 420 nm with different light intensities. A fast and slow decay component is observed for generated charges.

No trend between tail length and yield-mobility product were observed in these samples. If the yield is constant for different tail lengths then the carrier mobility of different n,2-OBTTT materials is unchanged. If the yield is changing with tail length then the mobility is also changing perfectly inversely so that the yield-mobility product remains the same for different tail lengths. The latter case is quite unlikely and thus I am proposing that the mobility is unchanged between samples with different tail lengths.

The distinct molecular crystal structures between the 3,2-OBTTT and 9,2-OBTTT molecules, see Figures 6-1C and 6-2C and 6-14 makes this result unexpected. Though chromophore alignment, which leads to the H-like aggregation described above, would allow orbital overlap in two directions for all molecule tail lengths. A lower limit sum of charge carrier mobilities for the n,2-OBTTT films (as determined from $\phi = 100\%$) is $5 \times 10^{-5} \text{ cm}^2 \text{V}^{-1} \text{s}^{-1}$. If a more reasonable yield of charges is assumed for the n,2-OBTTT molecules (1%) the sum of charge mobilities in these neat materials is $5 \times 10^{-3} \text{ cm}^2 \text{V}^{-1} \text{s}^{-1}$. This is a gigahertz microwave

mobility and is not comparable to a bulk carrier mobility measurement such as thin-film transistor or time-of-flight conductivity because it probes local mobility within crystallite grains without being constrained by grain boundaries.

6.5.2 n,2-OBTTT as an Electron Donor

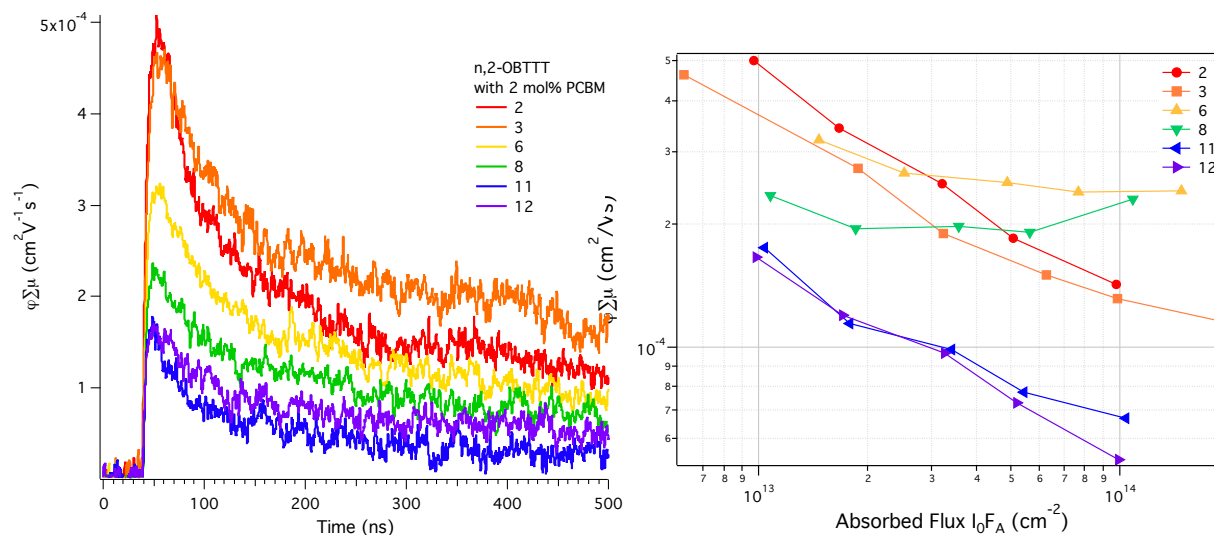


Figure 6-18. Photoconductance transients of n,2-OBTTT ($n = 2, 3, 6, 8, 11, 12$) with 2 mol% PCBM as an electron acceptor, photoexcited at 430 nm at $\sim 1 \times 10^{13}$ absorbed flux, left. Yield-mobility products are shown on the right indicating subtle differences with fluence. Maximum yield-mobility products are shown to decrease with increasing tail length. Recall that the charge carrier mobility was the same across different tail lengths making the difference in yield-mobility product here actually a difference in yield. Thus the tail length is leading to a difference in the total quantity of charges generated.

The n,2-OBTTT molecules are also studied as electron donors in dilute blends with the prototypical electron acceptor, PC₆₀BM, Figure 6-18. Low weight-percent loading of the electron acceptor, in this case 2 mol%, is used to minimize the PCBM mobility contribution to the signal, thus eliminating PCBM mobility from the yield-mobility product. Samples containing molar ratios of PCBM in 6,2-OBTTT ranging from 0.1% to 50% of PCBM were measured and showed that the PCBM mobility contribution turned on with a molar loading of between 10% and 50%,

thus samples at 2 mol% loading have no clustered PCBM contribution. Considering the aforementioned neat n,2-OBTTT microwave mobility study (in which it is proposed that the mobility is constant across the series) this then becomes a comparison of charge generation yield. The first noticeable feature is that the photoconductance transient peak, $t = 0$, is largest for the shortest-tailed molecules and the peak decreases for increasing tail lengths. Thus the tail has an appreciable effect on the charge generation yield. Note that these are all approximately an order or magnitude larger in yield-mobility product than the neat n,2-OBTTT materials ($\phi \approx 10\%$.)

There are several possible explanations for the observed tail-length dependent yield values. Intermolecular mixing of the donor and acceptor could lead to different morphologies within the samples. These molecular tail lengths were again chosen to encompass a spread of tail lengths, and odd and even tails to gauge effects of tail length and parity. Films in this study are not annealed to minimize any clustering of PCBM, but this also leads to a wider variety of crystallizations. Yet diffraction experiments show no correlation between tail length and crystallite size (by comparison of peak fwhm.)

Another possible explanations leading to the difference in photoconductance by the tail length relates to the observation of the J-like energy transition. Driving force, ΔG , for charge transfer in donor-acceptor systems can be approximated as the difference in initial and final energy states, as shown in Equation 6-1.^{2,4}

$$\Delta G = IP_D - EA_A - E_{ex}$$

Equation 6-1

Differences in driving force could be due to either or both 1) varied ionization potential of n,2-OBTTT for different tail length or 2) variation in the exciton energy. To consider the first possibility, samples containing low weight percent loading of n,2-OBTTT are added to PCBM. Thus any difference in total yield of the n,2-OBTTT series is minimized.

6.5.3 Driving Force Between PCBM and Isolated n,2-OBTTT

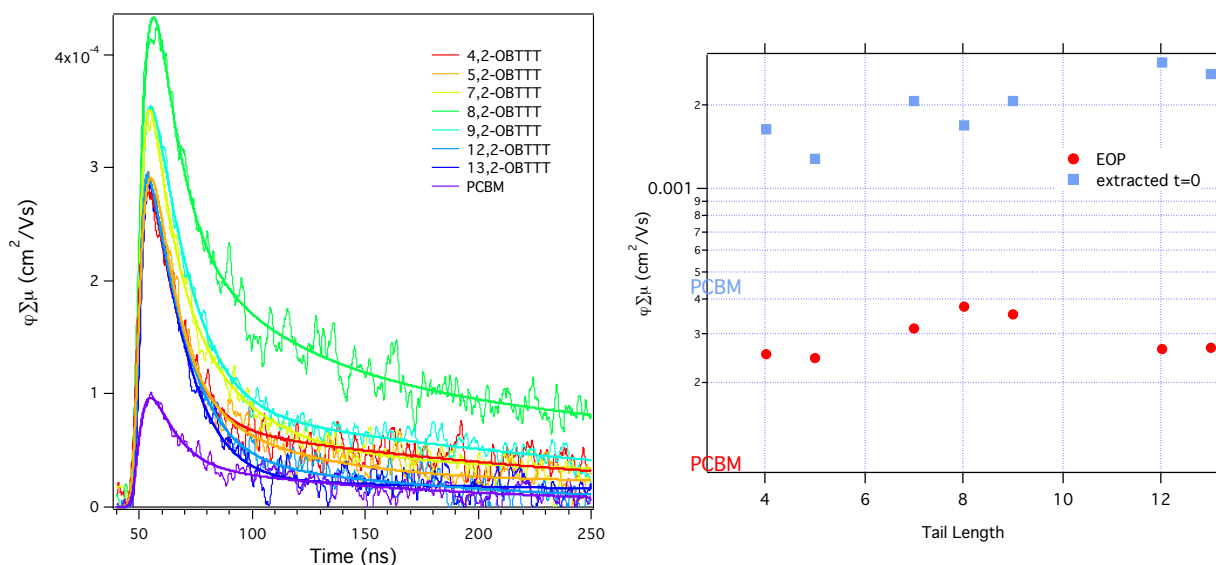


Figure 6-19. Photoconductance transients of 99 mol% PCBM doped with various n,2-OBTTT molecules (left) excited at 430 nm, the end-of-pulse (EOP) and extracted $t=0$ values for the same films are shown in the right plot, all fluences are $\sim 1 \times 10^{13}$ photons*cm⁻². No systematic difference is seen in the EOP data, and a very slight trend with increasing yield as tail length is increased is seen in the fit and extracted $t=0$ data. This trend is actually opposite that seen in the 2% PCBM and n,2-OBTTT blends and thus does not account for the yield/tail length difference in figure 6-18.

Figure 6-19 shows the photoconductance transients for samples containing 1 mol% n,2-OBTTT in PCBM. Some variation is observed in the samples, which may be due to minute amounts of n,2-OBTTT crystallization in certain samples. The transients show that all samples, excluding 8,2-OBTTT in PCBM, have similar short-lived charge dynamics. Tri-exponential decays are fit to the transients and are also shown on the plot. The slight variation in decay

dynamics leads to differences between the end-of-pulse yield-mobility product taken from the transients and the extracted $t = 0$ value from the exponential fits, Figure 6-19 right. As mentioned, the mobility is dominated in these samples by PCBM, and so the difference in the yield-mobility product is due to a difference in yield. The $t = 0$ shows a very subtle increase in yield with increasing tail length in this dilute regime, which is opposite the trend observed from the n,2-OBTTT dilute blend samples. The minimal difference in the signal demonstrates that the driving force for the PCBM/n,2-OBTTT series is nearly tail length independent. Using the previously measured PCBM microwave mobility, similar to in chapter 4, the charge generation yield is determined to be $\sim 5\%$. Driving force of the isolated molecule is not leading to the difference in signal for Figure 6-17, thus it is likely that there is a tail length modulated photoinduced charge transfer between n,2-OBTTT and PCBM.

As mentioned, another possible variation in driving force could be due to a difference in exciton energy, E_{ex} . Recall from the thin film photophysics section that the absorption edge increased systematically with increasing tail length. Although all sample studied here were excited with 430 nm light, the rapid relaxation of the hot exciton to the lowest energy level would lead to a difference in the exciton energy of each n,2-OBTTT film. If the exciton energy is the only source of difference for the ΔG equation, then a decrease in exciton energy would lead to less driving force and therefore less charge generation. A test to this hypothesis is the comparison of the yield-mobility product and the measured exciton energy, as shown in Figure 6-20. The exciton energy is in fact linearly correlated with the yield-mobility product. Ultimately the degree of J-like aggregation is determining the yield of generated charges.

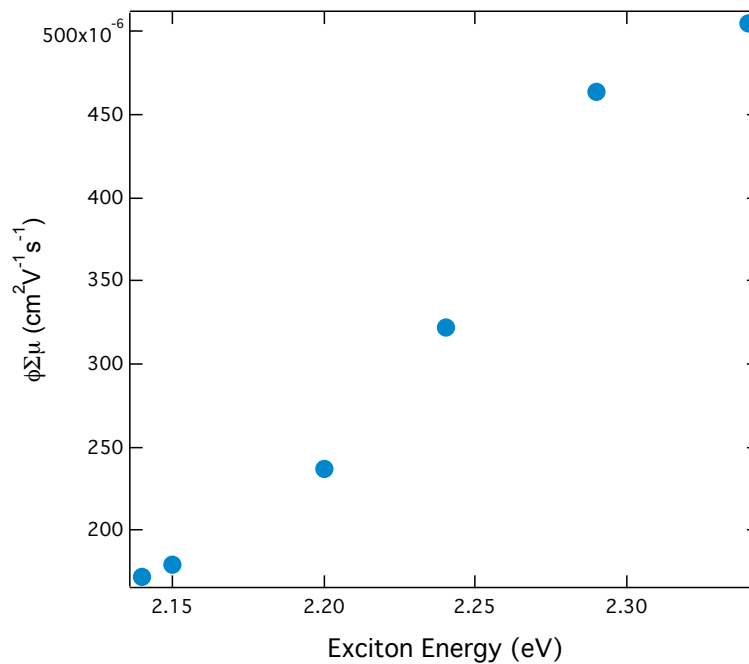


Figure 6-20. Maximum yield-mobility product for samples of 2 mol% PCBM in different n,2-OBTTT sample (n = 2, 3, 6, 8, 11, 12) plotted against the measured exciton energy for each n,2-OBTTT film. The microwave mobility is unchanged for different tail lengths, making the yield-mobility product effectively a comparison of yields. The exciton energy is shown to substantially affect the driving force of the charge transfer process, and is particularly dependent on the extent of J-like aggregation in the sample.

6.5.4 Photoconductivity of PCBM/n,2-OBTTT Films

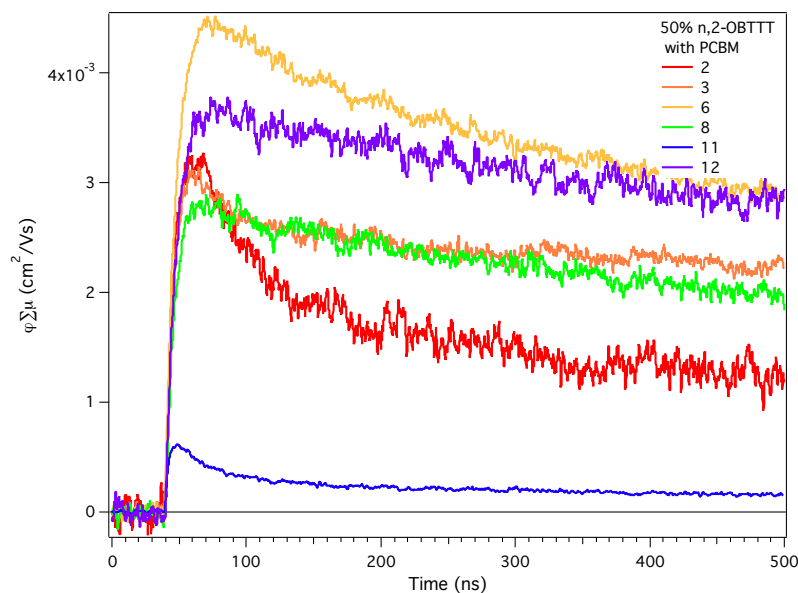


Figure 6-21. Photoconductance transients of 50/50 mol% mixtures of n,2-OBTTT/PCBM heterojunction excited at 430 nm (fluence 1×10^{12} photons/cm²). The driving force dependent yield-mobility product observed in the low molar PCBM loading studies is not duplicated for these 50/50 heterojunctions. All samples studied here ($n = 2, 3, 6, 8, 11$ and 12) except $n = 11$ show high yield-mobility products.

Studies of the n,2-OBTTT mesogens were expanded to include electron acceptor loading similar to that of device heterojunctions, 50 mol% PCBM. Akin to the 2 mol% study above, a variety of lengths and odd-even tails are included, specifically $n = 2, 3, 6, 8, 11, 12$. Samples were spincoated and measured as-spun to make the PCBM clustering would be similar across the series. As measured in the neat samples, the carrier mobility remains nearly constant across the series. Though a distinct tail-dependence (due to differing exciton energy) was measured for the photoconductivity in low loadings of PCBM, the 50/50 loaded films show no similar trend, Figure 6-21. The 11,2-OBTTT showed markedly lower charge yield than the others measured, but this study displays that the tail-length driving force modulation may not be relevant for high mol% heterojunction mixing. The fluence-dependent yield-mobility plot is shown in Figure 6-22,

further showing that at various light intensities the 11,2-OBTTT/PCBM sample yield differs from the rest of the series.

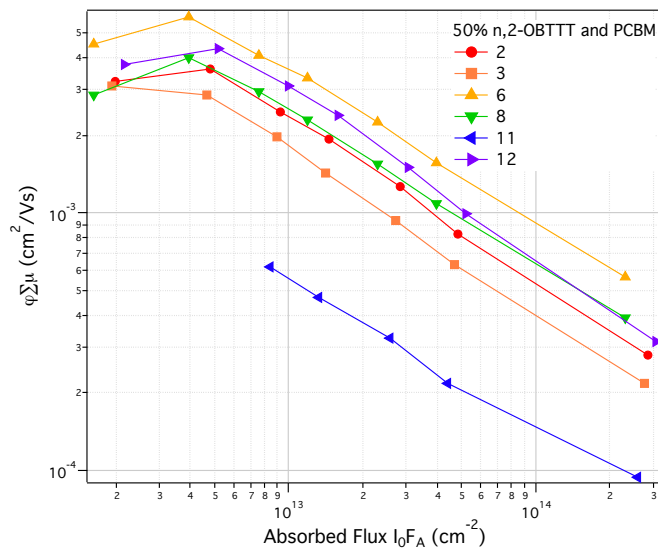


Figure 6-22. Yield-mobility product plots of the same n,2-OBTTT/PCBM heterojunctions photoexcited at various intensities of 430 nm light.

Triexponential fit yield-mobility data for 6,2-OBTTT gives a $t=0$ yield-mobility product of $0.0179 \text{ cm}^2\text{V}^{-1}\text{s}^{-1}$, which, if the PCBM is assumed to dominate the mobility gives a yield of 45% (this assumption is reasonable considering the PCBM mobility is at least an order of magnitude larger than that of the n,2-OBTTT series.)

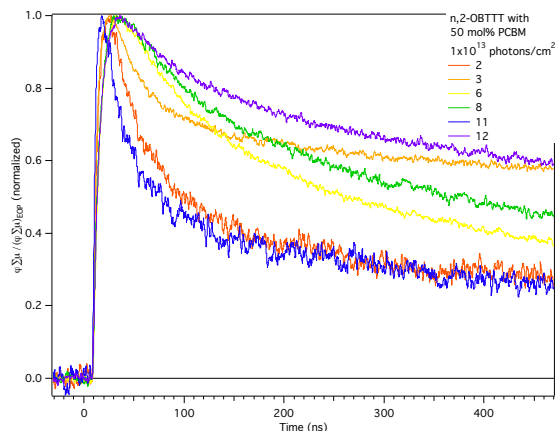


Figure 6-23. Normalized transients of the PCBM/ n,2-OBTTT films used to show the relative lifetimes of charges in blends of the different homologues. Notably,

Figure 6-23 shows that the recombination (or otherwise decay) dynamics are not universal across the tail series, nor are correlated with tail length. The decay is fastest for the 11,2-OBTTT and 2,2-OBTTT heterojunctions, though the 2,2-OBTTT sample has a larger overall yield it decays with nearly the same rate. Surprisingly the slowest decay, and consequently longest-lived charges, was measured in the longest tail-length sample, 12,2-OBTTT.

While driving force was shown to have a large effect on charge transfer in the 2 mol% PCBM in n,2-OBTTT samples the same is not shown for the high PCBM loaded samples. Thus while driving force is a reasonable predictor of photo-induced charge transfer in dilute blends a more complicated energy profile is created in the heterojunction (high levels of mixing) which leads to a less straightforward description of charge transfer.

6.5.5 n,2-OBTTT as an Electron Acceptor

The electrochemically determined ionization potentials of n,2-OBTTT in solution, chapter 5, show the possibility for a favorable electron transfer from P3HT to n,2-OBTTT. Just

as the tail lengths were compared for their electron donating ability in the preceding section here two tail lengths are compared for their electron accepting ability, 2,2-OBTTT and 11,2-OBTTT.

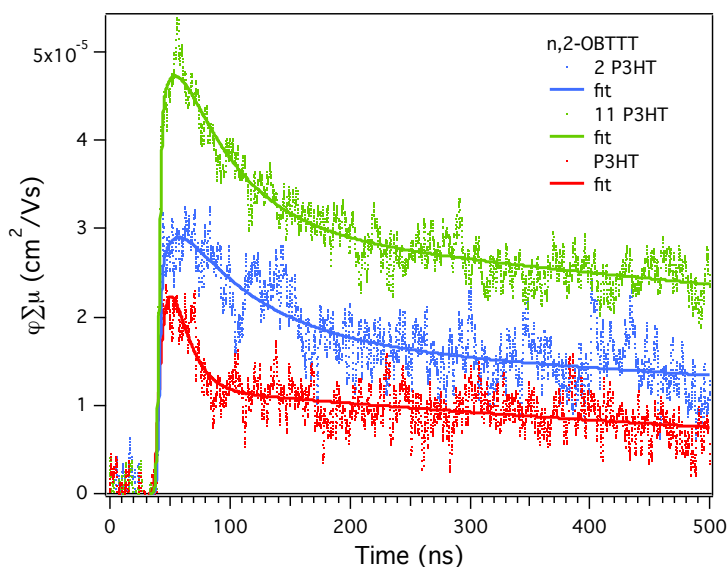


Figure 6-24. Transients of 2,2-OBTTT and 11,2-OBTTT mixed with P3HT (50 wt%) and neat P3HT to compare generation yields in thin films photoexcited at 430 nm. Both tail lengths act as electron acceptor and undergo photoinduced charge transfer with P3HT.

Figure 6-25 shows the modest yield-mobility enhancement of the n,2-OBTTT electron acceptors. (Note: an optically dense film of 3,2-OBTTT with P3HT showed near unity charge generation, Figure 6-26.) Both P3HT and n,2-OBTTT were photoexcited with 430 nm light. These results point to the n,2-OBTTT series acting as an electron acceptor with P3HT. Further, the charge generation with the polymer appears independent of tail length, possibly indicating a sufficient driving force for either tail length or an energy transfer process to P3HT.

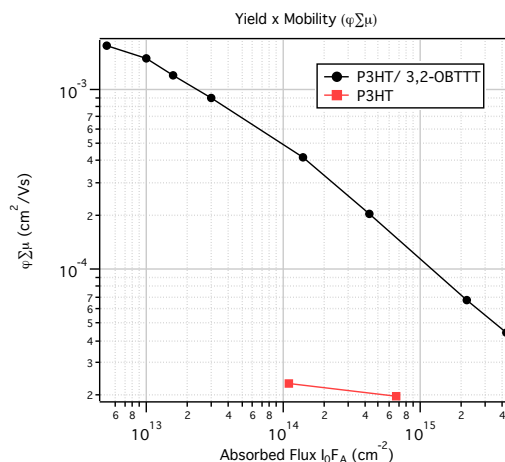


Figure 6-25. TRMC yield-mobility product diagram of optically dense film of a P3HT/3,2-OBTTT heterojunction photoexcited at 420 nm. This was shown to be a very high yield-mobility sample, it is likely that both components contribute to the mobility product and thus a yield cannot be extracted.

6.6 Studies of n,2-OBTTT as a High-Energy Sensitizer in P3HT/PCBM Blends

One very interesting but not fully explainable result from this work is that from the use of n,2-OBTTT as a dopant in a PCBM/P3HT blend. Recent studies using molecular dyes as sensitizers in heterojunction blends have shown a promising increase in device efficiency.^{39, 88-90} Typically dopants have been used to increase device absorption of the solar spectrum, and are thus generally low bandgap materials⁸⁹ (P3HT/PCBM lacks significant absorption at near infrared wavelengths.)

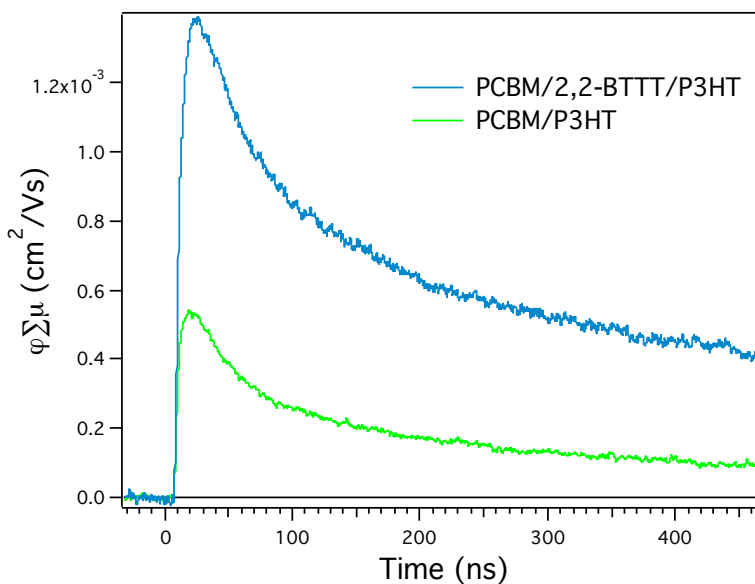


Figure 6-26. Yield-mobility product to compare two heterojunctions of P3HT/PCBM, one containing 2,2-OBTTT and the other without. The 2,2-OBTTT is acting as a high-energy sensitizer in the prototypical heterojunction blend. The carrier dynamics of the sample appear unchanged with the additive but the total yield is over 2x higher with the small molecule.

The 2,2-OBTTT is shown to undergo charge transfer with both PCBM and P3HT, here 10 wt% 2,2-OBTTT is added to a mixture of the two prototypical OPV components. Figure 6-27 shows that the added 2,2-OBTTT improved the signal (larger) relative to an otherwise identically prepared film of just the typical donor and acceptor. The carrier dynamics of the sample appear unchanged with the additive but the total yield is over 2x higher with the small molecule. The PCBM carrier mobility is likely dominant in the blend (and much larger than that of the 2,2-OBTTT molecule) thus it is speculated that the increased yield-mobility product signal is due to increased yield in the system and not increased mobility. The dopant led to a higher yield of photoinduced charges in the film.

The origin of the yield increase is unknown but may be due to either microstructural or energetic differences in the sample. The samples measured in Figure 6-27 were excited at 430

nm, a wavelength absorbed by all three heterojunction components. Additionally, all three components are able to undergo photoinduced charge transfer with each other component. It is possible that a process of energy funneling is occurring to a more efficient charge transfer location (either in energetics or microstructure.) Future studies will further determine the origin of the increased charge generation in samples with 2,2-OBTTT (and other n,2-OBTTT) dopants.

6.7 Conclusion

Several interesting properties were determined to vary as a function of molecular tail length in the n,2-OBTTT thiophenic small molecule series. Powder XRD showed that in thin films the crystal layer spacing is just larger than that of the molecular length, and thus the layers are composed of untilted sheets of molecules. Thin film absorption showed H- and J-like spectral features, which were correlated to a proposed intralayer structuring of the molecules. Remarkably, the J-like absorption was shown to decrease in energy with increasing tail length.

Charge generation yields were studied with TRMC. In dilute blends of PCBM in n,2-OBTTT it was determined that the exciton energy is linearly correlated with the charge yield (due to the ΔG driving force) leading to more charge transfer in shorter-tailed n,2-OBTTT molecules, but this trend does not hold for the device-loadings of PCBM. P3HT and n,2-OBTTT were also shown to undergo photoinduced charge transfer. Finally, preliminary results on a study using n,2-OBTTT as a high-energy sensitizer for P3HT/PCBM blends showed a 2-fold increase in yield as compared to an unsensitized heterojunction.

Chapter VII: The Role of Microstructural Effects in Photoinduced Charge Transfer Processes

When I set-out to quantify the effects of microstructure on charge generation in organic photovoltaics I anticipated that the effects of microstructure (assuming the electron transfer energetics were favorable) would largely fall into groups of “good” and “poor” contact between the donor and acceptor species of the active layer and that this would correspondingly lead to “good” and “poor” charge transfer. Two different systems studied in this work were shown to “work” and “not work” to varying degrees dependent on microstructure but the determining factor of their success was, ultimately, based on the electronic interactions within the donor material, and between the donor and acceptor, which itself can be dependent on the microstructure. Through the work here a much more intricate relationship is highlighted between the active layer microstructure and the photoinduced charge transfer process.

In the work on helical nanofilaments, chapter 3, two thin-film microstructures of the P-9-OPIMB liquid crystal were created and identified. In films of neat P-9-OPIMB, HNFs were shown to form in spincoated films while annealing the film would lead to curved smectic layers with homeotropic alignment. Thus a difference was observed in the kinetically (as-spun) and thermodynamically (annealed) formed structures. Fullerenes were also added to P-9-OPIMB and the resulting microstructures showed very similarly-formed films with differences between kinetic and thermodynamic films structures.

In blended heterojunctions of P-9-OPIMB and PCBM, photoinduced charge transfer was modestly efficient when P-9-OPIMB was structured into helical nanofilaments but when films

were annealed into a lamellar heterojunction the charge transfer process effectively shut off. Absorption of the lamellar phase, in which PCBM was also shown to form clusters, showed an additional absorption feature with its own radiant emission, proposed to be an optically active charge-transfer state, CT. This led to the conjecture that the formation of the CT state is acting as a competitive process with the charge separated state of a photoinduced charge transfer. Thus the microstructure has changed the energetics of interaction between the donor and acceptor, which is also shown to greatly affect the charge generation yield, and thus microstructure changes the rates of competitive processes.

Films of n,2-OBTTT molecules also showed certain microstructural differences, although in this case the focus of the study was to quantify the differences in the microstructure based on an increase in alkoxy tail length. The n,2-OBTTT structural variations due to tail length n led to changes in the growth of a J-aggregation with increased tail length. Consequently that led to a systematic decrease in the exciton energy for increased tail lengths and thus a decrease in the accompanying energetic driving force for the charge transfer in the system. Thus a direct relationship between tail length and charge generation yield were measured, and changes in microstructure affected the charge transfer driving force.

Bulk morphology of the small molecule systems have been measured for both molecular systems, quite thoroughly with extensive use of PLM, XRD, optical characterization, etc. for the case of the helical nanofilaments and with x-ray crystallography for the n,2-OBTTT system. For both systems here they were made into thin films and characterized with powder XRD. Notably both systems varied substantially between the bulk structure and that of the thin film. Furthermore, neither the thermodynamic nor kinetic microstructures were systematically

References

1. Brabec, C.; Sariciftci, N.; Hummelen, J., Plastic solar cells. *Advanced Functional Materials* 2001, 11, 15-26.
2. Clarke, T.; Durrant, J., Charge Photogeneration in Organic Solar Cells. *Chemical Reviews* 2010, 110, 6736-6767.
3. Bredas, J.; Norton, J.; Cornil, J.; Coropceanu, V., Molecular Understanding of Organic Solar Cells: The Challenges. *Accounts of Chemical Research* 2009, 42, 1691-1699.
4. Coffey, D.; Larson, B.; Hains, A.; Whitaker, J.; Kopidakis, N.; Boltalina, O.; Strauss, S.; Rumbles, G., An Optimal Driving Force for Converting Excitons into Free Carriers in Excitonic Solar Cells. *Journal of Physical Chemistry C* 2012, 116, 8916-8923.
5. Sun, Y.; Welch, G.; Leong, W.; Takacs, C.; Bazan, G.; Heeger, A., Solution-processed small-molecule solar cells with 6.7% efficiency. *Nature Materials* 2012, 11, 44-48.
6. Yang, J.; Nguyen, T., Effects of thin film processing on pentacene/C-60 bilayer solar cell performance. *Organic Electronics* 2007, 8, 566-574.
7. TANG, C., 2-LAYER ORGANIC PHOTOVOLTAIC CELL. *Applied Physics Letters* 1986, 48, 183-185.
8. Gregg, B.; Lieberman, M., Excitonic solar cells: The physics and chemistry of organic-based photovoltaics. *Molecules As Components of Electronic Devices* 2003, 844, 243-257.
9. Hains, A.; Liang, Z.; Woodhouse, M.; Gregg, B., Molecular Semiconductors in Organic Photovoltaic Cells. *Chemical Reviews* 2010, 110, 6689-6735.
10. Ohkita, H.; Cook, S.; Astuti, Y.; Duffy, W.; Tierney, S.; Zhang, W.; Heeney, M.; McCulloch, I.; Nelson, J.; Bradley, D.; Durrant, J., Charge carrier formation in polythiophene/fullerene blend films studied by transient absorption spectroscopy. *Journal of the American Chemical Society* 2008, 130, 3030-3042.
11. Coffey, D.; Ferguson, A.; Kopidakis, N.; Rumbles, G., Photovoltaic Charge Generation in Organic Semiconductors Based on Long-Range Energy Transfer. *Acs Nano* 2010, 4, 5437-5445.

12. Sirringhaus, H.; Sakanoue, T.; Chang, J., Charge-transport physics of high-mobility molecular semiconductors. *Physica Status Solidi B-Basic Solid State Physics* 2012, 249, 1655-1676.
13. Kroeze, J.; Savenije, T.; Warman, J., Electrodeless determination of the trap density, decay kinetics, and charge separation efficiency of dye-sensitized nanocrystalline TiO₂. *Journal of the American Chemical Society* 2004, 126, 7608-7618.
14. Pisula, W.; Zorn, M.; Chang, J.; Mullen, K.; Zentel, R., Liquid Crystalline Ordering and Charge Transport in Semiconducting Materials. *Macromolecular Rapid Communications* 2009, 30, 1179-1202.
15. Gregg, B., Excitonic solar cells. *Journal of Physical Chemistry B* 2003, 107, 4688-4698.
16. KNOX, R., SPECTRAL EFFECTS OF EXCITON SPLITTING IN STATISTICAL PAIRS. *Journal of Physical Chemistry* 1994, 98, 7270-7273.
17. Wurthner, F.; Kaiser, T.; Saha-Moller, C., J-Aggregates: From Serendipitous Discovery to Supramolecular Engineering of Functional Dye Materials. *Angewandte Chemie-International Edition* 2011, 50, 3376-3410.
18. Kasha, M.; Rawls, H. R.; Ashraf El-Bayoumi, M., The Exciton Model in Molecular Spectroscopy. *Pure and Applied Chemistry* 1965, 11, 371-392.
19. Basko, D.; Lobanov, A.; Pimenov, A.; Vitukhnovsky, A., Molecular arrangement of the Davydov-split dye aggregates. *Chemical Physics Letters* 2003, 369, 192-197.
20. YASSAR, A.; HOROWITZ, G.; VALAT, P.; WINTGENS, V.; HMYENE, M.; DELOFFRE, F.; SRIVASTAVA, P.; LANG, P.; GARNIER, F., EXCITON COUPLING EFFECTS IN THE ABSORPTION AND PHOTOLUMINESCENCE OF SEXITHIOPHENE DERIVATIVES. *Journal of Physical Chemistry* 1995, 99, 9155-9159.
21. Camposeo, A.; Polo, M.; Tavazzi, S.; Silvestri, L.; Spearman, P.; Cingolani, R.; Pisignano, D., Polarized superradiance from delocalized exciton transitions in tetracene single crystals. *Physical Review B* 2010, 81.
22. Najafov, H.; Lee, B.; Zhou, Q.; Feldman, L.; Podzorov, V., Observation of long-range exciton diffusion in highly ordered organic semiconductors. *Nature Materials* 2010, 9, 938-943.

23. Lunt, R.; Benziger, J.; Forrest, S., Relationship between Crystalline Order and Exciton Diffusion Length in Molecular Organic Semiconductors. *Advanced Materials* 2010, 22, 1233-+.
24. Pelzl, G.; Diele, S.; Weissflog, W., Banana-shaped compounds - A new field of liquid crystals. *Advanced Materials* 1999, 11, 707-724.
25. Hough, L.; Jung, H.; Kruerke, D.; Heberling, M.; Nakata, M.; Jones, C.; Chen, D.; Link, D.; Zasadzinski, J.; Heppke, G.; Rabe, J.; Stocker, W.; Korblova, E.; Walba, D.; Glaser, M.; Clark, N., Helical Nanofilament Phases. *Science* 2009, 325, 456-460.
26. Kim, H.; Lee, S.; Shin, T.; Cha, Y.; Korblova, E.; Walba, D.; Clark, N.; Lee, S.; Yoon, D., Alignment of helical nanofilaments on the surfaces of various self-assembled monolayers. *Soft Matter* 2013, 9, 6185-6191.
27. Callahan, R.; Coffey, D.; Chen, D.; Clark, N.; Rumbles, G.; Walba, D., Charge Generation Measured for Fullerene – Helical Nanofilament Liquid Crystal Heterojunctions. *ACS Applied Materials & Interfaces* 2014.
28. Chen, D.; MacLennan, J.; Shao, R.; Yoon, D.; Wang, H.; Korblova, E.; Walba, D.; Glaser, M.; Clark, N., Chirality-Preserving Growth of Helical Filaments in the B4 Phase of Bent-Core Liquid Crystals. *Journal of the American Chemical Society* 2011, 133, 12656-12663.
29. Tsai, E.; Richardson, J.; Korblova, E.; Nakata, M.; Chen, D.; Shen, Y.; Shao, R.; Clark, N.; Walba, D., A Modulated Helical Nanofilament Phase. *Angewandte Chemie-International Edition* 2013, 52, 5254-5257.
30. Walba, D.; Eshdat, L.; Korblova, E.; Shoemaker, R., On the nature of the B4 banana phase: crystal or not a crystal? *Crystal Growth & Design* 2005, 5, 2091-2099.
31. Ohno, A.; Haruyama, A.; Kurotaki, K.; Hanna, J., Charge-carrier transport in smectic mesophases of biphenyls. *Journal of Applied Physics* 2007, 102.
32. Iino, H.; Ohno, A.; Hanna, J., Hole mobility and lifetime in a smectic liquid crystalline photoconductor of a 2-phenyl naphthalene derivative. *Journal of Chemical Physics* 2005, 123.
33. Eccher, J.; Faria, G.; Bock, H.; von Seggern, H.; Bechtold, I., Order Induced Charge Carrier Mobility Enhancement in Columnar Liquid Crystal Diodes. *Acs Applied Materials & Interfaces* 2013, 5, 11935-11943.

34. An, Z.; Yu, J.; Jones, S.; Barlow, S.; Yoo, S.; Domercq, B.; Prins, P.; Siebbeles, L.; Kippelen, B.; Marder, S., High electron mobility in room-temperature discotic liquid-crystalline perylene diimides. *Advanced Materials* 2005, 17, 2580-+.
35. An, Z.; Yu, J.; Domercq, B.; Jones, S.; Barlow, S.; Kippelen, B.; Marder, S., Room-temperature discotic liquid-crystalline coronene diimides exhibiting high charge-carrier mobility in air. *Journal of Materials Chemistry* 2009, 19, 6688-6698.
36. Benito-Hernandez, A.; Pandey, U.; Cavero, E.; Termine, R.; Garcia-Frutos, E.; Serrano, J.; Golemme, A.; Gomez-Lor, B., High Hole Mobility in Triindole-Based Columnar phases: Removing the Bottleneck of Homogeneous Macroscopic Orientation. *Chemistry of Materials* 2013, 25, 117-121.
37. Dayal, S.; Kopidakis, N.; Rumbles, G., Photoinduced electron transfer in composites of conjugated polymers and dendrimers with branched colloidal nanoparticles. *Faraday Discussions* 2012, 155, 323-337.
38. Ferguson, A.; Kopidakis, N.; Shaheen, S.; Rumbles, G., Quenching of excitons by holes in poly(3-hexylthiophene) films. *Journal of Physical Chemistry C* 2008, 112, 9865-9871.
39. Kroeze, J.; Savenije, T., The application of a low-bandgap conjugated oligomer for the sensitization of SnO₂ and TiO₂. *Thin Solid Films* 2004, 451, 54-59.
40. Abdi, F.; Savenije, T.; May, M.; Dam, B.; van de Krol, R., The Origin of Slow Carrier Transport in BiVO₄ Thin Film Photoanodes: A Time-Resolved Microwave Conductivity Study. *Journal of Physical Chemistry Letters* 2013, 4, 2752-2757.
41. Mozer, A.; Sariciftci, N.; Pivrikas, A.; Osterbacka, R.; Juska, G.; Brassat, L.; Bassler, H., Charge carrier mobility in regioregular poly(3-hexylthiophene) probed by transient conductivity techniques: A comparative study. *Physical Review B* 2005, 71.
42. Grozema, F.; Siebbeles, L., Charge Mobilities in Conjugated Polymers Measured by Pulse Radiolysis Time-Resolved Microwave Conductivity: From Single Chains to Solids. *Journal of Physical Chemistry Letters* 2011, 2, 2951-2958.
43. Dicker, G. Photogeneration and dynamics of charge carriers in the conjugated polymer poly(3-hexylthiophene). Technische Universiteit Delft: Delft, The Netherlands, 2004.

44. Reid, O.; Rumbles, G., Quantitative Transient Absorption Measurements of Polaron Yield and Absorption Coefficient in Neat Conjugated Polymers. *Journal of Physical Chemistry Letters* 2013, 4, 2348-2355.
45. de Haas, M.; Warman, J.; Anthopoulos, T.; de Leeuw, D., The mobility and decay kinetics of charge carriers in pulse-ionized microcrystalline PCBM powder. *Advanced Functional Materials* 2006, 16, 2274-2280.
46. Langhals, H.; Karolin, J.; Johansson, L., Spectroscopic properties of new and convenient standards for measuring fluorescence quantum yields. *Journal of the Chemical Society-Faraday Transactions* 1998, 94, 2919-2922.
47. AKUTAGAWA, T.; MATSUNAGA, Y.; YASUHARA, K., MESOMORPHIC BEHAVIOR OF 1,3-PHENYLENE BIS[4-(4-ALKOXYPHENYLIMINOMETHYL)BENZOATES] AND RELATED-COMPOUNDS. *Liquid Crystals* 1994, 17, 659-666.
48. Chen, D.; Zhu, C.; Wang, H.; MacLennan, J.; Glaser, M.; Korblova, E.; Walba, D.; Rego, J.; Soto-Bustamante, E.; Clark, N., Nanoconfinement of guest materials by helical nanofilament networks of bent-core mesogens. *Soft Matter* 2013, 9, 462-471.
49. Zhu, C.; Chen, D.; Shen, Y.; Jones, C.; Glaser, M.; MacLennan, J.; Clark, N., Nanophase segregation in binary mixtures of a bent-core and a rodlike liquid-crystal molecule. *Physical Review E* 2010, 81.
50. Yoon, D.; Yi, Y.; Shen, Y.; Korblova, E.; Walba, D.; Smalyukh, I.; Clark, N., Orientation of a Helical Nanofilament (B4) Liquid-Crystal Phase: Topographic Control of Confinement, Shear Flow, and Temperature Gradients. *Advanced Materials* 2011, 23, 1962-1967.
51. Araoka, F.; Sugiyama, G.; Ishikawa, K.; Takezoe, H., Highly Ordered Helical Nanofilament Assembly Aligned by a Nematic Director Field. *Advanced Functional Materials* 2013, 23, 2701-2707.
52. Bialecka-Florjanczyk, E.; Sledzinska, I.; Gorecka, E.; Przedmojski, J., Odd-even effect in biphenyl-based symmetrical dimers with methylene spacer - evidence of the B4 phase. *Liquid Crystals* 2008, 35, 401-406.

53. Chen, D.; Heberling, M.; Nakata, M.; Hough, L.; MacLennan, J.; Glaser, M.; Korblova, E.; Walba, D.; Watanabe, J.; Clark, N., Structure of the B4 Liquid Crystal Phase near a Glass Surface. *Chemphyschem* 2012, 13, 155-159.
54. Mens, R.; Chambon, S.; Bertho, S.; Reggers, G.; Ruttens, B.; D'Haen, J.; Manca, J.; Carleer, R.; Vanderzande, D.; Adriaensens, P., Description of the nanostructured morphology of [6,6]-phenyl-C-61-butyric acid methyl ester (PCBM) by XRD, DSC and solid-state NMR. *Magnetic Resonance in Chemistry* 2011, 49, 242-247.
55. Patterson, A., The Scherrer formula for x-ray particle size determination. *Physical Review* 1939, 56, 978-982.
56. Yin, W.; Dadmun, M., A New Model for the Morphology of P3HT/PCBM Organic Photovoltaics from Small-Angle Neutron Scattering: Rivers and Streams. *Acs Nano* 2011, 5, 4756-4768.
57. Walba, D.; Korblova, E.; Shao, R.; MacLennan, J.; Link, D.; Glaser, M.; Clark, N., A ferroelectric liquid crystal conglomerate composed of racemic molecules. *Science* 2000, 288, 2181-2184.
58. Kim, J.; Frisbie, D., Correlation of Phase Behavior and Charge Transport in Conjugated Polymer/Fullerene Blends. *Journal of Physical Chemistry C* 2008, 112, 17726-17736.
59. Wu, J.; Usui, T.; Hanna, J., Synthesis of a novel smectic liquid crystalline glass and characterization of its charge carrier transport properties. *Journal of Materials Chemistry* 2011, 21, 8045-8051.
60. Feng, X.; Marcon, V.; Pisula, W.; Hansen, M.; Kirkpatrick, J.; Grozema, F.; Andrienko, D.; Kremer, K.; Mullen, K., Towards high charge-carrier mobilities by rational design of the shape and periphery of discotics. *Nature Materials* 2009, 8, 421-426.
61. Thelese, R.; Chan, K.; Hu, X., Structure and properties of nano-confined poly(3-hexylthiophene) in nano-array/polymer hybrid ordered-bulk heterojunction solar cells. *Nanoscale* 2012, 4, 478-485.
62. Hayashi, H.; Nihashi, W.; Umeyama, T.; Matano, Y.; Seki, S.; Shimizu, Y.; Imahori, H., Segregated Donor-Acceptor Columns in Liquid Crystals That Exhibit Highly Efficient Ambipolar Charge Transport. *Journal of the American Chemical Society* 2011, 133, 10736-10739.

63. Meiss, J.; Merten, A.; Hein, M.; Schuenemann, C.; Schafer, S.; Tietze, M.; Uhrich, C.; Pfeiffer, M.; Leo, K.; Riede, M., Fluorinated Zinc Phthalocyanine as Donor for Efficient Vacuum-Deposited Organic Solar Cells. *Advanced Functional Materials* 2012, 22, 405-414.
64. Campoy-Quiles, M.; Ferenczi, T.; Agostinelli, T.; Etchegoin, P.; Kim, Y.; Anthopoulos, T.; Stavrinou, P.; Bradley, D.; Nelson, J., Morphology evolution via self-organization and lateral and vertical diffusion in polymer: fullerene solar cell blends. *Nature Materials* 2008, 7, 158-164.
65. Agostinelli, T.; Lilliu, S.; Labram, J.; Campoy-Quiles, M.; Hampton, M.; Pires, E.; Rawle, J.; Bikondoa, O.; Bradley, D.; Anthopoulos, T.; Nelson, J.; Macdonald, J., Real-Time Investigation of Crystallization and Phase-Segregation Dynamics in P3HT:PCBM Solar Cells During Thermal Annealing. *Advanced Functional Materials* 2011, 21, 1701-1708.
66. Kim, J.; Kim, K.; Ko, S.; Kim, W., Optimum design of ordered bulk heterojunction organic photovoltaics. *Solar Energy Materials and Solar Cells* 2011, 95, 3021-3024.
67. Araoka, F.; Otani, T.; Ishikawa, K.; Takezoe, H., Spectral blue shift via intermolecular interactions in the B2 and B4 phases of a bent-shaped molecule. *Physical Review E* 2010, 82.
68. Cook, S.; Ohkita, H.; Kim, Y.; Benson-Smith, J.; Bradley, D.; Durrant, J., A photophysical study of PCBM thin films. *Chemical Physics Letters* 2007, 445, 276-280.
69. Hoofman, R.; vanderLaan, G.; deHaas, M.; Tanigaki, K., Charge migration in pulse-irradiated undoped C60 powder studied with the time-resolved microwave conductivity technique. *Synthetic Metals* 1997, 86, 2355-2356.
70. Dicker, G.; de Haas, M.; Siebbeles, L.; Warman, J., Electrodeless time-resolved microwave conductivity study of charge-carrier photogeneration in regioregular poly(3-hexylthiophene) thin films. *Physical Review B* 2004, 70.
71. I, M.; Heeney, M.; Bailey, C.; Genevicius, K.; I, M.; Shkunov, M.; Sparrowe, D.; Tierney, S.; Wagner, R.; Zhang, W.; Chabinyk, M.; Kline, R.; McGehee, M.; Toney, M., Liquid-crystalline semiconducting polymers with high charge-carrier mobility. *Nature Materials* 2006, 5, 328-333.
72. Parmer, J.; Mayer, A.; Hardin, B.; Scully, S.; McGehee, M.; Heeney, M.; McCulloch, I., Organic bulk heterojunction solar cells using poly(2,5-bis(3-tetradecylthiophen-2-yl)thieno[3,2-b]thiophene). *Applied Physics Letters* 2008, 92.

73. Mayer, A.; Toney, M.; Scully, S.; Rivnay, J.; Brabec, C.; Scharber, M.; Koppe, M.; Heeney, M.; McCulloch, I.; McGehee, M., Bimolecular Crystals of Fullerenes in Conjugated Polymers and the Implications of Molecular Mixing for Solar Cells. *Advanced Functional Materials* 2009, 19, 1173-1179.
74. Miller, N.; Sweetnam, S.; Hoke, E.; Gysel, R.; Miller, C.; Bartelt, J.; Xie, X.; Toney, M.; McGehee, M., Molecular Packing and Solar Cell Performance in Blends of Polymers with a Bisadduct Fullerene. *Nano Letters* 2012, 12, 1566-1570.
75. Martin, R.; Diederich, F., Linear monodisperse pi-conjugated oligomers: Model compounds for polymers and more. *Angewandte Chemie-International Edition* 1999, 38, 1350-1377.
76. de Melo, J.; Elisei, F.; Becker, R., Photophysical studies of mixed furan, pyrrole, and thiophene-containing oligomers with three and five rings. *Journal of Chemical Physics* 2002, 117, 4428-4435.
77. van Hutten, P.; Krasnikov, V.; Hadziioannou, G., A model oligomer approach to light emitting semiconducting polymers. *Accounts of Chemical Research* 1999, 32, 257-265.
78. Chen, P.; Yang, G.; Liu, T.; Li, T.; Wang, M.; Huang, W., Optimization of optoelectronic property and device efficiency of polyfluorenes by tuning structure and morphology. *Polymer International* 2006, 55, 473-490.
79. Ahmed, M.; Wang, C.; Keg, P.; Pisula, W.; Lam, Y.; Ong, B.; Ng, S.; Chen, Z.; Mhaisalkar, S., Thieno[3,2-b]thiophene oligomers and their applications as p-type organic semiconductors (vol 19, pg 3449, 2009). *Journal of Materials Chemistry* 2009, 19, 9288-9288.
80. Tanaka, H.; Kozuka, M.; Watanabe, S.; Ito, H.; Shimoi, Y.; Takimiya, K.; Kuroda, S., Observation of field-induced charge carriers in high-mobility organic transistors of a thienothiophene-based small molecule: Electron spin resonance measurements. *Physical Review B* 2011, 84.
81. He, J.; Su, Z.; Yan, B.; Xiang, L.; Wang, Y., The effects of different side groups on the properties of polythiophene. *Journal of Macromolecular Science Part a-Pure and Applied Chemistry* 2007, 44, 989-993.

82. Mitchell, W.; Kopidakis, N.; Rumbles, G.; Ginley, D.; Shaheen, S., The synthesis and properties of solution processable phenyl cored thiophene dendrimers. *Journal of Materials Chemistry* 2005, 15, 4518-4528.
83. STRICKLER, S.; BERG, R., RELATIONSHIP BETWEEN ABSORPTION INTENSITY AND FLUORESCENCE LIFETIME OF MOLECULES. *Journal of Chemical Physics* 1962, 37, 814-&.
84. Cardona, C.; Li, W.; Kaifer, A.; Stockdale, D.; Bazan, G., Electrochemical Considerations for Determining Absolute Frontier Orbital Energy Levels of Conjugated Polymers for Solar Cell Applications. *Advanced Materials* 2011, 23, 2367-2371.
85. GAGNE, R.; KOVAL, C.; LISENSKY, G., FERROCENE AS AN INTERNAL STANDARD FOR ELECTROCHEMICAL MEASUREMENTS. *Inorganic Chemistry* 1980, 19, 2854-2855.
86. Zhang, L.; Liu, M., Supramolecular Chirality and Chiral Inversion of Tetraphenylsulfonato Porphyrin Assemblies on Optically Active Polylysine. *Journal of Physical Chemistry B* 2009, 113, 14015-14020.
87. Hoffmann, S.; Bassler, H.; Kohler, A., What Determines Inhomogeneous Broadening of Electronic Transitions in Conjugated Polymers? *Journal of Physical Chemistry B* 2010, 114, 17037-17048.
88. Martinez-Diaz, M.; de la Torre, G.; Torres, T., Lighting porphyrins and phthalocyanines for molecular photovoltaics. *Chemical Communications* 2010, 46, 7090-7108.
89. Peet, J.; Tamayo, A.; Dang, X.; Seo, J.; Nguyena, T., Small molecule sensitizers for near-infrared absorption in polymer bulk heterojunction solar cells. *Applied Physics Letters* 2008, 93.
90. Silvestri, F.; Lopez-Duarte, I.; Seitz, W.; Beverina, L.; Martinez-Diaz, M.; Marks, T.; Guldi, D.; Pagani, G.; Torres, T., A squaraine-phthalocyanine ensemble: towards molecular panchromatic sensitizers in solar cells. *Chemical Communications* 2009, 4500-4502.